FACULTY OF MATHEMATICS AND PHYSICS
Charles University

MASTER THESIS

Vendula Benešová

Identified hadron production in deep-inelastic scattering at COMPASS

Department of Low-Temperature Physics

Supervisor of the master thesis: Mgr. Jan Matoušek, Ph.D.
Study programme: Particle and Nuclear Physics
Study branch: FCJFP

Prague 2025

I declare that I carried out this master thesis independently, and only with the cited sources, literature and other professional sources. It has not been used to obtain another or the same degree.

I understand that my work relates to the rights and obligations under the Act No. 121/2000 Sb., the Copyright Act, as amended, in particular the fact that the Charles University has the right to conclude a license agreement on the use of this work as a school work pursuant to Section 60 subsection 1 of the Copyright Act.

In .... date ....

Author's signature

A big thank you to Jan Matoušek, Anna Martin, Bakur Parsamyan, Andrea Bressan, the COMPASS collaboration, Davide Giordano, the ČEZ group, my mom, my dad, my family and my friends – in no particular order.

Title: Identified hadron production in deep-inelastic scattering at COMPASS

Author: Vendula Benešová

Department: Department of Low-Temperature Physics

Supervisor: Mgr. Jan Matoušek, Ph.D., Department of Low-Temperature Physics

Abstract: This thesis presents the measurement of azimuthal modulations and P_{T}^2 distributions of hadrons produced in semi-inclusive deep inelastic scattering of muons off an unpolarized liquid hydrogen target, using data from the 2016 COMPASS experiment. The analysis builds upon the author's bachelor's thesis, refining previous results and extending the study through the inclusion of hadron identification. Additionally, we compare the results obtained on a proton target with earlier COMPASS measurements on a deuteron target and other measurements on similar experiments. These comparisons aim to validate obtained results and provide further insight into the flavour dependence of structure functions and transverse momentum dependent distributions.

Keywords: DIS SIDIS COMPASS nucleon structure TMD PDF RICH hadron identification

Contents

Introduction

Sub-atomic structure has been studied ever since its discovery by Ernest Rutherford in 1911 [1]. The key to this experiment was the scattering of α particles to probe the internal structure of matter, a principle that has lasted to modern-day experiments probing the nucleon structure.

Results from deep inelastic scattering (DIS) of high-energy electrons off protons first hinted at the internal structure of the nucleon. To explain the observed behaviour, Richard Feynman proposed in the 1970s that hadrons, such as protons, are composed of point-like constituents called partons, leading to the development of the *parton model* [2]. Partons were later identified with quarks from Murray Gell-Man's quark model [3].

The existence of an intrinsic transverse momentum k_T for quarks inside hadrons was not an assumption in early parton models. The first hints of transverse motion in nucleons came from unexpectedly broad transverse momentum distributions of the produced particles, especially W and Z bosons. The difference between measurement and leading-order perturbative calculations indicated the presence of intrinsic transverse momentum of quarks, which causes observed particles to deviate from a purely collinear trajectory while broadening their transverse momentum distributions. These indications lead to dedicated studies of transverse momentum of partons in DIS and Drell-Yan processes.

In the first approximation, the distribution of the transverse and longitudinal momentum and the polarisation of partons inside the nucleon is described by eight transverse momentum dependent parton distribution functions[1], while fragmentation that follows right after the hard process is described by eight transverse momentum dependent fragmentation functions[2]. COMPASS measurements of SIDIS and Drell-Yan provide crucial data points for extracting key TMDs (TMD-PDFs and TMD-FFs), such as the Sivers, Transversity, and Boer-Mulders functions [4, 5, 6].

Although COMPASS is particularly well suited for studying spin-dependent TMDs thanks to its polarised targets and high-energy muon beams, the 2016 and 2017 physics program was dedicated to unpolarised measurements, primarily aimed at studying deeply virtual compton scattering (DVCS) and hard exclusive meson production (HEMP), which provide access to the combined spatial and momentum distributions of quarks and gluons inside hadrons [7, 8]. Nevertheless, the data collected are also suitable for unpolarised SIDIS studies. Another result from 2016 published by COMPASS is a SIDIS multiplicity measurement focused more on the collinear parton distribution functions and fragmentation functions [9].

Measurements of SIDIS provide crucial insights into TMDs, which help us with both the understanding of non-perturbative dynamics in low-energy quantum chromodynamics (QCD) and the prediction of high-energy hadron collisions. For instance, in proton-proton collisions, these effects significantly impact the precision of measurements such as the determination of the W boson mass from the $\mathrm{W} \to \ell\nu$ decay, where the mass is inferred from the missing transverse energy

[1] TMD-PDFs
[2] TMD-FFs

(neutrino) and the transverse momentum of the lepton. The uncertainty in TMDs contributes non-negligibly to the systematic uncertainties in such measurements, and its impact will become even more pronounced with the construction of increasingly powerful colliders [10]. Furthermore, the flavour dependence of TMDs is completely neglected in the current measurements, even though its presence can cause a difference up to 1 MeV [11].

In this thesis, unpolarised SIDIS data measured in 2016 at COMPASS experiment are being analysed. We provide results of azimuthal asymmetries and P_{T}^2-distributions for positive and negative hadrons. In addition, we compare results on proton and deuteron targets and try to distinguish kaons and pions among the measured hadrons to give more insight into the flavour dependence of TMDs. To accomplish accurate hadron identification for the measurement of unpolarised azimuthal asymmetries, we also extract the efficiency of the ring-imaging Cherenkov detector (RICH) detector in dependence on the azimuthal angle, which is another key task addressed in this thesis.

1. Theoretical path from SIDIS measurement to the TMDs

1.1 Kinematics and introduction of variables

In this thesis, we study the semi-inclusive measurement of the standard unpolarised DIS process (SIDIS) – scattering of a lepton off a nucleon with the detection of a final-state hadron as a collision product:

$$\ell(l) + \mathrm{N}(P) \to \ell'(l') + \mathrm{h}(P_\mathrm{h}) + \mathrm{X} \; . \tag{1.1}$$

In the equation 1.1 we denoted the rest of the hadronic final state by X and wrote 4-momenta of detected particles in affiliated parentheses. When the magnitude of the transferred momentum $q \equiv l - l'$ is far below the Z^0 mass, the interaction between lepton and nucleon is mediated exclusively via a virtual photon $\gamma^*(q)$ as shown in figure 1.1.

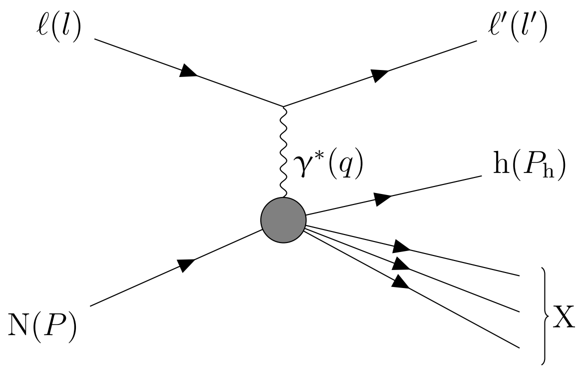

Figure 1.1: Feynman diagram of SIDIS process at tree level.

To describe the SIDIS process, this work will be using the following list of commonly used leptonic kinematical variables[1]:

virtuality Q^2, momentum transfer q :	$Q^2 \equiv -q^2 \equiv -(l-l')^2 \;, \quad (1.2)$
Bjorken scaling variable x :	$x \equiv \dfrac{Q^2}{2P \cdot q} \;, \quad (1.3)$
inelasticity y :	$y \equiv \dfrac{q \cdot P}{l \cdot P} \;, \quad (1.4)$
invariant mass of the hadronic final state W :	$W^2 \equiv (q+P)^2 \;. \quad (1.5)$

The same set of relativistic invariants is used for DIS description. In case of all particles unpolarised, any pair of quantities 1.2–1.5 is enough to provide all information about the state of the final lepton. DIS (and thus also SIDIS)

[1]Choice of the spacetime metric tensor is $g^{\mu\nu} = \mathrm{diag}\{1, -1, -1, -1\}$ in the whole work.

occurs only when the Bjorken limit is achieved – a condition defined as inequality between the aforementioned variables and the proton mass M_{N}:

$$Q^2 \gg M_{\mathrm{N}}^2 \qquad\qquad P \cdot q \gg M_{\mathrm{N}}^2 \tag{1.6}$$

A suitable reference frame needs to be introduced to complete the description of SIDIS. γ^*-nucleon system (GNS) depicted in 1.2 can be considered as a candidate when working with transverse components of momenta. Since it is a virtual photon – nucleon centre-of-mass frame with the z-axis direction aligned with the momentum of the virtual photon, the Lorentz boost from laboratory frame to GNS does not affect the transverse components of hadronic and quark momenta, making the analysis easier and GNS the perfect choice of reference frame.

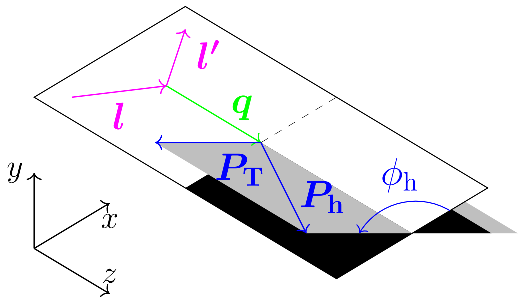

Figure 1.2: Scheme of GNS, definition of P_{T} and ϕ_{h} in the SIDIS process

The following set of hadronic variables defined in GNS will be used throughout this work:

transverse momentum of the hadron : $$\boldsymbol{P}_{\mathbf{T}} \equiv \boldsymbol{P}_{\mathbf{h}} - \frac{(\boldsymbol{P}_{\mathrm{h}} \cdot \boldsymbol{q})\boldsymbol{q}}{|\boldsymbol{q}^2|} \;, \tag{1.7}$$

relative energy of the final state hadron z : $$z \equiv \frac{P \cdot P_{\mathrm{h}}}{P \cdot q} \;. \tag{1.8}$$

1.2 Cross-section and structure functions

The tree-level differential cross-section for SIDIS can be expressed in terms of structure functions $F_{\mathrm{XU,Z}}^{f(\phi_{\mathrm{h}})}$, which depend not only on quark flavour, type of hadron, x, and Q^2 as in description of DIS, but also on z and P_{T}. In the subscript, the letters 'XU,Z' denote the polarisation of the beam, the target, and optionally the virtual photon (L stands for longitudinal, T transverse, and U unpolarised).

$$\begin{aligned}\frac{\mathrm{d}\sigma}{\mathrm{d}x\mathrm{d}y\mathrm{d}z\mathrm{d}\phi_{\mathrm{h}}\mathrm{d}\boldsymbol{P}_{\mathbf{T}}^2} =& \frac{2\pi\alpha^2}{xyQ^2}\frac{y^2}{2(1-\varepsilon)}\left(1+\frac{\gamma^2}{2x}\right)\Big[F_{\mathrm{UU,T}} + \varepsilon F_{\mathrm{UU,L}} + \\ \sqrt{2\varepsilon(1+\varepsilon)}F_{\mathrm{UU}}^{\cos\phi_{\mathrm{h}}}\cos\phi_{\mathrm{h}} &+ \varepsilon F_{\mathrm{UU}}^{\cos 2\phi_{\mathrm{h}}}\cos 2\phi_{\mathrm{h}} + \lambda\sqrt{2\varepsilon(1+\varepsilon)}F_{\mathrm{LU}}^{\sin\phi_{\mathrm{h}}}\sin\phi_{\mathrm{h}}\Big] \;.\end{aligned} \tag{1.9}$$

Apart from the standard kinematical variables explained in section 1.1, beam polarization λ and coupling constant α, there are kinematical factors ε and γ:

$$\varepsilon = \frac{1 - y - \frac{1}{4}\gamma^2 y^2}{1 - y + \frac{1}{2}y^2 + \frac{1}{4}\gamma^2 y^2} \;, \qquad \gamma = \frac{2M_{\mathrm{N}}x}{Q} \;. \tag{1.10}$$

SIDIS is interesting to study because the transverse momentum of the final state hadron with origin in the struck quark reflects the intrinsic transverse momentum of the struck quark, as illustrated in figure 1.3. It holds that:

$$\boldsymbol{P}_{\mathbf{T}}\big|_{\mathrm{q}\to\mathrm{h}} = z\,\boldsymbol{k}_{\mathbf{T}}\big|_{\mathrm{q}} + \boldsymbol{P}_{\perp}\big|_{\mathrm{q}\to\mathrm{h}} \ , \tag{1.11}$$

where $\boldsymbol{k}_{\mathbf{T}}$ is the intrinsic transverse momentum of the quark q and $\boldsymbol{P}_{\perp}$ is the momentum gained in the process of fragmentation $\mathrm{q} \to \mathrm{h}$.

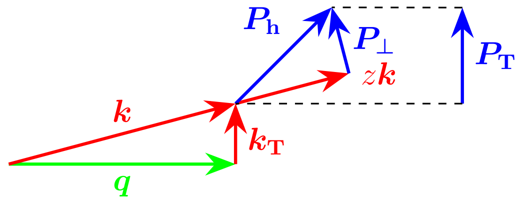

Figure 1.3: Origin of $\boldsymbol{P}_{\mathbf{T}}$ in SIDIS process

1.3 TMDs factorisation

It has been proven that if $P_{\mathrm{T}} \ll Q$ then we can factorize the SIDIS process into hard photon-quark scattering process and nonperturbative functions describing the distribution of quarks in the target or the fragmentation of a quark into the observed hadron, we can write the structure functions as weighted (denoting the weight as $w(\boldsymbol{k}_{\mathbf{T}}, \boldsymbol{P}_{\perp})$) convolutions of transverse momentum dependent parton distribution functions (TMD-PDFs) $f^{\mathrm{q}}(x, k_{\mathrm{T}}^2, Q^2)$ and transverse momentum dependent fragmentation functions (TMD-FFs) $D^{\mathrm{q}\to h}(z, P_{\perp}^2, Q^2)$ [12, 13, 14]:

$$F_{\mathrm{XU}}^{f(\phi_{\mathrm{h}})} = \mathscr{C}[wfD] = x\sum_{\mathrm{q}} e_{\mathrm{q}}^2 \int \mathrm{d}^2\boldsymbol{k}_{\mathbf{T}}\mathrm{d}^2\boldsymbol{P}_{\perp}\delta^{(2)}(z\boldsymbol{k}_{\mathbf{T}} + \boldsymbol{P}_{\perp} - \boldsymbol{P}_{\mathbf{T}})wf^{\mathrm{q}}D^{\mathrm{q}\to\mathrm{h}} \ . \tag{1.12}$$

Restricting ourselves to the sub-leading twist[2] and for $F_{\mathrm{UU}}^{\cos 2\phi_{\mathrm{h}}}$ neglecting quark-gluon-quark correlations (in the so-called Wilczek-Wandzura approximation [16]), the structure functions can be written as:

$$\begin{aligned}
F_{\mathrm{LU}}^{\sin\phi_{\mathrm{h}}} &= \mathscr{C}[\ldots] \ , \\
F_{\mathrm{UU,L}} &= 0 \ , \\
F_{\mathrm{UU,T}} &= \mathscr{C}[f_1 D_1] \ , \\
F_{\mathrm{UU}}^{\cos 2\phi_{\mathrm{h}}} &= \mathscr{C}\left[\frac{2(\hat{\boldsymbol{h}}\cdot\boldsymbol{k}_{\mathbf{T}})(\hat{\boldsymbol{h}}\cdot\boldsymbol{P}_{\perp}) - (\boldsymbol{k}_{\mathbf{T}}\cdot\boldsymbol{P}_{\perp})}{zMM_h} h_1^{\perp} H_1^{\perp}\right] \ , \\
F_{\mathrm{UU}}^{\cos\phi_{\mathrm{h}}} &= \frac{2M}{Q}\mathscr{C}\left[-\frac{(\hat{\boldsymbol{h}}\cdot\boldsymbol{k}_{\mathbf{T}})}{M} f_1 D_1 + \frac{k_{\mathrm{T}}^2(\hat{\boldsymbol{h}}\cdot\boldsymbol{P}_{\perp})}{zM^2M_h} h_1^{\perp} H_1^{\perp} + \ldots\right] \ .
\end{aligned} \tag{1.13}$$

where we considered only leading twist TMDs (f_1 is the unpolarised and $h_1^{\perp}$ the Boer–Mulders TMD-PDF, while D_1 is the unpolarised and $H_1^{\perp}$ the Collins

[2]Twist is a number related to mass dimension and spin, which determines the order of $\frac{1}{Q}$ at which transverse momentum dependent parton distribution functions (TMD-PDFs) appear in the factorization [15].

TMD-FF), defined $\hat{\boldsymbol{h}} = \frac{\boldsymbol{P_T}}{|\boldsymbol{P_T}|}$ and denoted '...' contributions that are zero in the chosen approximation. The terms of the type $-\hat{\boldsymbol{h}} \cdot \boldsymbol{k_T} f_1 D_1$ are often referred to as *Cahn effect*, which arises from the intrinsic transverse momentum of quarks in an unpolarised nucleon. In contrast, $\mathscr{C}[wh_1^{\perp}H_1^{\perp}]$ is called *Boer-Mulders effect*, describing a correlation between the transverse spin of quarks and their transverse momentum inside an unpolarised hadron [17].

The approximations in 1.13 hint at interesting properties that we expect to see from the results. Due to only higher-twist contributions to the $F_{\mathrm{LU}}^{\sin\phi_{\mathrm{h}}}$, we expect it to be compatible with zero. The same holds for $F_{\mathrm{UU,L}}$, in this case we define a simplifying notation $F_{\mathrm{UU,T}} + \varepsilon F_{\mathrm{UU,L}} \approx F_{\mathrm{UU,T}} \equiv F_{\mathrm{UU}}$. The most interesting is probably the Cahn effect in the $F_{\mathrm{UU}}^{\cos\phi_{\mathrm{h}}}$. Due to the suppression of the Boer-Mulders effect with a factor of $\frac{k_{\mathrm{T}}}{z}$ and negative weight of the Cahn effect in this particular case, this structure-function was predicted to be negative [17].

1.4 Models for TMDs

The simplest models assume that the transverse-momentum dependence of the unpolarised SIDIS TMDs introduced in the previous section, can be separated from the collinear part and parametrised as [18, 19]:

$$
\begin{aligned}
f(x, \boldsymbol{k_T}, Q^2) &= f(x, Q^2) \frac{\exp\left(\frac{-\boldsymbol{k_T}^2}{\langle \boldsymbol{k_T}^2 \rangle}\right)}{\pi \langle \boldsymbol{k_T}^2 \rangle} \ , \\
D(z, \boldsymbol{P}_{\perp}, Q^2) &= D(z, Q^2) \frac{\exp\left(\frac{-\boldsymbol{P}_{\perp}^2}{\langle \boldsymbol{P}_{\perp}^2 \rangle}\right)}{\pi \langle \boldsymbol{P}_{\perp}^2 \rangle} \ .
\end{aligned}
\tag{1.14}
$$

Flavour dependence was omitted for simplicity. This so-called *Gaussian ansatz* enables us to analytically compute the integrals in convolutions 1.13 and obtain a parametrisation of the structure functions. For example, F_{UU} is in the *Gaussian ansatz*:

$$
F_{\mathrm{UU}} = \sum_{\mathrm{q}} e_{\mathrm{q}}^2 x f_{\mathrm{q}}(x) D^{\mathrm{q}\to\mathrm{h}} \frac{\exp(-\frac{P_{\mathrm{T}}^2}{\langle P_{\mathrm{T}}^2 \rangle})}{\pi \langle P_{\mathrm{T}}^2 \rangle}
\tag{1.15}
$$

Parametrisations of the rest of the structure functions follow similar theoretical frameworks [19]. For SIDIS at higher energies, transverse-momentum dependence is no longer gaussian and different models for TMDs such as Collins-Soper-Sterman TMD evolution formalism are used [20].

1.5 Probing TMDs through unpolarised SIDIS measurments

1.5.1 Distributions of P_{T}^2

To describe P_{T}^2-distributions, we can use forumula 1.9 and integrate it over ϕ_{h} with the following result:

$$\frac{\mathrm{d}\sigma}{\mathrm{d}x\mathrm{d}y\mathrm{d}z\mathrm{d}\boldsymbol{P}_{\mathbf{T}}^{\mathbf{2}}} = \frac{4\pi^2\alpha^2}{xyQ^2}\frac{y^2}{2\,(1-\varepsilon)}(1+\frac{\gamma^2}{2x})F_{\mathrm{UU}}\ . \tag{1.16}$$

Note, that we used $F_{\mathrm{UU,T}} + \varepsilon F_{\mathrm{UU,L}} \approx F_{\mathrm{UU,T}} \equiv F_{\mathrm{UU}}$.

One can use the *Gaussian ansatz* to model F_{UU}, which further modifies the cross-section to the following form:

$$\frac{\mathrm{d}\sigma}{\mathrm{d}x\mathrm{d}y\mathrm{d}z\mathrm{d}\boldsymbol{P}_{\mathbf{T}}^{\mathbf{2}}} = \frac{4\pi^2\alpha^2}{xyQ^2}\frac{y^2}{2\,(1-\varepsilon)}(1+\frac{\gamma^2}{2x})\sum_{\mathrm{q}} e_{\mathrm{q}}^2 x f_{\mathrm{q}}(x) D^{\mathrm{q}\to\mathrm{h}} \frac{\exp\left(-\frac{P_{\mathrm{T}}^2}{\langle P_{\mathrm{T}}^2\rangle_{\mathrm{q}\to\mathrm{h}}}\right)}{\pi\langle P_{\mathrm{T}}^2\rangle_{\mathrm{q}\to\mathrm{h}}}\ . \tag{1.17}$$

The relation between $\langle P_{\mathrm{T}}^2\rangle$ and $\langle k_{\mathrm{T}}^2\rangle$ can be derived from 1.11 by squaring and averaging both sides of the equation while considering the angle between $\boldsymbol{k}_{\mathbf{T}}$ and $\boldsymbol{P}_{\perp}$ being random:

$$\langle P_{\mathrm{T}}^2\rangle_{\mathrm{q}\to\mathrm{h}} = z^2\langle k_{\mathrm{T}}^2\rangle_{\mathrm{q}} + \langle P_{\perp}^2\rangle_{\mathrm{q}\to\mathrm{h}}\ . \tag{1.18}$$

1.5.2 Modulations in ϕ_{h} distributions

It is inconvenient to directly fit the complicated formula for SIDIS cross-section as in eq. 1.9 on the measured ϕ_{h} distributions. For convenience, we define new coefficients called *azimuthal asymmetries* $A_{\mathrm{XU}}^{f(\phi_{\mathrm{h}})}$ as follows:

$$A_{\mathrm{XU}}^{f(\phi_{\mathrm{h}})}\left(x, z, P_{\mathrm{T}}^2, Q^2\right) \equiv \frac{F_{\mathrm{XU}}^{f(\phi_{\mathrm{h}})}}{F_{\mathrm{UU}}}\ . \tag{1.19}$$

Note, that we used $F_{\mathrm{UU,T}}+\varepsilon F_{\mathrm{UU,L}} \approx F_{\mathrm{UU,T}} \equiv F_{\mathrm{UU}}$. The inheritance of the properties of structure functions by the azimuthal asymmetries $A_{\mathrm{XU}}^{f(\phi_{\mathrm{h}})}$ becomes evident from equation 1.13. The characteristics of the unpolarised structure functions were discussed in the previous section 1.3.

The definition of azimuthal asymmetries and introduction of new kinematical factors

$$\varepsilon_1 = \frac{2(2-y)\sqrt{1-y}}{1+(1-y)^2}\ ,\quad \varepsilon_2 = \frac{2(1-y)}{1+(1-y)^2} \quad \text{and} \quad \varepsilon_3 = \frac{2y\sqrt{(1-y)}}{1+(1-y)^2} \tag{1.20}$$

simplifies the cross-section to the following formula:

$$\frac{\mathrm{d}\sigma}{\mathrm{d}x\mathrm{d}y\mathrm{d}z\mathrm{d}\phi_{\mathrm{h}}\mathrm{d}\boldsymbol{P}_{\mathbf{T}}^{\mathbf{2}}} = \sigma_0(1+\varepsilon_1 A_{\mathrm{UU}}^{\cos\phi_{\mathrm{h}}}\cos\phi_{\mathrm{h}} + \varepsilon_2 A_{\mathrm{UU}}^{\cos 2\phi_{\mathrm{h}}}\cos 2\phi_{\mathrm{h}} + \lambda\varepsilon_3 A_{\mathrm{LU}}^{\sin\phi_{\mathrm{h}}}\sin\phi_{\mathrm{h}})\ . \tag{1.21}$$

1.6 Extraction of TMDs from global fits

The COMPASS collaboration at CERN collected tens of millions of SIDIS events in several runs with polarised and unpolarised proton and deuteron targets. These events are analysed, azimuthal asymmetries and P_{T}^2-distributions are extracted.[3]

[3] Concerning unpolarised asymmetries and P_{T}^2-distributions, only the results from deuteron target were published by the moment of submission of this thesis [21, 22].

The connection between them and TMDs was explained in the previous sections of this chapter. A global fit is the final step of the path from measurement to the extraction of TMDs. External collaborations performing global fits, such as Multi-dimensional Analyses of Partonic distributions (MAP), compile data from various experiments, including COMPASS, to achieve the widest possible coverage in the $x : Q^2$ plane, as illustrated in figure 1.4. Notable experiments that are kinematically close to COMPASS are CLAS12 at Jefferson Laboratory (JLab) and HERMES at DESY. As an example of a result of a global fit, recent MAP results of f_1 and D_1 extraction are shown in figure 1.5.

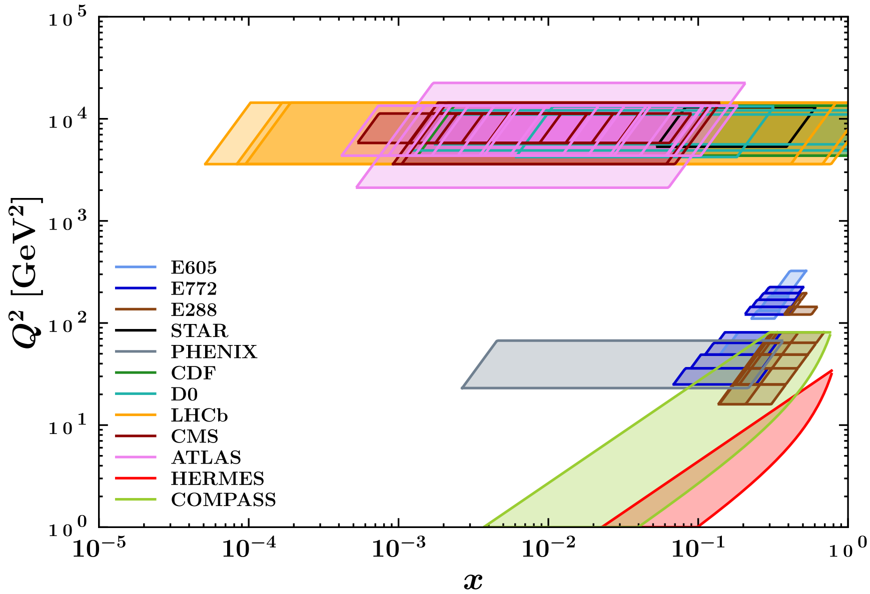

Figure 1.4: $x : Q^2$ coverage in the recent f_1 and D_1 extracted by MAP collaboration with the use of COMPASS data [23]

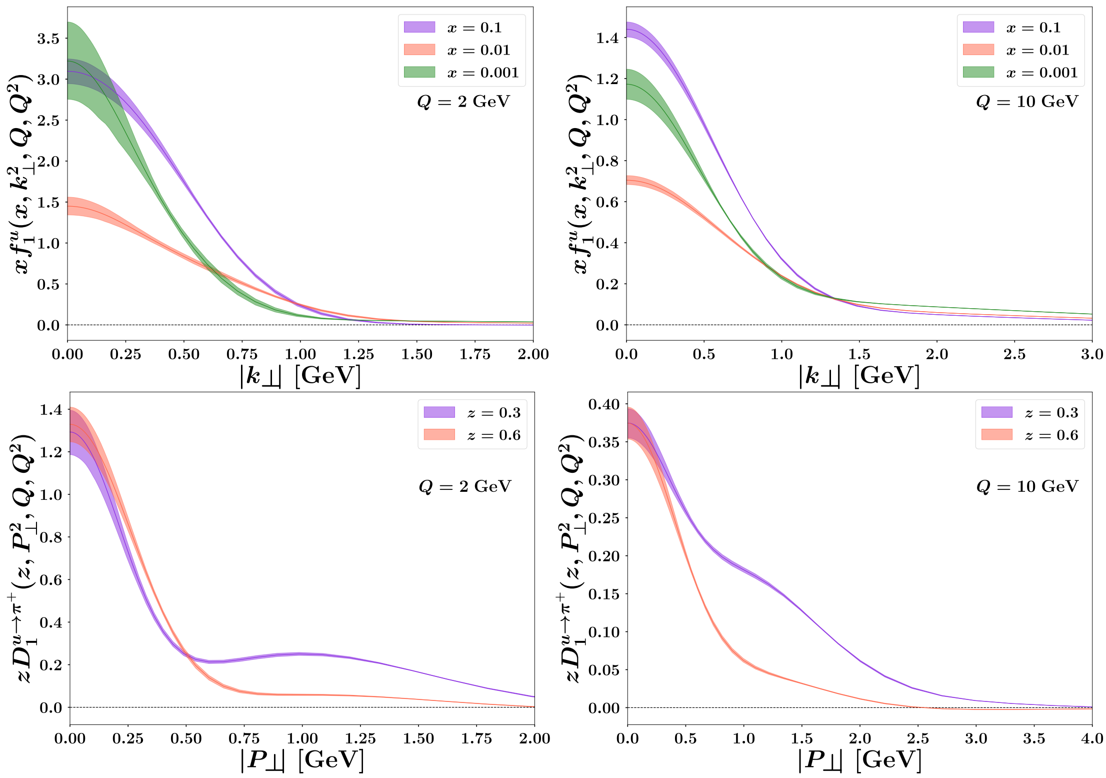

Figure 1.5: The dependence of f_1 and D_1 on the transverse momenta in the extraction by MAP collaboration [23]

2. Hadron identification at COMPASS experiment

Particle identification (PID) is a fundamental aspect of experimental particle physics, enabling the distinction between different types of particles produced in high-energy collisions or decays. PID is crucial for measurements of transverse momentum dependent parton distribution functions (TMD-PDFs), and also PDFs in general, because accurate identification of the particles produced in high-energy collisions or DIS is essential for isolating and interpreting the contributions of different partons to the internal structure of hadrons.

A particle can be identified by analysing its specific properties, such as momentum, energy, charge, and interaction signatures. For instance, detectors like the time-of-flight (TOF) system measure a particle's velocity by timing its travel across a known distance, while Cherenkov detectors exploit the emission of light that depends on the particle's velocity. In contrast, calorimeters and transmission radiation detectors (TRDs) identify particles based on their energy deposition and transition radiation, respectively. Each detection technique is optimised for specific particle types and energy ranges,

This chapter explores techniques relevant to this thesis and 2016 COMPASS spectrometer, and briefly introduces the basics of the spectrometer layout to the reader.

2.1 Basic principle of Cherenkov detectors

The key concept of Cherenkov detectors is the Cherenkov effect: the emission of radiation when a charged particle moves through a dielectric medium at a speed greater than the speed of light in that medium. This occurs because of the polarisation of atoms in the dielectric medium by the passing particle. As the atoms return to their equilibrium state, they emit coherent radiation, forming a characteristic Cherenkov cone. An illustration of the Cherenkov effect is in figure 2.1. The angle of emitted Cherenkov radiation, known as the Cherenkov angle θ_{C}, is given by

$$\cos\theta_{\mathrm{C}} = \frac{c}{nv} \; , \tag{2.1}$$

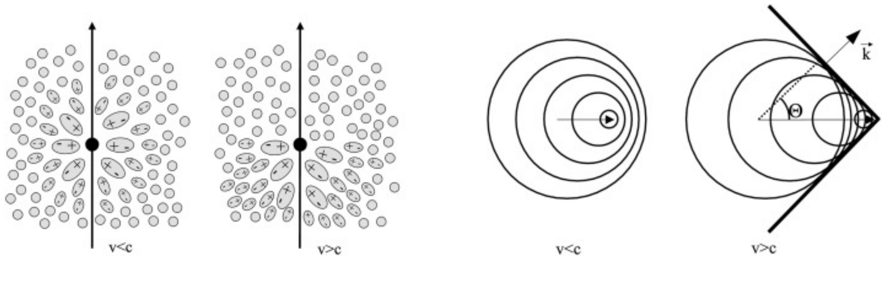

Figure 2.1: Polarisation of the medium due to passage of charged tracks with the velocity below and above $\frac{c}{n}$ (left). Illustration of the formation of the Cherenkov cone (right) [24].

where c is the speed of light in vacuum, v is the velocity of the charged particle, n is the refractive index of the medium [24]. At large velocities, $\cos\theta_{\mathrm{C}}$ gets saturated. A particle travelling faster than the speed of light in the medium must satisfy the following condition:

$$v > \frac{c}{n}\ . \tag{2.2}$$

This means that a threshold velocity for radiation emission exists, which depends on the properties of the medium [24]. If the particle's velocity is below this threshold, no Cherenkov radiation is produced. The threshold and saturation can be controlled by the choice of the medium (or its refractive index). Additionally, the medium has to be transparent to allow emitted Cherenkov photons to reach the photon detectors, which collect and measure Cherenkov photons. In some designs, mirrors or lenses focus Cherenkov light onto these detectors, which is an elegant solution with a better acceptance than trying to detect the Cherenkov photons directly from the cone. A special type of the Cherenkov detector – RICH uses parabolic mirrors that focus the photons into rings. The ring radius corresponding to θ_{C} is measured to identify the particle.

Some experiments, such as the Daya Bay Reactor Neutrino Experiment, use Cherenkov detectors as triggers vetos. In such cases, the detector operates with a binary readout. This allows for a simplified detector design and is useful for rejecting background signals. In the case of usage as a tool for PID, the Cherenkov angle is carefully measured to distinguish between different types of charged particles.

2.2 COMPASS spectrometer

Located in Building 888 at the CERN North Area, the COMPASS experimental setup has been operational for a record-breaking twenty years, delivering a wide range of measurements. Its versatility, from spectroscopy to nucleon structure studies, stems from its interchangeable fixed target and the flexibility in the choice of a hadronic or leptonic beam provided by the M2 beamline from Super Proton Synchrotron (SPS) and the wide-acceptance spectrometer with particle identification capabilities [25]. COMPASS experimental setup was inherited by its successor Apparatus for Meson and Baryon Experimental Research (AMBER), ensuring continuation of nucleon structure studies [26].

The experimental setup of the COMPASS experiment, as utilised in 2016 and 2017, is shown in Figure 2.2. The setup included an unpolarised liquid hydrogen target and a 160 GeV/c (anti)muon beam. The spectrometer was divided into two stages: a large angle Spectrometer (LAS) and a small angle spectrometer (SAS), designed to measure particles produced at large and small polar angles, respectively. Each stage consisted of tracking detectors positioned around a spectrometer magnet, followed by hadronic calorimeters (HCALs) and electromagnetic calorimeters (ECALs), with a muon filter located at the downstream end [25].

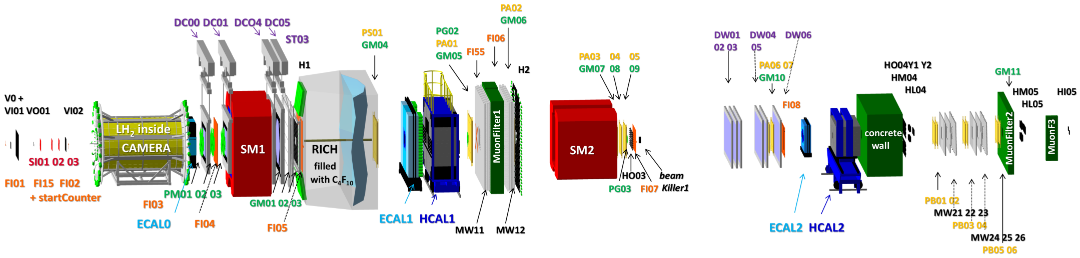

Figure 2.2: The 2016 setup of the COMPASS spectrometer, source: COMPASS collaboration

2.3 COMPASS RICH detector

The RICH detector is an integral component of the COMPASS LAS. Its vessel is filled with C_4F_{10} gas, which enables effective pion–kaon separation in the momentum range from the kaon Cherenkov threshold at approximately 10 GeV/c up to 40 GeV/c, beyond which the Cherenkov angle θ_C becomes saturated for both particles. This separation region is clearly visible in the two-dimensional histogram of $\theta_C : P_{RICH}$ shown in figure 2.3. Here, P_{RICH} is the momentum of the track extrapolated to the RICH detector.

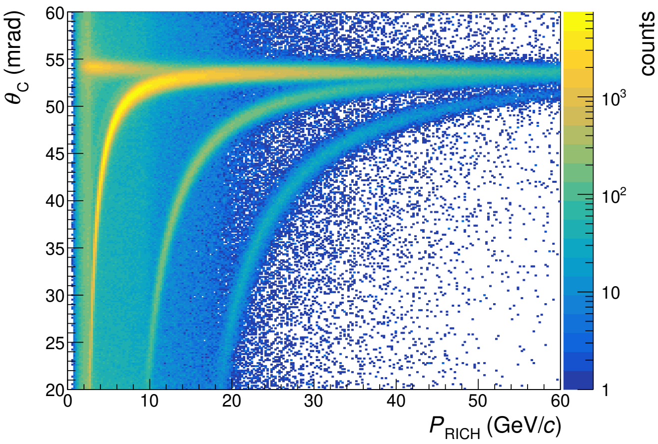

Figure 2.3: Reconstructed Cherenkov angle θ_C as a function of the momentum of hadron track extrapolated to RICH detector entrance P_{RICH}.

Thanks to its large dimensions, the RICH covers the full angular acceptance of the LAS, spanning approximately ±180 mrad in the vertical direction and ±250 mrad in the horizontal direction. The system utilises two spherical mirror arrays, positioned above and below the beamline, to reflect Cherenkov photons emitted by charged particles traversing the radiator gas. These reflected photons are then detected outside the spectrometer acceptance, as shown in figure 2.4. They are converted into electrons by a dedicated photodetection system (multi-wire proportional chambers (MWPCs), multi-anode photomultiplier tubes (MAPMTs) or micro pattern gaseous detectors (MPGDs)). Initially, from 2002 to 2004, the detector exclusively used MWPCs, with 16 MWPCs covering the entire detection surface. However, to accommodate the increased particle flux in the central region, four MWPCs were later replaced by an array of MAPMTs, while another four were substituted with micromesh gaseous structures (Micromegas) and gas electron multipliers (GEMs), further enhancing performance in high-intensity conditions.

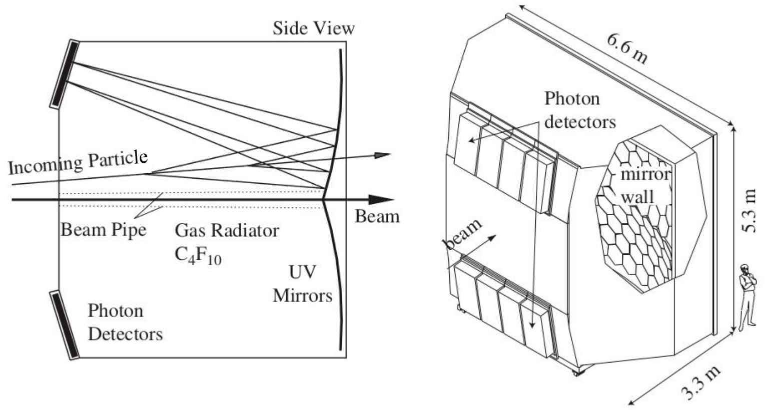

Figure 2.4: COMPASS RICH detector, source: COMPASS collaboration

Photodetectors measure Cherenkov photons, allowing for the reconstruction of their trajectory and the determination of the Cherenkov angle, θ_{C}. In reconstruction software, the expected photon pattern is calculated assuming different particle hypotheses and its likelihood is evaluated by comparing it to the detected pattern.

In the original proposal for the COMPASS experiment, a second RICH detector was planned for the SAS, intended to occupy the space between the trackers following SM2 [27]. However, this detector has never been constructed due to financial constraints.

2.3.1 Likelihood tagging

The primary role of the RICH detector is to assign a hadron type to each reconstructed track. In the simplest approach, the particle type is assigned based on the highest likelihood $\mathscr{L}_{\mathrm{max}}$. To reduce misidentification, stricter cuts are applied to the ratios of the maximum to the second-highest likelihood $\mathscr{L}_{\mathrm{2nd}}$ and to the background likelihood $\mathscr{L}_{\mathrm{bckg}}$. The thresholds for likelihoods are empirically optimised to maximise the detector's performance and may vary between data-taking years. The specific likelihood limits used for the 2016 RICH detector in this analysis are listed in table 2.1, and were selected based on previous performance studies of the 2016 COMPASS RICH data. The efficiency of the RICH likelihood tagging is evaluated in chapter 3.

criterium	π	K
$\mathscr{L}_{\mathrm{max}}$	$\mathscr{L}_{\pi}$	$\mathscr{L}_{\mathrm{K}}$
$\mathscr{L}_{\mathrm{max}}/\mathscr{L}_{\mathrm{2nd}}$	> 1.02	> 1.08
$\mathscr{L}_{\mathrm{max}}/\mathscr{L}_{\mathrm{bckg}}$	> 2.02	> 2.08

Table 2.1: Selection criteria on likelihood for PID using RICH detector.

2.4 Calorimetry for hadron identification at COMPASS

Cherenkov radiation is an effect based on polarisation of the dielectric by charged particles. For that reason, neutral hadron identification relies on their interactions with calorimeters, where they deposit energy through cascade of hadronic and electromagnetic processes called *hadronic* and *electromagnetic showers*. Hadronic showers in calorimeters are more complex than electromagnetic showers due to the variety of secondary interactions, including breaking of nucleus, pion production, and fluctuations in shower development. Calorimetry typically involves two key types of calorimeters: ECAL and HCAL.

Electromagnetic processes dominate in ECAL, which is primarily used to detect photons from neutral meson decays such as π^0. COMPASS setup has 3 homogeneous or sampling ECAL stations numbered from 0 to 2.

Hadronic calorimeters (HCALs) are designed to measure energy deposition from strongly interacting particles. COMPASS setup has 2 sampling HCAL stations numbered from 1 to 2.

3. Extracting RICH efficiencies

The only hadronic products of the SIDIS process stable enough to be detected in COMPASS spectrometer are $\pi^{\pm}$, $\mathrm{K}^{\pm}$, p and $\bar{\mathrm{p}}$ [25, 28]. The number of identified (anti)protons is insufficient for further analysis of azimuthal asymmetries. For that reason, we excluded p and $\bar{\mathrm{p}}$ from the analysis.

The particles are identified using COMPASS RICH1 detector. This detector is not included in the Monte Carlo (MC) simulation, thus we extract RICH performance from the data. It is characterised by efficiency (detection probability) and purity (misidentification probability), both evaluated for each hadron separately. Obtained numbers $\epsilon(i \to j)$, which will be defined in section 3.2 are usually organised in the so-called *efficiency-purity matrix* (protons are neglected):

$$M_{\mathrm{RICH}} = \begin{pmatrix} \epsilon(\pi \to \pi) & \epsilon(\mathrm{K} \to \pi) \\ \epsilon(\pi \to \mathrm{K}) & \epsilon(\mathrm{K} \to \mathrm{K}) \\ \epsilon(\pi \to \text{no ID}) & \epsilon(\mathrm{K} \to \text{no ID}) \end{pmatrix} . \tag{3.1}$$

This matrix is usually evaluated in P_{RICH} (momentum of the track extrapolated to the RICH detector) and θ_{RICH} (polar angle of the track extrapolated to the RICH detector) bins to describe the dependencies on these variables. Analysis of 2016 RICH performance can be found in ref. [29]. For this analysis, we try to adjust the standard binning and exploit the dependence on ϕ_{h}. To do this, it is necessary to have a source of events where the true kind of the particle passing the RICH is known. In the case of COMPASS analysis, the following two-body decays are used:

$$\begin{aligned} \phi^0(1020) &\to \mathrm{K}^+\mathrm{K}^- , \\ \mathrm{K}^0 &\to \pi^+\pi^- . \end{aligned} \tag{3.2}$$

A detailed description of the process of extracting the efficiency-purity matrix is in the following sections.

3.1 Data selection and binning

In 2016, the RICH detector was operational only in periods P06–P10. The event selection is the same as the main analysis, except for excluding the DIS kinematic selection (apart from the y cut) and the hadron selection, which is done separately according to the decay mode studied. Additionally, RICH cuts are applied, ensuring the correct kinematical range for RICH operation. First, we require the track extrapolated in the detector setup to RICH entrance to have polar angle $0.01 < \theta_{\mathrm{RICH}} < 0.12$ and $\left|\frac{\mathrm{d}Y}{\mathrm{d}Z}\right| < 0.08$ to avoid regions of low photon detection efficiency (θ_{RICH} determines the region into which the photon ring is projected) and the region of MPGD, which were newly installed and not yet fully operational in 2016. Hadron momentum is restricted 4 GeV$< P_{\mathrm{RICH}} < 40$ GeV. We reject tracks passing the RICH beam pipe (corresponds to $R > 5$ cm around the nominal beam axis). The same selection criteria are applied to the hadrons to be identified in the SIDIS analysis. As the RICH performance was shown to depend only on these quantities, the efficiency-purity matrix obtained from the decays can be used in SIDIS.

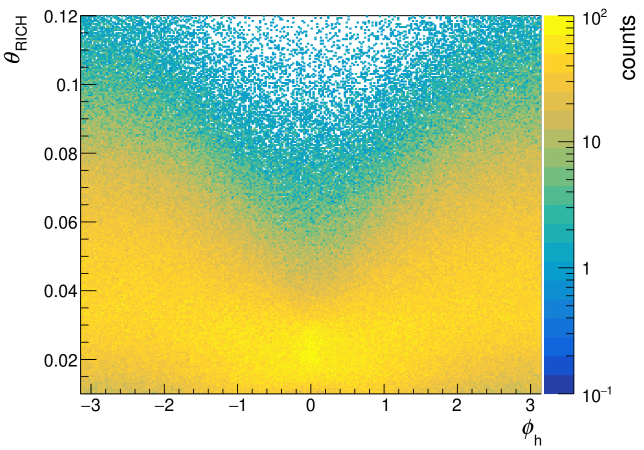

Figure 3.1: Correlation between θ_{RICH} and ϕ_h of all SIDIS hadron candidates.

To select a reasonably pure sample of hadrons from the decays 3.2, we demand $Z_{\mathrm{Last}} > Z_{\mathrm{SM1}}$ to ensure good momentum resolution and $P_{\mathrm{T}} > 23$ MeV to suppress the electron background. Electron veto cut $\frac{\mathscr{L}_e}{\mathscr{L}_\pi} < 1.8$ is also applied to purify the sample. Furthermore, we require that at least one of the two hadrons from the decay is correctly tagged by the RICH detector. The track of the other hadron then enters the efficiency–purity determination.

The binning was inspired by the previous analyses of RICH performance in 2016. Normally, a very fine binning in P_{RICH} is chosen and supported by two bins in θ_{RICH}. In this analysis, we must also describe the dependence on ϕ_{h} to remove false modulations from ϕ_{h} distributions caused by non-trivial dependence of the efficiency on P_{RICH} and ϕ_{h}. The results of the previous analyses suggest that the efficiencies are not hadron-charge dependent and constant in the region $15 < P_{\mathrm{RICH}} < 30$ [29]. The distribution of hadrons in their ϕ_{h} dependence is symmetric and correlated with θ_{RICH} as can be seen in the figure 3.1. All these observations resulted in the choice of binning limits as listed in table 3.1. The first two bins in P_{RICH} are omitted in the case of kaons because they lie below the Cherenkov threshold.

bin no.		1		2		3		4		5		6	
P_{RICH}/ GeV	4	–	7	–	10	–	15	–	21	–	30	–	40
θ_{RICH}	0.01	–	0.04	–	0.12								
$\lvert\phi_{\mathrm{h}}\rvert$	0	–	$\frac{\pi}{8}$	–	$\frac{\pi}{3}$	–	$\frac{2\pi}{3}$	–	π				

Table 3.1: Binning limits for extraction of RICH efficiencies.

3.2 Methodology of extraction of the efficiency–purity matrix

The definition of the probabilities $\epsilon(i \to j)$ is evaluated considering the following matrix equation:

$$M_{\mathrm{RICH}} \begin{pmatrix} N_{\pi,\mathrm{true}} \\ N_{\mathrm{K},\mathrm{true}} \end{pmatrix} = \begin{pmatrix} N_{\pi} \\ N_{\mathrm{K}} \\ N_{\mathrm{noID}} \end{pmatrix} , \tag{3.3}$$

where counts measured using RICH are unindexed, true counts are denoted with the index *true*. The extraction of individual matrix elements is possible because in theory, what we select as $\phi^0 \to \mathrm{K}^+\mathrm{K}^-$ provides a pure sample of kaons ($N_{\pi,\mathrm{true}} \approx 0$), while $\mathrm{K}^0 \to \mathrm{K}^+\mathrm{K}^-$ should yield a pure sample of pions ($N_{\mathrm{K},\mathrm{true}} \approx 0$). Due to that, matrix elements are evaluated as:

$$\epsilon(i \to j) N_{i,\mathrm{true}} = N_{ij} , \tag{3.4}$$

where $N_{i,\mathrm{true}}$ is the total amount of signal and N_{ij} is the amount of signal for case j from the following 3 hypotheses:

1. The hadron will be identified correctly (amount of signal labelled N_{ij} with $j = i$).
2. The hadron will be misidentified as another particle that is being identified. (amount of signal labelled N_{ij} with $j \neq i$ while $j \in \{\pi, \mathrm{K}\}$).
3. The hadron will not be classified as π or K (amount of signal labelled N_{ij} with $j \notin \{\pi, \mathrm{K}\}$).

While the value of N_{ij} represents the counts of hadrons given by RICH tagging (see section 2.3.1 of chapter 2), $N_{i,\mathrm{true}}$ represents the 'true' counts for hadron i in the data sample.

An empirically chosen function is then fitted to the reconstructed mass distributions. The choice of the function depends on the kind of decay and the shape of the background in the given kinematics. First, the fit is performed on all the previously listed cases together to fix some parameters of the fit and define the total amount of the signal in the data (N_i). The chosen function (with some parameters fixed) is then simultaneously fitted on all three cases separately, obtaining the amount of signal (N_{ij}) for each of the three cases mentioned above.

In this work, we estimate the counts using amplitudes of signal part of the fitting function. Specifically, $N_{i,\mathrm{true}} \equiv A_0$ the total amplitude and the amplitudes for 3 possible (mis)identification cases $N_{ij} \equiv A_j$, $j \in \{1, 2, 3\}$. Parameters that are not fixed from the fit of all histograms together are indexed with i in formulae in the following sections. Knowing that $\sum_i \epsilon(i \to j) = 1$, we demand the following condition while performing the fits:

$$A_0 = A_1 + A_2 + A_3 . \tag{3.5}$$

3.3 $\phi^0 \to \mathrm{K}^+\mathrm{K}^-$

$\phi^0(1020)$ with a decay width of $\Gamma_\phi = 4.249(13)$ MeV is decaying too fast for the secondary vertex to be reconstructed [28]. The search for its decay begins in the outgoing tracks of a primary vertex with at least 3 outgoing tracks. We exclude muons and select pairs of hadrons of opposite charges.

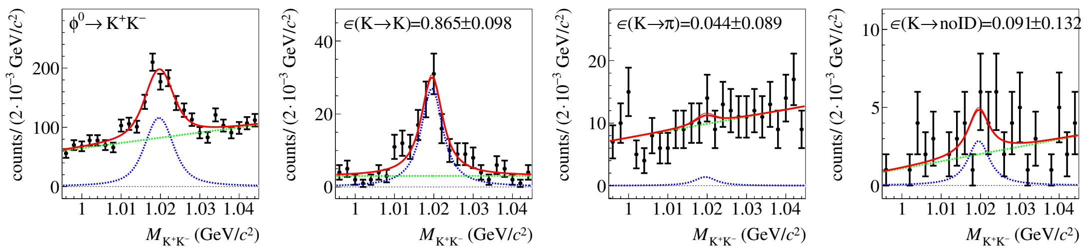

Figure 3.2: Example of simultaneous fits of peaks in the invariant mass of ϕ^0 for bin $P_{\mathrm{RICH}} \in [21, 30]$ GeV, $\theta_{\mathrm{RICH}} \in [0.01, 0.04]$ and $|\phi_{\mathrm{h}}| \in [\frac{2\pi}{3}, \pi]$. The full fitting function is shown in red, with the background component depicted as a green dashed line and the signal component as a blue dashed line.

The fitting function was chosen according to the previous analyses of RICH performance as:

$$
\begin{aligned}
f_i(M, A_i, &B_i, C_i; \mu, \sigma_1, \sigma_2) = \\
&\underbrace{A_i \left[\frac{1}{\sqrt{2\pi}\sigma_1} \exp\left(-\frac{(M-\mu)^2}{2\sigma_1^2} \right) \frac{1}{\pi} \frac{\frac{\sigma_2}{2}}{(M-\mu)^2 + (\frac{\sigma_2}{2})^2} \right]}_{\text{signal}} \\
&\qquad\qquad\qquad\qquad \underbrace{+ B_i M^2 + C_i M + D_i}_{\text{background}} \; .
\end{aligned} \tag{3.6}
$$

An example of the fit of the invariant mass of $\phi^0 \to K^+K^-$ is shown in figure 3.2.

3.4 $K^0 \to \pi^+\pi^-$

In the case of the K^0 decay, which is a mixed state of short(er)-lived K^0_S and long(er)-lived K^0_L with decay widths of the order of 10^{-11} and 10^{-9} MeV [28], reconstruction of the secondary vertex is possible. K^0 decay candidate is a secondary vertex with an incoming track connected to the primary vertex ($\theta \leq 0.01$) separated by more than 2σ from other vertex candidates and with at least two oppositely charged outgoing tracks, which are not associated with any other primary vertex. The hadron tracks have to travel less than 10 radiation lengths in the spectrometer. Finally, the difference between K^0 candidate invariant mass and K^0 true mass must be smaller than 150 MeV/c^2.

The fitting function was chosen according to the previous analyses of RICH

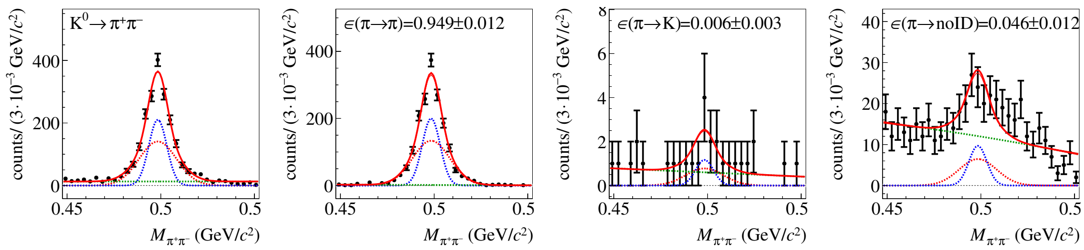

Figure 3.3: Example of simultaneous fits of peaks in the invariant mass of K^0 for the bin $P_{\text{RICH}} \in [21, 30]$ GeV, $\theta_{\text{RICH}} \in [0.01, 0.04]$ and $|\phi_{\text{h}}| \in [\frac{2\pi}{3}, \pi]$. The full fitting function is shown in red, with the background component depicted as a green dashed line and the 2 Gaussian parts of the signal component as a blue and red dashed line.

performance as:

$$\begin{aligned} f_i(M, A_i, &B_i, C_i; \mu, \sigma_1, \sigma_2, \delta) = \\ &\underbrace{A_i \left[\delta \exp\left(-\frac{(M-\mu)^2}{2\sigma_1^2} \right) + (1-\delta) \exp\left(-\frac{(M-\mu)^2}{2\sigma_2^2} \right) \right]}_{\text{signal}} \\ &\qquad\qquad\qquad\qquad + \underbrace{B_i M^2 + C_i M + D_i}_{\text{background}} \ . \end{aligned} \tag{3.7}$$

An example of the fit of the invariant mass of $K^0 \to \pi^+\pi^-$ is given in figure 3.3.

3.5 Results

The final results for $P_{\text{RICH}} : \theta_{\text{RICH}} : \phi_{\text{h}}$ dependent efficiency-purity matrix elements are presented in figure 3.5 for $\epsilon(\text{K} \to j)$ and in figure 3.4 for $\epsilon(\pi \to j)$. The results show a dependence of the efficiencies on P_{RICH}, θ_{RICH}, which was expected from the previous analyses of the RICH performance. Dependence on ϕ_{h} is also visible; the efficiency is the worst on low $|\phi_{\text{h}}|$, in the $[0, \frac{\pi}{8}]$ bin, which corresponds to the region usually neglected from the SIDIS azimuthal fits due to high contamination with Bremsstrahlung electrons (see 4.7). Due to the poor efficiency, we will neglect this region in the analysis of identified hadrons as well. Note that $\epsilon(i \to \text{no ID})$ also includes misidentifications to protons and antiprotons.

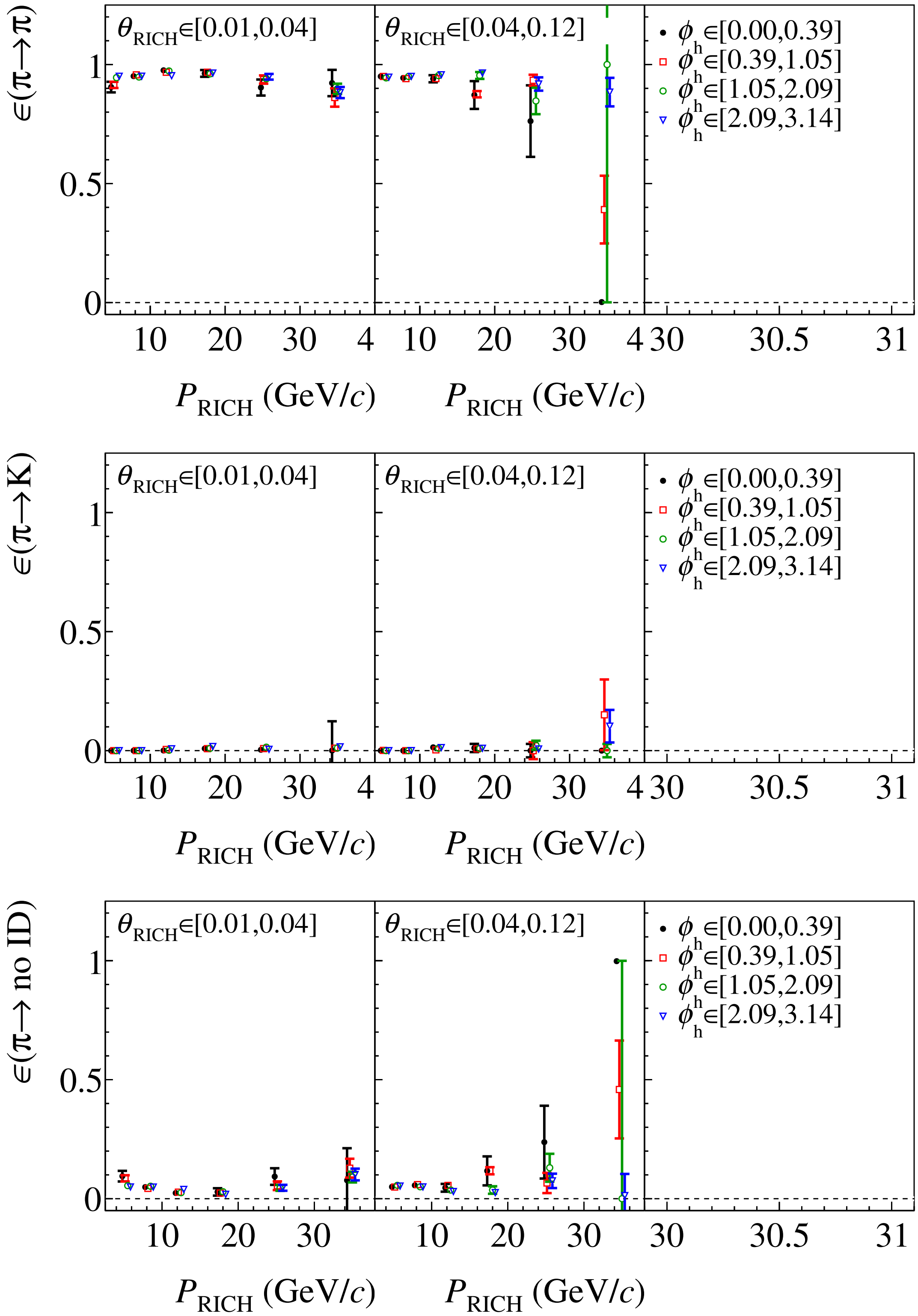

Figure 3.4: Results for elements $\epsilon(\pi \rightarrow j)$ of the efficiency-purity matrix in $P_{\text{RICH}} : \theta_{\text{RICH}} : \phi_{\text{h}}$ dependence.

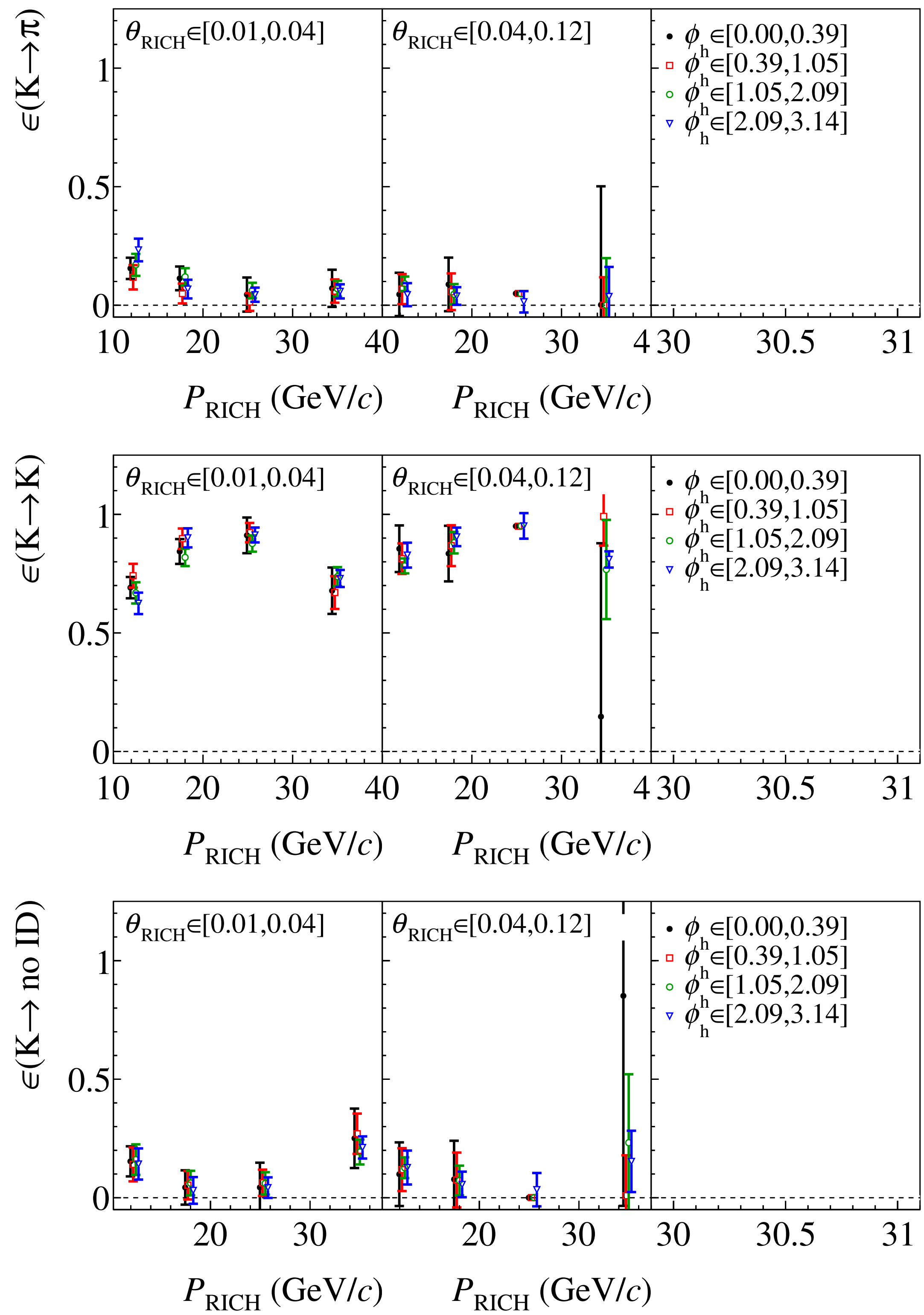

Figure 3.5: Results for elements $\epsilon(\mathrm{K} \to j)$ of the efficiency-purity matrix in $P_{\mathrm{RICH}} : \theta_{\mathrm{RICH}} : \phi_{\mathrm{h}}$ dependence.

4. Measurement of azimuthal asymmetries and P_{T}^2-distributions of charged hadrons

This chapter provides a comprehensive overview of the analysis. First, technical aspects such as event and hadron selection, as well as the fitting procedure, are discussed in sections 4.1–4.3. Subsequently, various corrections applied to the data are presented in sections 4.4–4.7. Except for a few additional technical details, the procedure for extracting results is identical for analyses with and without hadron identification.

4.1 Data sample and selection

This analysis works with 2016 COMPASS data, specifically with periods P04–P09. We use trees with reconstructed events, which have been pre-filtered asking for at least one primary vertex with well-measured beam momentum and for at least one scattered μ candidate that leads to $Q^2 > 0.8$ (GeV/c)^2 as input. These trees are processed with physics analysis software tools (PHAST) – a framework for data analysis of the COMPASS and AMBER experiments. More about the structure of storage and processing of the measured and reconstructed data can be found in ref. [30, 31].

The requirements for the events upon the data selection can be split into the following sections. All selection steps and their effect on the measured data are listed in tables 4.1 and 4.2. The kinematic coverage of this analysis is demonstrated in $x : Q^2$ and $z : P_{\mathrm{T}}$ planes in figure 4.1.

Vertex selection

In each event PHAST selects *the best* the primary vertex according to the highest number of outgoing tracks and if equal the lower vertex χ^2. Additionally, the position of the best primary vertex is asked to be within the target (-325 cm $< Z_{\mathrm{vert}} < -71$ cm as the longitudinal cut, $Y_{\mathrm{vert}} < 1.2$ cm as the vertical cut, $R_{\mathrm{vert}} < 1.9$ cm as the radial one, and 2 cm as the `RMC_cut` parameter).

Beam track selection

The beam momentum and the track fit reduced χ^2 have to be within the usual limits of $\frac{\chi^2_\mu}{n_{\mathrm{df}}}$ to remove very poorly reconstructed tracks. The extrapolated beam track should cross the whole target length. In addition, already in the μDST pre-selection, we required $\sigma_{P_\mu} < 4$ GeV/c to avoid events with beam tracks with momentum not reconstructed by beam momentum station (BMS).

Scattered muon cuts

The scattered muon is required to be the only muon outgoing from the primary vertex, it must also point to a trusted region of trigger hodoscopes (to ensure correspondence with the MC simulation). It is demanded that the scattered muon travels at least 30 radiation lengths in the spectrometer. The usual limit $\frac{\chi^2_{\mu'}}{n_{\mathrm{df}}} < 10$ for reconstructed track quality is applied. Additionally, the track must have hits both before and after the SM1 to ensure reliable momentum reconstruction. A few remaining ambiguous events are rejected when any track with the same charge as μ' outgoing from the primary vertex is found with Z_{Last} downstream of MF2 (33 m) or pointing to the absorber beam hole.

Kinematic selection

We apply basic requirements ensuring the DIS regime. For rejection of events with poorly reconstructed virtual-photon energy we demand $y > 0.1$. To avoid large electromagnetic radiative corrections we demand $y < 0.9$. Basic kinematics limits on Bjorken x variable ($0.003 < x < 0.130$) have been applied according to the acceptance of the COMPASS spectrometer. In addition, $\theta_\gamma < 60$ mrad was imposed, where θ_γ is calculated in the laboratory system with respect to the direction of the incoming muon. This requirement, which was implemented already for analysis of unpolarised measurements on deuteron from 2004, is used to avoid large acceptance correction [6]. As the hadrons are distributed around the virtual photon direction, if θ_γ is large, the hadron is more likely to go out of the geometrical acceptance, thus introducing spurious azimuthal modulations.

Hadron selection

Standard requirements on the quality of tracks and the number of radiation lengths crossed in the spectrometer have been imposed. The current fragmentation regime, where the struck quark undergoes fragmentation into observable hadrons, as opposed to hadrons originating from the remnants of the target nucleon, is ensured by requesting $z > 0.1$. A sufficient azimuthal angle resolution is secured by demanding $P_{\mathrm{T}} > 0.1$ GeV/c.

Bad spill and bad run selection

Bad spill and bad run selection is a process of identifying and removing spills or runs with problems in data taking. Various techniques are applied to purify the data sample, from selecting runs with empty spills to checking the mean values of defined variables [32]. Run-by-run stability of selected kinematic distributions was monitored using the unbinned Kolmogorov–Smirnov test. This thesis does not include an independent stability analysis; instead, validated spill and run quality lists provided by colleagues were employed to ensure data reliability.

cut	P04	P05	P06	P07	P08	P09
All events	15271729 100.00	14063438 100.00	13088846 100.00	16752829 100.00	17673546 100.00	13799026 100.00
events with BPV	15271729 100.00	14063438 100.00	13088846 100.00	16752829 100.00	17673546 100.00	13799026 100.00
BPV in target	8022872 52.53	7406063 52.66	6902914 52.74	8896463 53.10	9273872 52.47	7272769 52.70
$\sigma_{P_\mu} < 4$ GeV/c	7963480 52.15	7338812 52.18	6827227 52.16	8845685 52.80	9221955 52.18	7236676 52.44
140 GeV/c $< P_\mu <$ 180 GeV/c	7963393 52.14	7338743 52.18	6827156 52.16	8845532 52.80	9221799 52.18	7236552 52.44
$\frac{\chi^2_\mu}{n_{\mathrm{df}}} < 10$	7963335 52.14	7338691 52.18	6827119 52.16	8845496 52.80	9221759 52.18	7236527 52.44
μ crosses the whole target	7726456 50.59	7123670 50.65	6628226 50.64	8577464 51.20	8919450 50.47	7001982 50.74
μ' selection (`Hodohelper`)	4951267 32.42	4521646 32.15	4249693 32.47	5450613 32.54	5772122 32.66	4634030 33.58
$\frac{\chi^2_{\mu'}}{n_{\mathrm{df}}} < 10$	4949255 32.41	4520214 32.14	4248346 32.46	5449139 32.53	5770541 32.65	4632793 33.57
$Z_{\mathrm{First}} < 3, 5$ m $< Z_{\mathrm{Last}}$	4947076 32.39	4518185 32.13	4247106 32.45	5447723 32.52	5768961 32.64	4631503 33.56
$Z_{\mathrm{Last}} < 33$ m and $Q \neq Q_{\mu'}$	4937671 32.33	4509486 32.07	4238742 32.38	5437183 32.46	5757965 32.58	4622899 33.50
$Q^2 > 1$ (GeV/c)^2	3906664 25.58	3589343 25.52	3399938 25.98	4361761 26.04	4666608 26.40	3714176 26.92
$W > 5$ GeV/c	2061815 13.50	1872194 13.31	1801140 13.76	2287709 13.66	2407020 13.62	1913338 13.87
$0.003 < x < 0.130$	1939110 12.70	1760689 12.52	1687322 12.89	2143229 12.79	2256755 12.77	1789097 12.97
$0.1 < y < 0.9$	1754279 11.49	1600782 11.38	1536119 11.74	1956240 11.68	2061623 11.67	1633684 11.84
$\theta_\gamma < 60$ mrad	1475537 9.66	1346876 9.58	1291619 9.87	1645285 9.82	1721363 9.74	1367470 9.91
Triggers: `LT | MT | OT | LAST`	1475537 9.66	1346876 9.58	1291619 9.87	1645285 9.82	1721363 9.74	1367470 9.91

Table 4.1: Effect of the DIS cuts on each analysed period of 2016 data (number on the top of each row corresponds to the number of events, number on the bottom is events percentage).

cut	P04	P05	P06	P07	P08	P09
All tracks without μ'	4122185 100.00	3821416 100.00	3681923 100.00	4688169 100.00	4872897 100.00	3881648 100.00
$\frac{X}{X_0} < 10$	4066840 98.66	3789962 99.18	3651890 99.18	4650205 99.19	4833599 99.19	3850656 99.20
hadron track $\frac{\chi^2}{n_{\mathrm{df}}} < 10$	4015702 97.42	3740062 97.87	3602690 97.85	4589790 97.90	4771170 97.91	3795400 97.78
$Z_{\mathrm{First}} < 350$ cm	4006743 97.20	3732143 97.66	3594485 97.63	4579866 97.69	4760744 97.70	3787100 97.56
$Z_{\mathrm{Last}} > 350$ cm	3886296 94.28	3622924 94.81	3489401 94.77	4451005 94.94	4625963 94.93	3678798 94.77
$0.1 < z < \infty$	2029167 49.23	1874938 49.06	1790001 48.62	2284855 48.74	2392543 49.10	1896568 48.86
0.1 GeV$< P_{\mathrm{T}} < \infty$	1919711 46.57	1774662 46.44	1694315 46.02	2162496 46.13	2263819 46.46	1795059 46.24
DVM cut	1864772 45.24	1723487 45.10	1646840 44.73	2101415 44.82	2199376 45.13	1743933 44.93
BS and BR rejection	1738469 42.17	1561890 40.87	1538473 41.78	1945645 41.50	1983596 40.71	1664088 42.87

Table 4.2: Effect of the hadron cuts on each analysed period of 2016 data (number on the top of each row corresponds to the number of events, number on the bottom is events percentage).

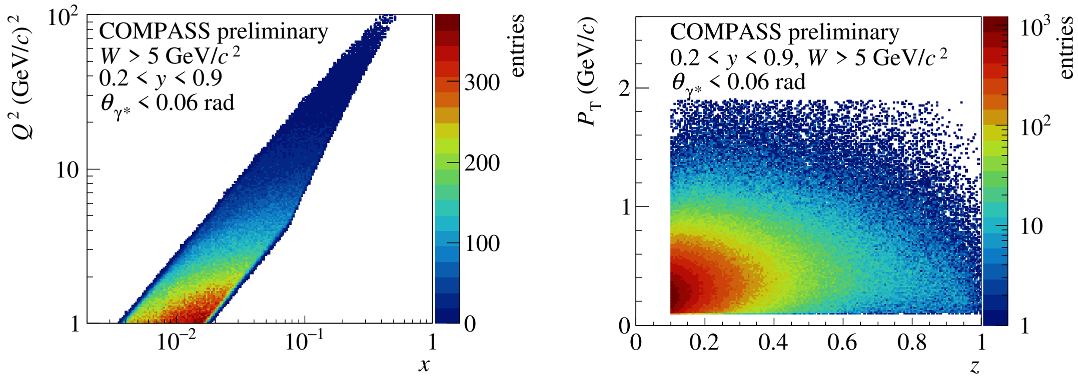

Figure 4.1: Kinematical coverage in $x : Q^2$ and $z : P_{\mathrm{T}}$ planes

4.1.1 Additional selection for PID

For analysis of azimuthal asymmetries and P_{T}^2-distributions of identified hadrons, only periods P07–P09 can be used due limited operational window of RICH detector and systematic effects observed in the analysis of multiplicities [9]. As explained in section 2.3 COMPASS RICH detector allows us to identify $\pi^{\pm}$, $\mathrm{K}^{\pm}$, p and $\bar{\mathrm{p}}$. Reasonable ring recognition is possible only in certain kinematics, further narrowing the data selection with demands on the track extrapolated in the detector setup to RICH entrance. First, we require the track to have $0.01 < \theta_{\mathrm{RICH}} < 0.12$ and $\left|\frac{\mathrm{d}Y}{\mathrm{d}Z}\right| < 0.08$. Hadron momentum is restricted 4 GeV$< P_{\mathrm{RICH}} < 40$ GeV. Tracks passing the beam pipe (corresponding to radius limit $R < 5$ cm around the nominal beam axis) are rejected. The effect of the cuts on the number of events is presented in table 4.3. Since the time component of the 4-momentum of pion and kaon differs, there is a slight difference in z when considering K or π hypothesis. In the analysis without identification, the pion mass hypothesis was used for all hadrons, which is the reason why table 4.3 also contains lines with $0.1 < z < \infty$ and consequently 0.1 GeV$< P_{\mathrm{T}} < \infty$ cut, which differ from the lines in table 4.2.

cut	P07	P08	P09
$0.1 < z < \infty$	2284871 48.74	2392555 49.10	1896575 48.86
0.1 GeV$< P_{\mathrm{T}} < \infty$	2162512 46.13	2263829 46.46	1795066 46.24
4 GeV$< P_{\mathrm{RICH}} < 40$ GeV	1907990 40.70	1997970 41.00	1583955 40.81
$\|\mathrm{d}Y/\mathrm{d}Z\| < 0.08$	1855841 39.59	1943808 39.89	1541313 39.71
$0.01 < \theta_{\mathrm{RICH}} < 0.12$	1671271 35.65	1750580 35.92	1388777 35.78
$R > 5$ cm	1641663 35.02	1720097 35.30	1364248 35.15
DVM cut	1601607 34.16	1677588 34.43	1330750 34.28

Table 4.3: Effect of the RICH cuts on each analyzed period of 2016 data. The table contains the number of hadrons (top of row) and the corresponding percentage concerning the table 4.2 (bottom of row).

Hadrons that passed event selection are now identified using RICH detector. The limits on the likelihoods of being pion $\mathscr{L}_{\pi}$, kaon $\mathscr{L}_{\mathrm{K}}$ or background $\mathscr{L}_{\mathrm{bckg}}$

that are required to identify the particle as $\pi^{\pm}$ and $K^{\pm}$ are in table 2.1. The final numbers of identified π, K are in table 4.4 together with the number of particles discarded by electron veto cut N_{veto} and the number of particles that did not pass the condition to be classified as π or K (N_{noID}).

	P07	P08	P09
N_{π}	1255408 78.38	1312066 78.21	1042243 78.32
N_{K}	129400 8.08	134198 8.00	107271 8.06
N_{noID}	182034 11.37	195517 11.65	153376 11.53
N_{veto}	34765 1.74	35807 2.13	27860 2.09

Table 4.4: Number of identified hadrons (N_{π} and N_{K}), particles discarded by electron veto cut (N_{veto}) and number of hadrons, for which identification was not possible (N_{noID}). The table contains the number of hadrons (top of row) and the corresponding percentage (bottom of row).

Since the data sample is dominated by π, we expect the results for π to be close to the results for general hadrons without identification. To obtain the results, the measured number of hadrons in ϕ_{h} and P_{T}^2-distributions is corrected for efficiency and mis-identification by weighing each event with elements of the pseudo-inverse[1] of the efficiency-purity matrix:

$$\underbrace{\begin{pmatrix} \epsilon(\pi \to \pi) & \epsilon(\text{K} \to \pi) \\ \epsilon(\pi \to \text{K}) & \epsilon(\text{K} \to \text{K}) \\ \epsilon(\pi \to \text{no ID}) & \epsilon(\text{K} \to \text{no ID}) \end{pmatrix}^{+}}_{M^{+}_{\text{RICH}}} \begin{pmatrix} N_{\pi} \\ N_{\text{K}} \\ N_{\text{noID}} \end{pmatrix} = \begin{pmatrix} N_{\pi,\text{true}} \\ N_{\text{K},\text{true}} \end{pmatrix}. \tag{4.1}$$

Counts before the correction are not indexed, corrected counts are denoted by the index *true*. The elements of the efficiency-purity matrix were evaluated in chapter 3.

4.2 Binning and kinematic range

The binning for this analysis was chosen according to previous releases and published papers. Limits for kinematic variables for 1D and 3D analysis of the azimuthal asymmetries as well as for studies of Q^2 dependence and 4D P_{T}^2-distributions are given in tables 4.5–4.8. The studies of azimuthal asymmetries are performed in various binnings to capture the multi-dimensional dependence of the azimuthal asymmetries (or structure functions). For identified hadrons, the analysis is performed only in 1D binning due to the lack of statistics (only 3 out of 6 periods are used for the analysis of identified hadrons).

The kinematic range previously set by DIS cuts described in section 4.1 was narrowed down to match previous releases and papers with the following set of additional conditions:

[1]The term pseudo-inverse refers to the Moore–Penrose inverse, which is denoted by the symbol + in superscript. For calculation we use function `linalg.pinv` from NumPy library for Python [33].

bin no.		1		2		3		4→
x	0.003	–	0.008	–	0.013	–	0.020	–
z	0.10	–	0.12	–	0.15	–	0.20	–
$P_{\mathrm{T}}/(\mathrm{GeV}/c)$	0.10	–	0.20	–	0.27	–	0.33	–
bin no.	→	5		6		7		8→
x	0.032	–	0.050	–	0.080	–	0.130	
z	0.25	–	0.30	–	0.34	–	0.38	–
$P_{\mathrm{T}}/(\mathrm{GeV}/c)$	0.39	–	0.46	–	0.55	–	0.64	–
bin no.	→		9		10		11	
z	0.42	–	0.49	–	0.63	–	0.85	
$P_{\mathrm{T}}/(\mathrm{GeV}/c)$	0.77	–	1.00	–	1.73			

Table 4.5: Binning limits for 1D azimuthal asymmetries analysis.

bin no.		1		2		3		4 →
x	0.008	–	0.013	–	0.020	–	0.032	–
$Q^2/(\mathrm{GeV}/c)^2$	1.0	–	1.7	–	3.0	–	7.0	–
bin no.	→	5		6				
x	0.050	–	0.080	–	0.130			
$Q^2/(\mathrm{GeV}/c)^2$	16							

Table 4.6: Binning limits for Q^2 dependence studies for asymmetries analysis (2D $x : Q^2$ binning).

bin no.		1		2		3		4→
x	0.003	–	0.012	–	0.020	–	0.038	–
z	0.10	–	0.20	–	0.25	–	0.32	–
P_{T} (GeV/c)	0.10	–	0.30	–	0.50	–	0.64	–
bin no.	→	5		6		7		
x	0.130							
z	0.40	–	0.55	–	0.70	–	0.85	
P_{T} (GeV/c)	1.00	–	1.73					

Table 4.7: Binning limits for 3D azimuthal asymmetries analysis.

bin no.		1		2		3		4→
x	0.003	–	0.013	–	0.020	–	0.055	–
$Q^2/(\mathrm{GeV}/c)^2$	1	–	3	–	16			
z	0.2	–	0.3	–	0.4	–	0.6	–
$P_{\mathrm{T}}^2/(\mathrm{GeV}/c)^2$	0.02	–	0.06	–	0.1	–	0.14	–
bin no.		5		6		7		8→
x	0.100							
z	0.8							
$P_{\mathrm{T}}^2/(\mathrm{GeV}/c)^2$	0.196	–	0.27	–	0.35	–	0.46	–
bin no.		9		10		11		12→
$P_{\mathrm{T}}^2/(\mathrm{GeV}/c)^2$	0.6	–	0.76	–	1	–	1.24	–
bin no.		13		14		15		
$P_{\mathrm{T}}^2/(\mathrm{GeV}/c)^2$	1.52	–	1.85	–	2.35	–	3	

Table 4.8: Binning limits for measurement of P_{T}^2-distributions.

1. For analysis in 1D binning:

$$\begin{aligned}
0.2 < y < 0.9 \\
0.2 < z < 0.85 \text{ for } P_{\mathrm{T}} \text{ and } x \text{ binning} \\
0.1 < z < 0.85 \text{ for } z \text{ binning} \\
0.1 \text{ GeV}/c < P_{\mathrm{T}} < 1.73 \text{ GeV}/c \text{ for } P_{\mathrm{T}} \text{ binning} \\
0.1 \text{ GeV}/c < P_{\mathrm{T}} < 1.00 \text{ GeV}/c \text{ for } z \text{ and } x \text{ binning} \\
-251 \text{ cm} < Z_{\mathrm{vertex}} < -71 \text{ cm}
\end{aligned} \tag{4.2}$$

2. For analysis in Q^2 dependence (2D $x : Q^2$ binning) and 4D P_{T}^2 binning:

$$\begin{aligned}
0.2 < y < 0.9 \\
0.2 < z < 0.85 \\
0.1 \text{ GeV}/c < P_{\mathrm{T}} < 1.00 \text{ GeV}/c \\
-251 \text{ cm} < Z_{\mathrm{vertex}} < -71 \text{ cm}
\end{aligned} \tag{4.3}$$

3. For analysis in 3D binning:

$$\begin{aligned}
0.2 < y < 0.9 \\
0.1 < z < 0.85 \\
0.1 \text{ GeV}/c < P_{\mathrm{T}} < 1.73 \text{ GeV}/c \\
-251 \text{ cm} < Z_{\mathrm{vertex}} < -71 \text{ cm}
\end{aligned} \tag{4.4}$$

4.3 Fitting procedure

4.3.1 Azimuthal asymmetries

The ϕ_{h} dependent cross-section of the SIDIS process is given in the equation 1.9. The procedure of extracting the azimuthal asymmetries means fitting the following form of a cross-section on the measured and corrected distributions of ϕ_{h} in the form of a histogram with 16 bins from $-\pi$ to π:

$$\sigma(\phi_{\mathrm{h}}) = \sigma_0(1 + p_1 \cos\phi_{\mathrm{h}} + p_2 \cos 2\phi_{\mathrm{h}} + p_3 \sin\phi_{\mathrm{h}}) \ . \tag{4.5}$$

The relation between the coefficients of the fit $p_i \pm \sigma_{p_i},\ i \in \{1, 2, 3\}$ and the azimuthal asymmetries is then:

$$A_{\mathrm{UU}}^{\cos\phi_{\mathrm{h}}} = \frac{p_1}{\langle\varepsilon_1\rangle} \ , \ A_{\mathrm{UU}}^{\cos 2\phi_{\mathrm{h}}} = \frac{p_2}{\langle\varepsilon_2\rangle} \ , \ A_{\mathrm{LU}}^{\sin\phi_{\mathrm{h}}} = \frac{p_3}{\langle\lambda\rangle\langle\varepsilon_3\rangle} \ , \tag{4.6}$$

where the mean values are evaluated in each kinematic bin. Statistical errors of asymmetries derived from the errors of the fitted coefficient are given as:

$$\sigma_{A_{\mathrm{UU}}^{\cos\phi_{\mathrm{h}}}} = \frac{\sigma_{p_1}}{\langle\varepsilon_1\rangle} \ , \ \sigma_{A_{\mathrm{UU}}^{\cos 2\phi_{\mathrm{h}}}} = \frac{\sigma_{p_2}}{\langle\varepsilon_2\rangle} \ , \ \sigma_{A_{\mathrm{LU}}^{\sin\phi_{\mathrm{h}}}} = \frac{\sigma_{p_3}}{\langle\lambda\rangle\langle\varepsilon_3\rangle} \ . \tag{4.7}$$

To visualise kinematic dependences, the mean values of the variables $\langle x\rangle$, $\langle P_T\rangle$, and $\langle z\rangle$ were used in the graphs as the coordinates on the abscissa. To avoid double-counting we use the measured kinematic mean values and kinematic factors without any corrections as the *smearing* (shifting of events between kinematical bins) is already accounted for in the correction of counts in the $x : \phi_{\mathrm{h}}$ bins, $z : Q^2 : x : P_{\mathrm{T}}^2$ bins or other variants of the binnings.

4.3.2 P_{T}^2-distributions

An integrated cross-section describing P_{T}^2-distributions is given in equation 1.17. This cross-section can be fitted on the distributions of P_{T}^2, normalised to the size of the first bin (binning described in table 4.8). It was empirically shown that in the whole range of P_{T}^2 the measured cross-section can be described by a double exponential,

$$\sigma(P_{\mathrm{T}}^2) = \sum_{i=1}^{2} A_i \exp\left(-\frac{P_{\mathrm{T}}^2}{a_i}\right) . \tag{4.8}$$

with a final value of $\langle P_{\mathrm{T}}^2 \rangle$ being a statistically-weighted average over the two slopes of the exponentials:

$$\langle P_{\mathrm{T}}^2 \rangle = \frac{A_1 a_1^2 + A_2 a_2^2}{A_1 a_1 + A_2 a_2} . \tag{4.9}$$

4.3.3 Final results

Both the azimuthal asymmetries and the P_{T}^2-distributions are evaluated for multiple data-taking periods and corrected for various effects, as described in the following sections. It has been proven that fitting the merged histograms of ϕ_{h} or P_{T}^2, rather than performing the fit separately for each period, as was done in [30], yields a better-quality fit of the cross sections (4.5) and (4.8). The final result is obtained as a statistically weighted average over the two beam charges. Distributions measured with μ^+ and μ^- beams cannot be merged, as the sensitivity to the beam-polarisation dependent $A_{\mathrm{LU}}^{\sin\phi_{\mathrm{h}}}$ would be lost.

4.4 Background treatment

The event selection explained in the previous section 4.1 does not account for the production of diffractive vector mesons (DVMs),

$$\ell(l) + \mathrm{N}(P) \to \ell(l') + \mathrm{N}(P') + \mathrm{V}(P_{\mathrm{V}}), \tag{4.10}$$

where V represents the vector meson and ℓ and ℓ' denote the initial and final leptons with their 4-momenta in affiliated parentheses. If the short-lived diffractive vector mesons (DVMs) decays to charged hadrons in the SIDIS kinematical region, the decay products contaminate the SIDIS sample. Since they come from a completely different (elastic) process with a different cross-section, we have to remove them from the sample if we want to describe it by the SIDIS TMDs formalism explained in section 1.3.

DVM inherits the polarisation of γ^*, thus the decay hadrons are produced with large azimuthal modulations, which makes the treatment of their presence in the SIDIS sample necessary for the analysis of azimuthal asymmetries. For example, the amplitudes of azimuthal modulations in the ϕ_{h} distributions of the decay products of exclusive ρ^0 (obtained by fitting standard SIDIS cross-section from formula 1.9) reach values up to ≈ 0.7 as illustrated in figure 4.2. For comparison, the size of the measured effect for SIDIS hadrons is one order of magnitude lower, as will be presented in section 5 with the final results. The effect

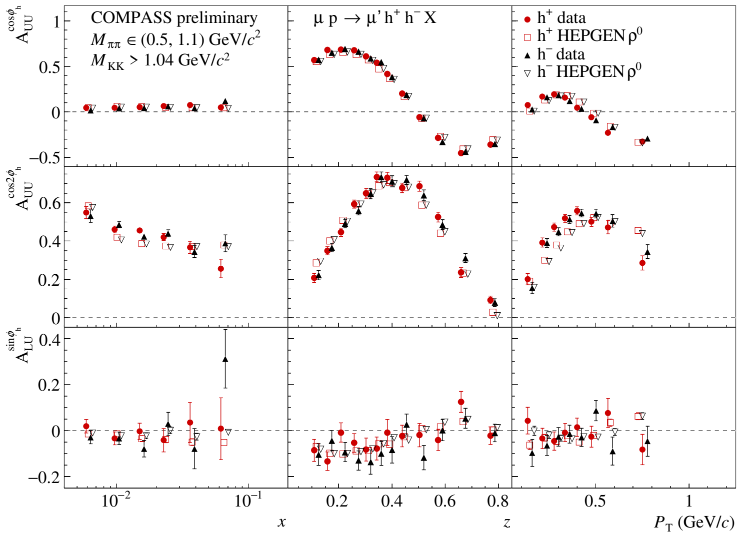

Figure 4.2: The amplitudes of azimuthal modulations in ϕ_h distributions of visible ρ^0 decay products (obtained by fitting standard SIDIS cross-section from formula 1.9). Measured data compared with HEPGEN ρ^0 MC.

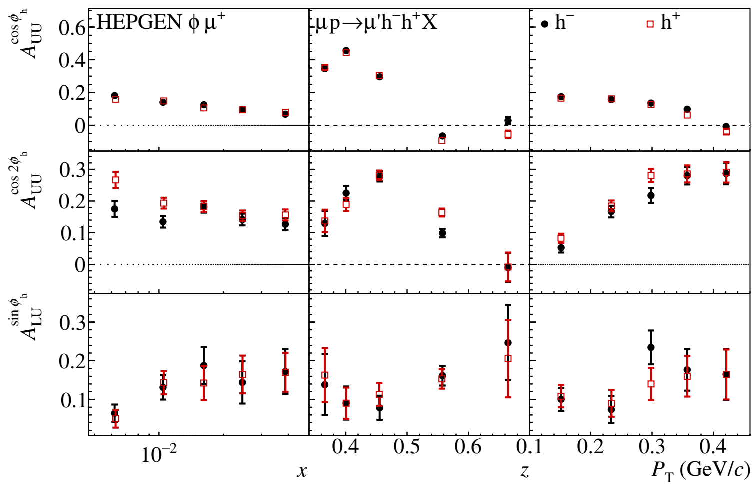

Figure 4.3: The amplitudes of azimuthal modulations in ϕ_h distributions of HEPGEN ϕ^0 μ^+ MC (obtained by fitting standard SIDIS cross-section from formula 1.9).

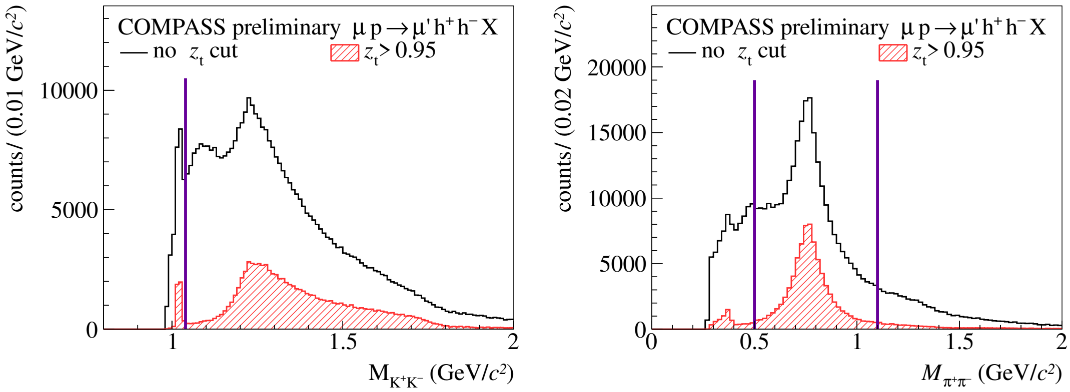

Figure 4.4: Invariant mass for $\phi^0(1020) \to K^+K^-$ (left) and $\rho^0(770) \to \pi^+\pi^-$ (right) decay hypotheses. Figures compare distributions before (white) and after (red) cut on z_t. Purple lines represent limits for the peak selection from 4.14.

of the background treatment is expected to be less significant for P_T^2-distributions because they are affected only by the number of hadrons.

The theory predicts a significant number of diffractive vector mesons (DVMs) produced in process 4.10 that have a reasonable branching ratio BR to charged hadrons only for the following three vector mesons [28]:

$$\begin{aligned} \rho^0(770) &\to \pi^+\pi^- & BR &= 100\% \,, \\ \omega(782) &\to \pi^+\pi^-\pi^0 & BR &= (89.2 \pm 0.7)\% \,, \\ \phi^0(1020) &\to K^+K^- & BR &= (49.1 \pm 0.5)\% \,. \end{aligned} \tag{4.11}$$

Studies with a MC simulation showed that the contribution of $\omega(782)$ can be neglected at COMPASS [34].

In the process of treatment of HEMP as a background process, we distinguish two cases, which are treated differently, as explained in the following subsections:

1. both of the products of 4.11 are reconstructed in the spectrometer (case of *visible decays*),

2. only one hadron is reconstructed in the spectrometer (case of *invisible decays*).

The treatment of contributions from each of these cases is different, as explained in the following subsections.

4.4.1 Visible decays of DVMs

First, in the case of reconstructing both charged hadrons in the spectrometer, one can select *candidates for the exclusive processes* as events with only 3 particles detected in the spectrometer: muon and 2 oppositely charged hadrons that both pass hadron selection from 4.1. The presence of the hadrons from decays of ρ^0 and ϕ can be proven by plotting the invariant masses of their decay products (see 4.11) as shown in figure 4.4.

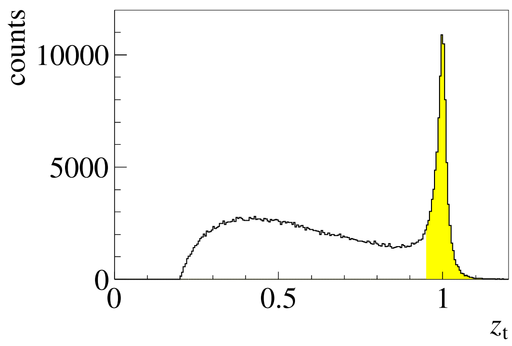

Figure 4.5: Distribution of z_t of the hadron pairs from candidates for exclusive processes. [34]

When the event is exclusive, the two hadrons share all the energy from the interaction. This constraint can be quantified using the total fractional energy of hadrons from exclusive candidates (z defined in 1.8):

$$z_\mathrm{t} \equiv z_{\mathrm{h}^+} + z_{\mathrm{h}^-} \ . \tag{4.12}$$

From the previous consideration, we expect $z_\mathrm{t} = 1$ for the exclusive process. The peak in the z_t distribution of candidates in exclusive events is clearly visible in figure 4.5. To cut the exclusive peak, and thus eliminate visible contamination, we demand the following:

$$z_\mathrm{t} < 0.95 \ . \tag{4.13}$$

4.4.2 Invisible decays of DVMs

In the case of reconstructing only one charged hadron in the spectrometer, it is indistinguishable if the hadron comes from an exclusive or inclusive process. Thus, we have to use MC simulations to subtract the background directly from the ϕ_h distributions. At COMPASS, HEPGEN MC generator is used to simulate HEMP processes for each relevant vector meson separately. HEPGEN generator nicely describes the amplitudes of azimuthal modulations of the visible hadrons from DVM decays (see figure 4.2) thanks to the parametrisation of the diffractive cross-section measured by COMPASS by the spin density matrix elements (SDMEs), which HEPGEN uses when generating the events [35].

The amount of hadrons from *invisible* DVM decays to subtract is estimated using the exclusive events from the *visible* case. To do that, first, we have to separate the events of ρ^0 and ϕ^0 decays by selecting their corresponding peaks in invariant mass distributions in measured data. The limits for peak selection (purple lines in figure 4.4) are numerically:

$$\begin{aligned} \rho \to \pi^+\pi^- :\ & M_{\mathrm{K}^+\mathrm{K}^-} \in [1.04, \infty]\ \mathrm{GeV}/c^2 \\ & \text{and } M_{\pi^+\pi^-} \in [0.5, 1.1]\ \mathrm{GeV}/c^2 \ , \\ \phi \to \mathrm{K}^+\mathrm{K}^- :\ & M_{\mathrm{K}^+\mathrm{K}^-} \in [0, 1.04]\ \mathrm{GeV}/c^2 \ . \end{aligned} \tag{4.14}$$

For each of the decay hypotheses defined with the limits in equation 4.14, we plot the missing energy distributions:

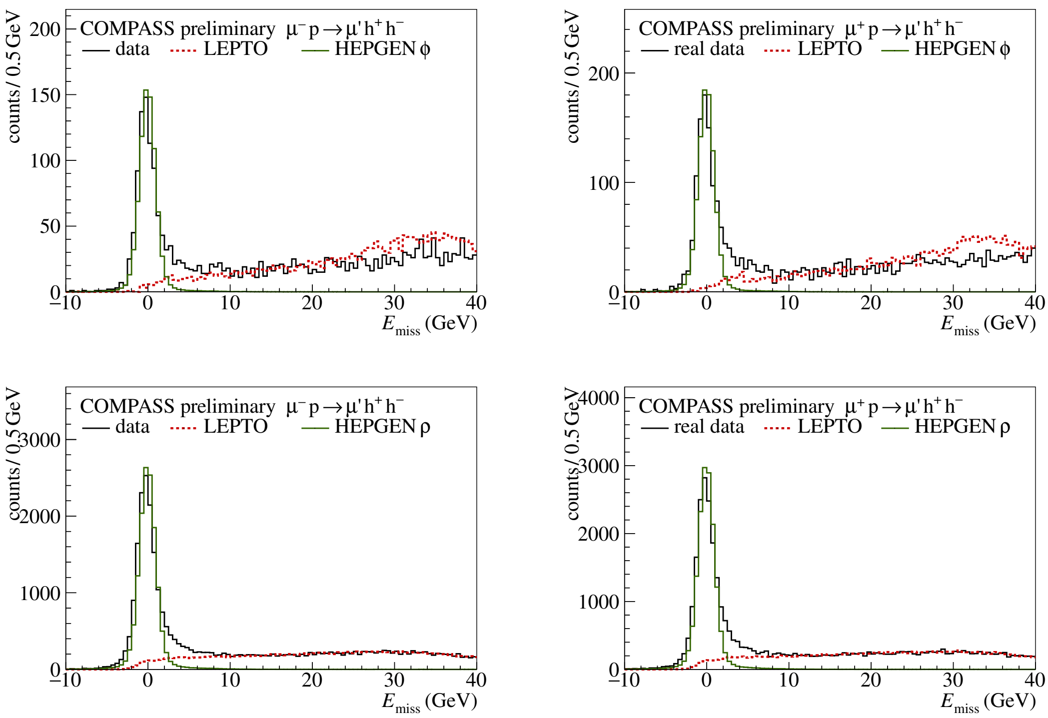

Figure 4.6: Missing energy distributions of the candidates for exclusive events in measured data (black line), LEPTO MC (red line) and HEPGEN MC (green line). Plots for ϕ^0 are on top, for ρ^0 on the bottom. Plots for μ^- are on left, μ^+ on right.

$$E_{\mathrm{miss}} = \frac{M_{\mathrm{X}}^2 - M_{\mathrm{p}}^2}{2M_{\mathrm{p}}} , \qquad M_{\mathrm{X}}^2 = (p + q - P_{\mathrm{h}^+} - P_{\mathrm{h}^-})^2 . \tag{4.15}$$

Since exclusive events carry all of the energy of the interaction, their missing energy should have a value around 0. The missing energy histograms are plotted in figure 4.6 with the *exclusive peak* visible around 0. The goal is to fully describe the missing energy distribution of the measured data by re-scaled HEPGEN (reproducing the peak around 0) and LEPTO MC (reproducing the inclusive tail). The number that we scale HEPGEN with (*normalization factor* $n_\rho^\pm$, $n_\phi^\pm$)[2] tells us how many invisible hadrons are there to subtract from the ϕ_{h} distributions. Table 4.9 shows its values integrated over all the periods analysed, for clarity, while in the actual analysis, the normalisation factors are determined, and the subtraction is performed period by period

	μ^-	μ^+
$n_\rho^\pm$	0.170 ± 0.002	0.198 ± 0.002
$n_\phi^\pm$	0.060 ± 0.003	0.074 ± 0.003

Table 4.9: Values of the normalization factor calculated with respect to the data from all analyzed periods.

[2] $\pm$ represents beam charge

4.4.3 The effect of background treatment

The effect of background treatment on UAs and P_{T}^2-distributions without identification

Background treatment is a hot topic within the experiments measuring azimuthal asymmetries. To verify the procedure of removal of hadrons that are products of DVMs, it is interesting to check the effect of each correction step. In fact, there is a big difference in the effect of each step of the background treatment, which is demonstrated in figures 4.7–4.13. The majority of the background is removed by the *DVM cut* (see 4.4). The correction done by subtracting HEPGEN MC is only small, which is the strong point of the measurement – relying too much on MC corrections would increase the systematic uncertainty of the results. The largest effect is observed at high z and low x, which are also the kinematic regions with a significant contamination by the decay products of diffractive vector mesons (DVMs). The effect of the background treatment on the P_{T}^2-distributions is small [36].

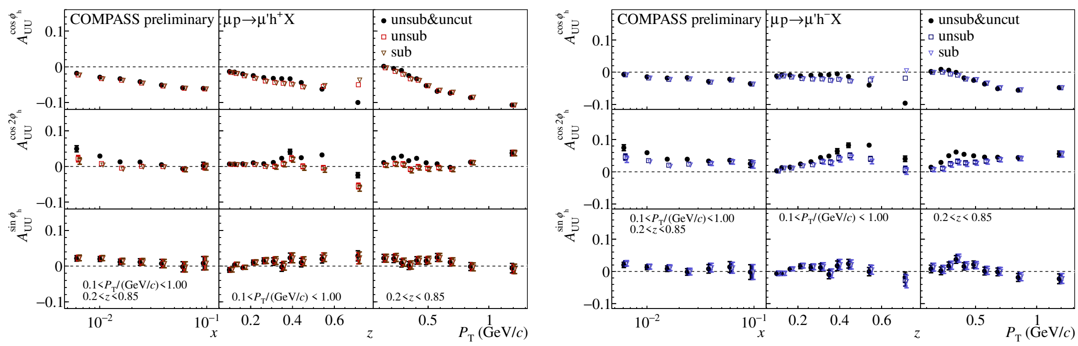

Figure 4.7: The comparison of the $A_{\mathrm{XU}}^{f(\phi_{\mathrm{h}})}$ before applying DVM cut (unsub & no cut), after applying the cut (unsub) and after DVM subtraction (sub) for (left) h^+ and (right) h^-.

The effect of background treatment on UAs of identified hadrons

The step-by-step effect of background treatment is shown in figure 4.14 for π and in figure 4.15 for K. The effect on π closely resembles the effect observed in the analysis without the hadron identification presented in the figure 4.7, as expected due to π dominance within the data sample. The impact for K is not as significant, which is a result of multiple factors: much more restricted kinematic range and smaller azimuthal modulations in the cross section for the exclusive ϕ^0 (as illustrated in figure 4.2), lower contamination from exclusive ϕ^0 decays, and the fact that the asymmetries of K are much larger.

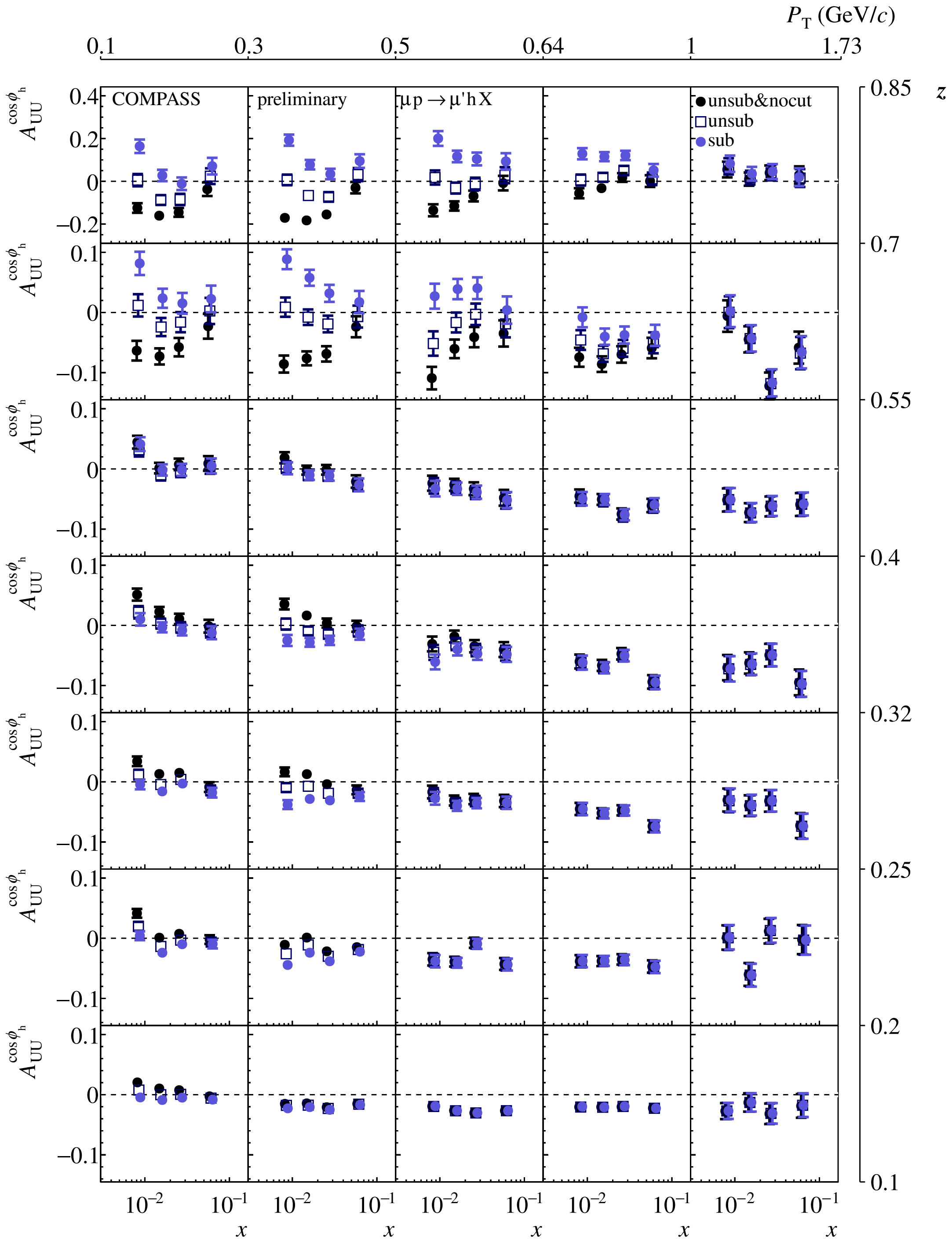

Figure 4.8: The comparison of $A_{\mathrm{UU}}^{\cos\phi_{\mathrm{h}}}$ before applying DVM cut (unsub & no cut), after applying the cut (unsub) and after DVM subtraction (sub) for h^{-}.

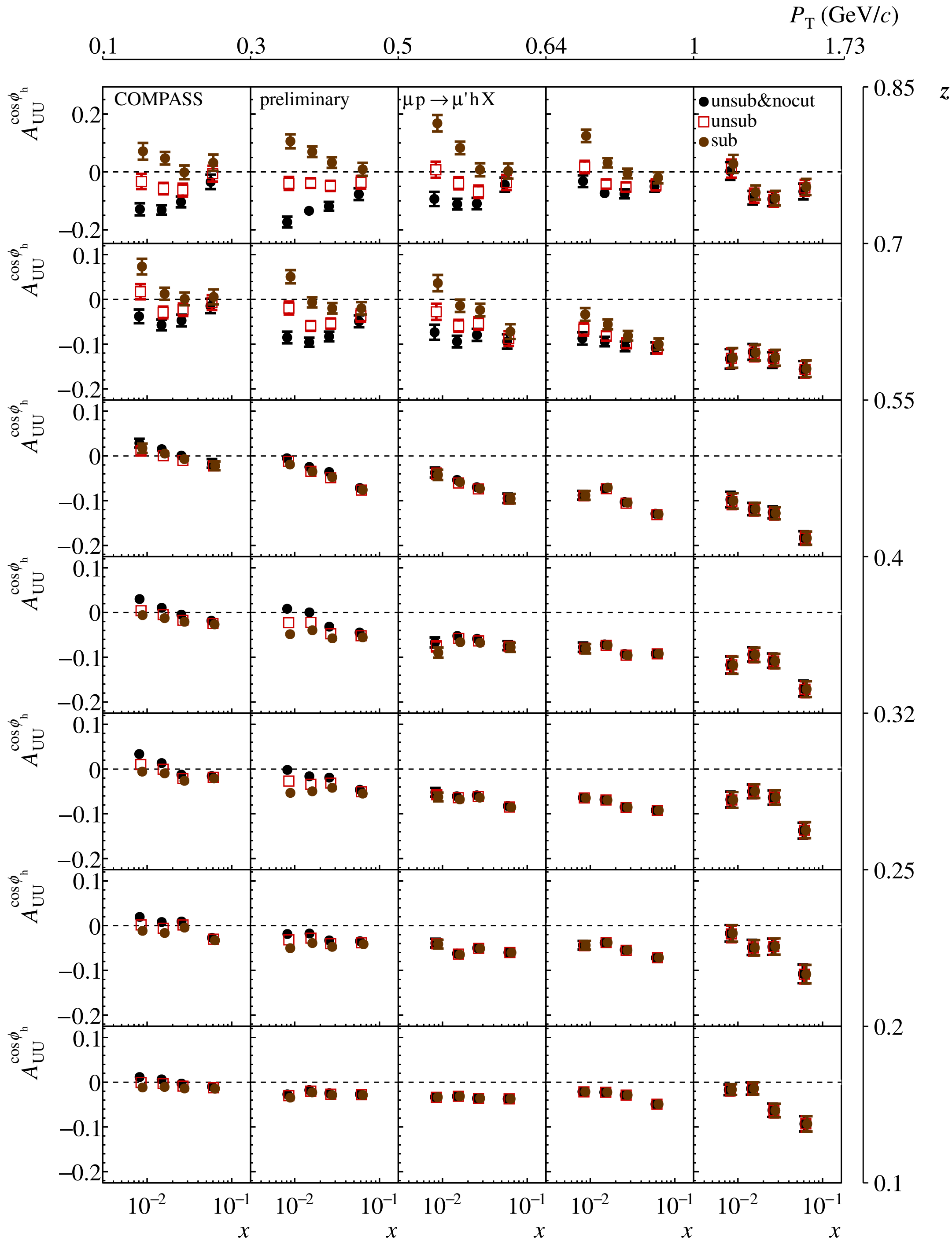

Figure 4.9: The comparison of $A_{\mathrm{UU}}^{\cos\phi_{\mathrm{h}}}$ before applying DVM cut (unsub & no cut), after applying the cut (unsub) and after DVM subtraction (sub) for h^{+}.

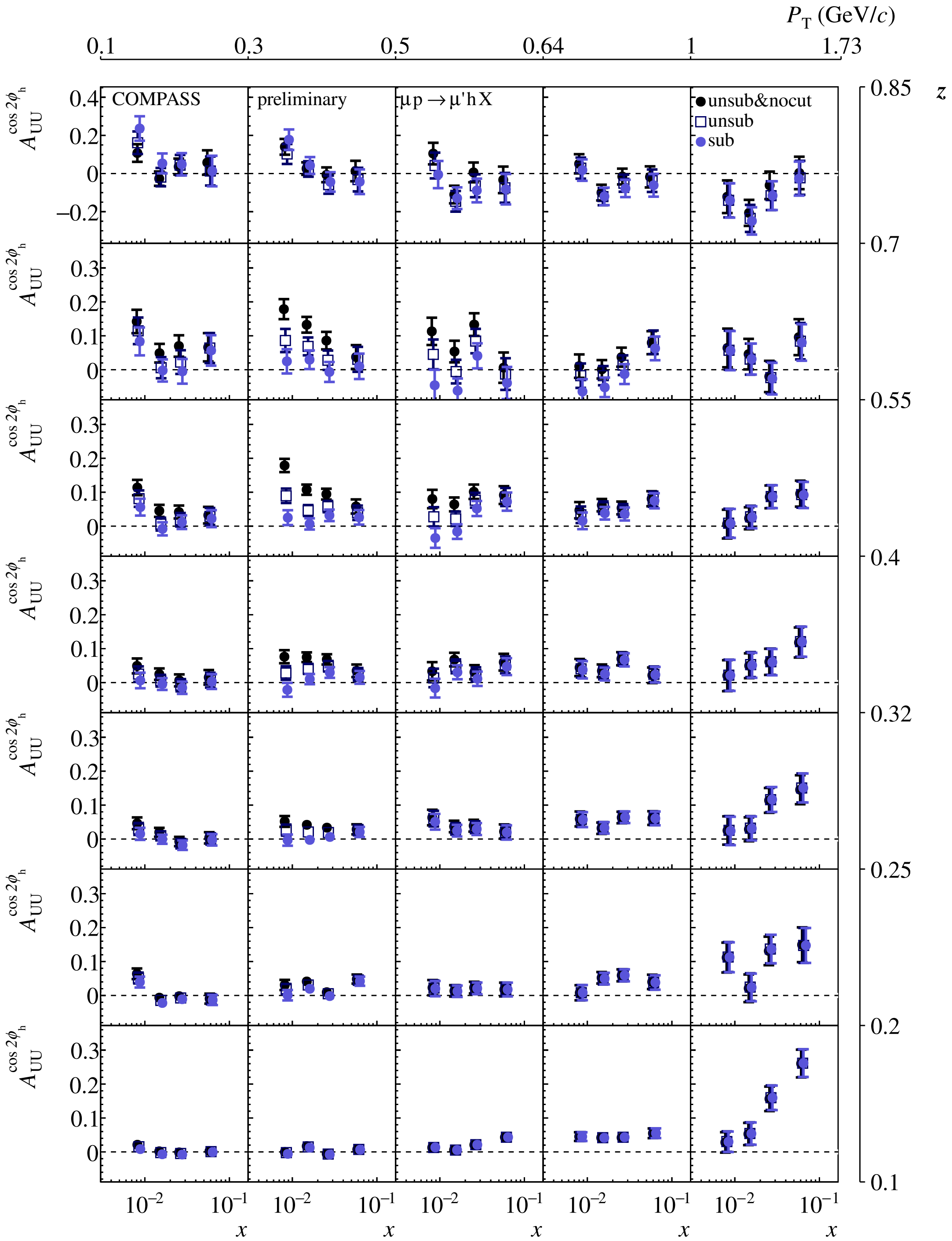

Figure 4.10: The comparison of $A_{\mathrm{UU}}^{\cos 2\phi_{\mathrm{h}}}$ before applying DVM cut (unsub & no cut), after applying the cut (unsub) and after DVM subtraction (sub) for h$^-$.

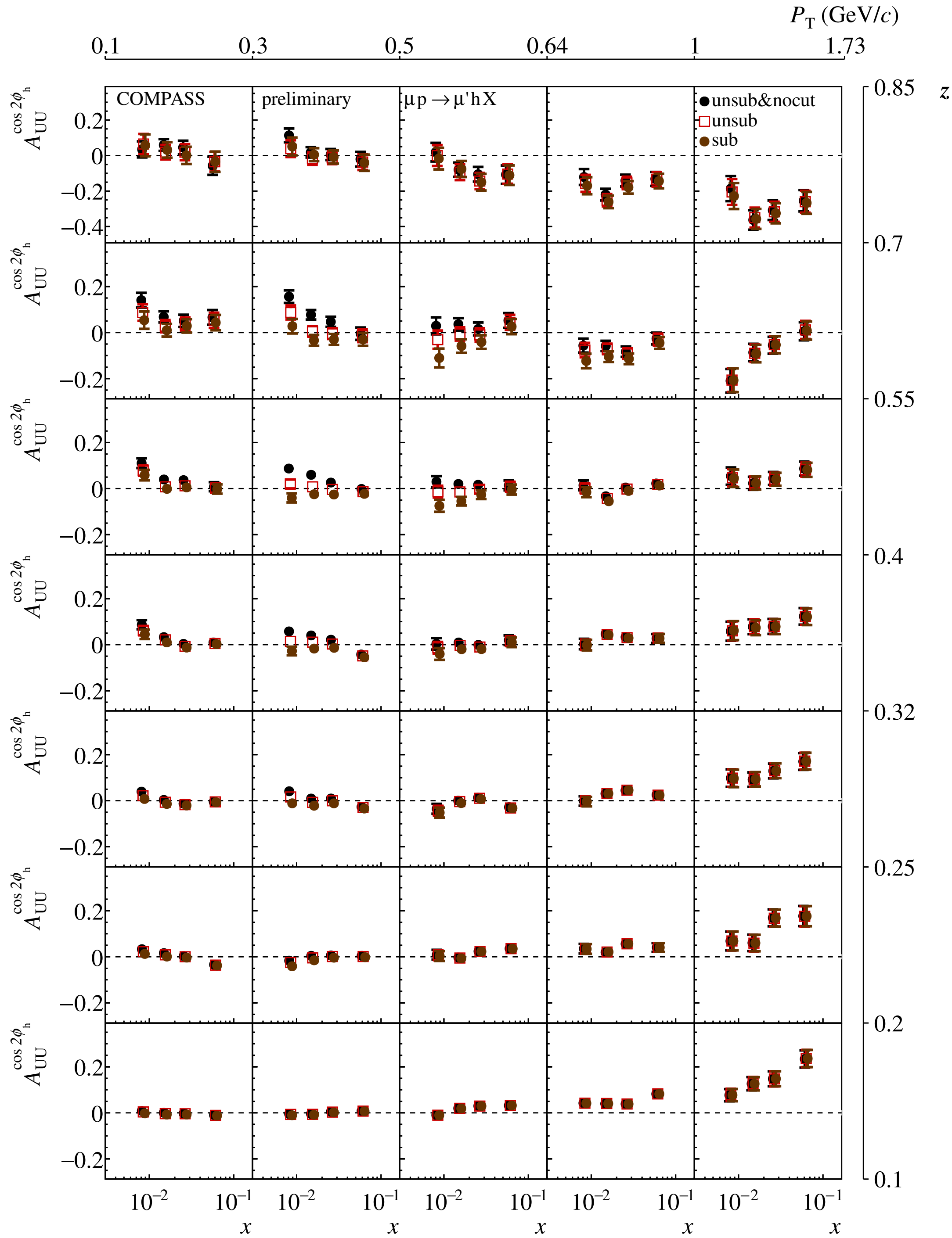

Figure 4.11: The comparison of $A_{\mathrm{UU}}^{\cos 2\phi_{\mathrm{h}}}$ before applying DVM cut (unsub & no cut), after applying the cut (unsub) and after DVM subtraction (sub) for h^{+}.

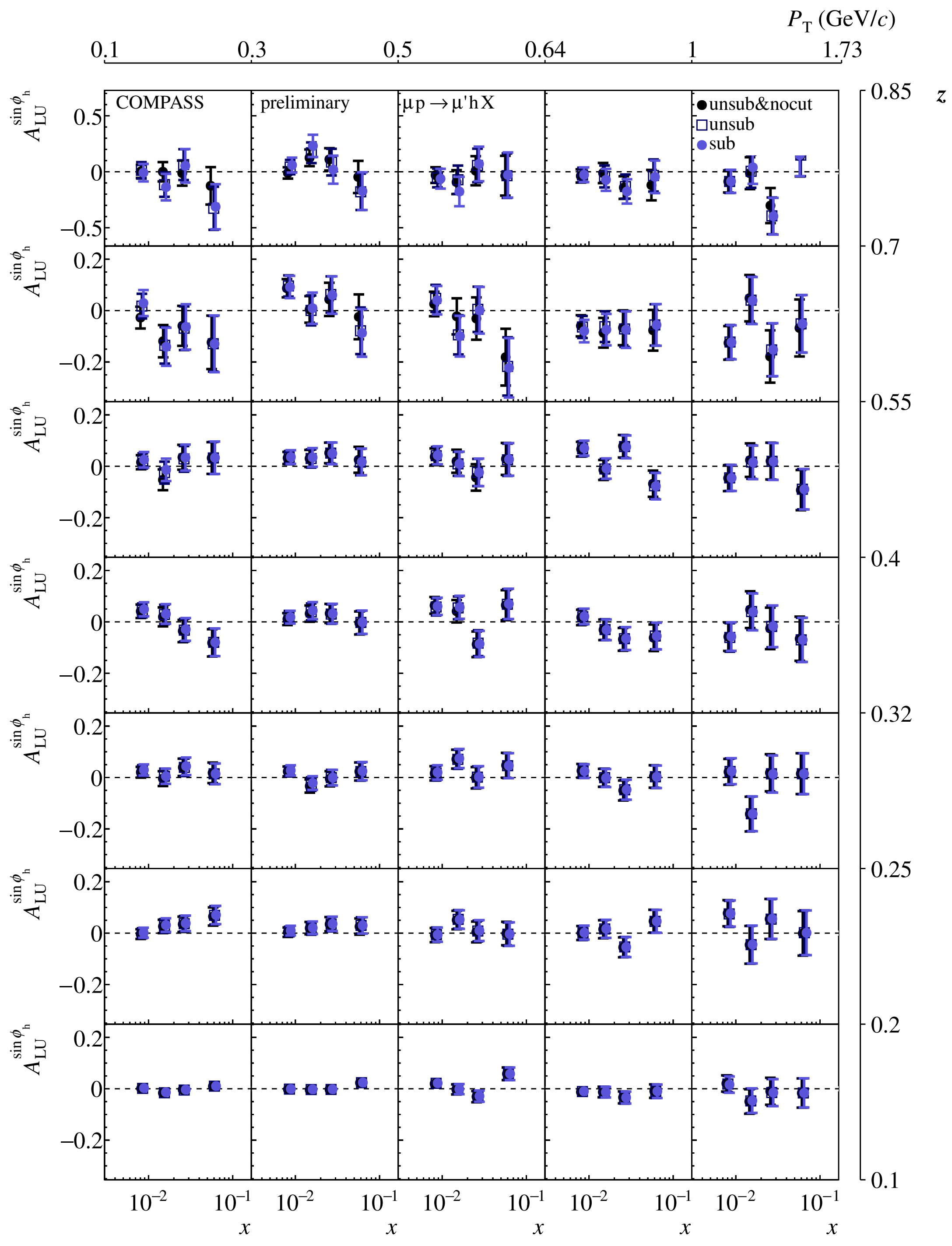

Figure 4.12: The comparison of $A_{\mathrm{LU}}^{\sin\phi_{\mathrm{h}}}$ before applying DVM cut (unsub & no cut), after applying the cut (unsub) and after DVM subtraction (sub) for h^-.

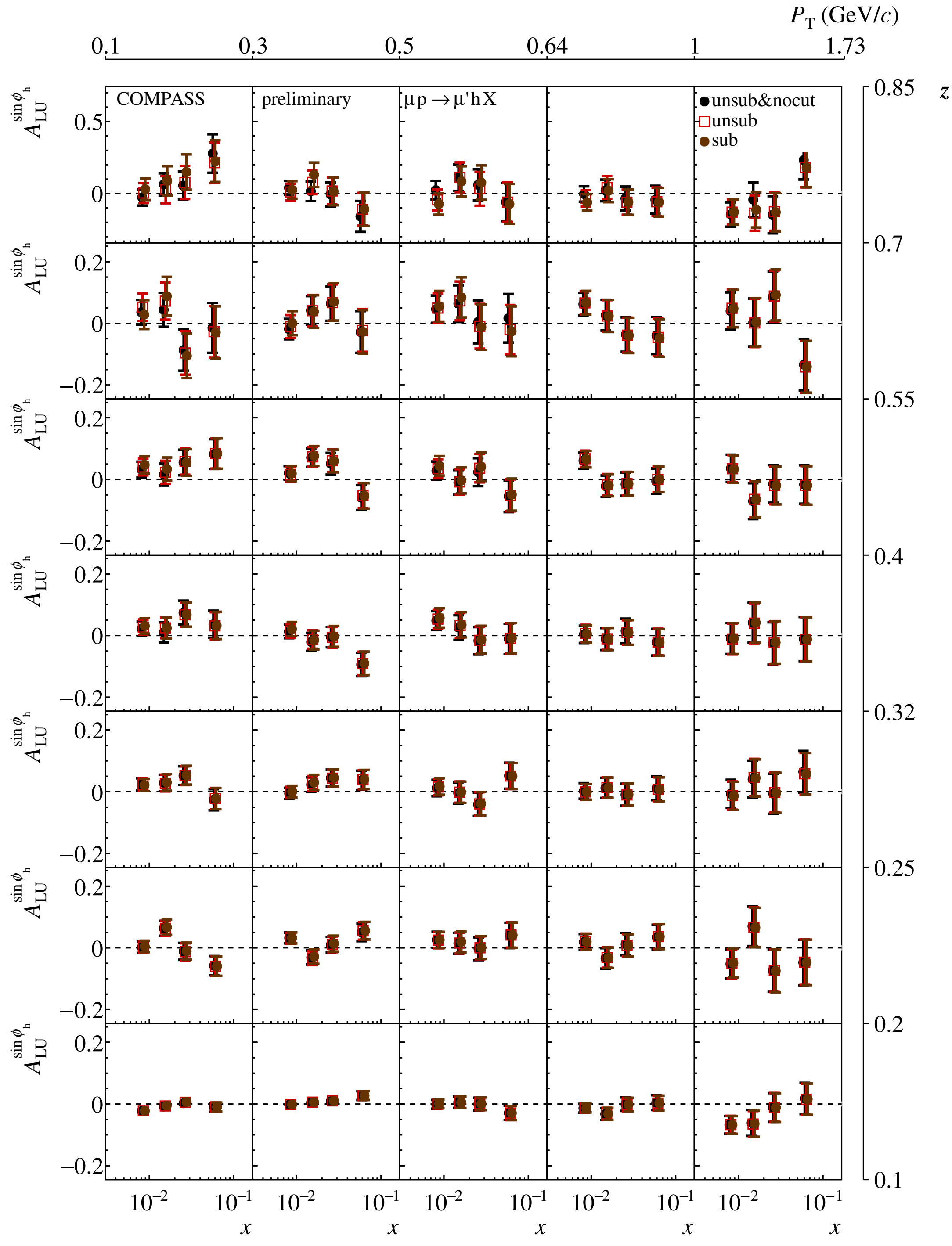

Figure 4.13: The comparison of $A_{LU}^{\sin\phi_h}$ before applying DVM cut (unsub & no cut), after applying the cut (unsub) and after DVM subtraction (sub) for h^+.

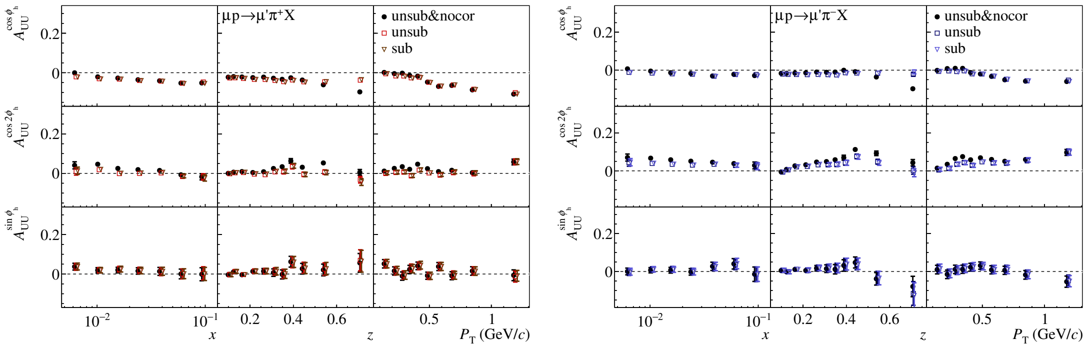

Figure 4.14: The comparison of the $A_{\mathrm{XU}}^{f(\phi_\mathrm{h})}$ before applying DVM cut (unsub&no cut), after applying the cut (unsub) and after DVM subtraction (sub) for (left) π^+ and (right) π^-.

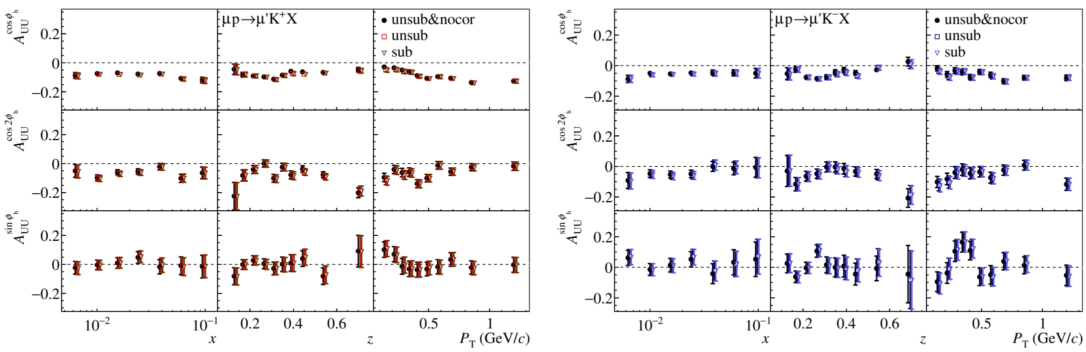

Figure 4.15: The comparison of the $A_{\mathrm{XU}}^{f(\phi_\mathrm{h})}$ before applying DVM cut (unsub&no cut), after applying the cut (unsub) and after DVM subtraction (sub) for (left) K^+ and (right) K^-.

4.5 Acceptance correction

Due to the finite dimensions and efficiency of the spectrometer, a fraction of the products of scattering remains undetected. The ratio of detected to produced particles, known as the *acceptance* and denoted by a, varies with the kinematics, particularly the azimuthal angle, which results in non-physical azimuthal modulations in the ϕ_h distributions. Acceptance correction removes these non-physical modulations using MC.

At COMPASS the so-called MC chain for determining SIDIS acceptance consists of the LEPTO event generator, TGeant – package based on Geant 4 for modelling the interaction of produced particles with the experimental setup, and CORAL – software for the event reconstruction [37, 38].

Removing false asymmetries requires correcting the observed distributions for acceptance effects. This is done by evaluating the acceptance a, defined as the ratio of reconstructed N_rec to generated N_gen events in the MC simulation::

$$a = \frac{N_\mathrm{rec}}{N_\mathrm{gen}} \,. \tag{4.16}$$

Each bin of the measured ϕ_h distribution or P_T^2-distribution is then corrected by dividing by the corresponding acceptance value. Since $N_\mathrm{rec} \ll N_\mathrm{gen}$, the acceptance error is given only by the error of reconstructed MC, which follows a Poisson distribution with variance $\sigma^2_{N_\mathrm{rec}} = N_\mathrm{rec}$:

$$\sigma_a = \frac{\sqrt{N_\mathrm{rec}}}{N_\mathrm{gen}} \,. \tag{4.17}$$

The kinematic range of the analysis is selected such that the acceptance correction remains reasonably small compared to the size of the measured effect. In most of the phase space, the acceptance averaged over ϕ_h is between 0.4 and 0.6, going down to 0.3 only in the corner of low z and high P_T. The amplitudes of the azimuthal modulations of the acceptance are mostly below 0.02, with notable exceptions in certain 3D bins, where the $\cos\phi$ and $\cos 2\phi$ can reach up to 0.2. The size of the acceptance correction is different for each beam charge – hadron charge combination due to the different setup of magnets, and has to be studied carefully to validate the final results [36].

4.6 Radiative correction

The TMD framework of the tree-level cross section in equation 1.9 does not account for QED radiative effects such as the processes highlighted in colour in figure 4.16. Contributions from higher-order diagrams affect leptonic DIS variables as well as the hadronic variables due to the change of virtual photon direction [39].

In the past, the program TERAD (based on the scheme described in ref. [40]) was used to correct COMPASS results on multiplicities of charged hadrons [41, 42] for radiative effects. This approach is strictly valid only for inclusive DIS events and there is no dependence on hadronic variables. Thus, a new approach had to be adopted to better describe the multiplicities in their z dependence and to correct azimuthal asymmetries.

While the correction for leptonic variables can be calculated analytically, the effect on the hadronic variables, which are the result of stochastic processes of parton showers and hadronisation, has to be accessed by MC simulations. At COMPASS, DJANGOH MC generator has been adopted for this use [43].

We correct the number of events in each ϕ_h or P_T^2 bin by the ratio η of hadrons simulated in that bin by DJANGOH with radiative effects on $N_h^{\text{RE-on}}$ and off $N_h^{\text{RE-off}}$ (normalised to the MC luminosity in form of number of DIS events $N_{\text{DIS}}^{\text{RE-off}}$ and $N_{\text{DIS}}^{\text{RE-on}}$, respectively):

$$\eta = \frac{N_h^{\text{RE-off}}}{N_h^{\text{RE-on}}} \frac{N_{\text{DIS}}^{\text{RE-on}}}{N_{\text{DIS}}^{\text{RE-off}}} . \tag{4.18}$$

For the hadron counts in P_T^2-distributions, the shift towards lower P_T is expected due to the loss of energy with the radiation. RC should have no effect on the $A_{LU}^{\sin\phi_h}$. Such an effect would be the result of a helicity or beam-charge dependence of the RE, which is not the case according to the current theory of QED in the standard model.

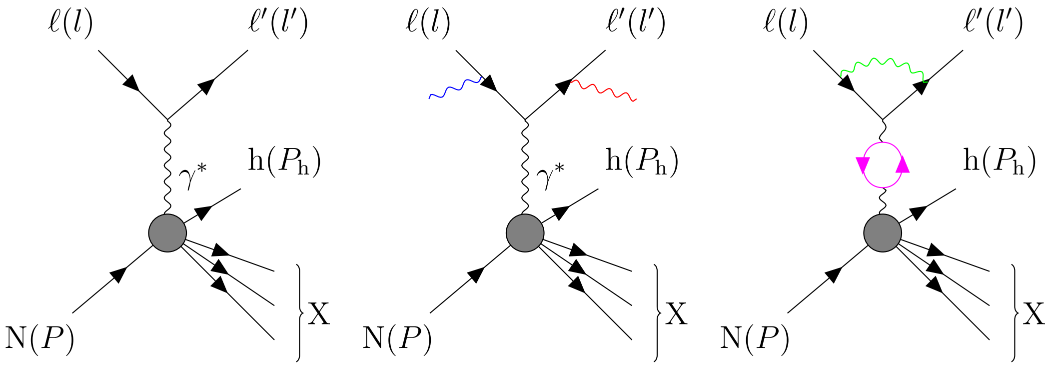

Figure 4.16: (left) Feynman diagram of SIDIS process at tree level (middle, right). Examples of higher order diagrams – illustration of QED radiative effects: initial state radiation (blue), final state radiation (red), vertex correction (green) and virtual photon self energy (magenta).

4.6.1 The effect of RC

The effect of RC on UAs without identification

Being the new addition to the family of corrections, it is interesting to investigate how the results are affected by RE. The results in 1D and 3D binning are in the figures 4.17–4.23. The correction is the largest at high x, low z and high P_T. The effect for $A_{UU}^{\cos\phi_h}$ and $A_{UU}^{\cos 2\phi_h}$ is in the order of percent. No effect of the RC is observed for $A_{LU}^{\sin\phi_h}$ as expected. In some 3D bins, an unexpected sign change of $A_{UU}^{\cos 2\phi_h}$ from negative to positive values is present.

One of the puzzles of the 2016 unpolarised azimuthal asymmetries was the Q^2 dependence of $A_{UU}^{\cos\phi_h}$. Being proportional to $\frac{1}{Q}$ (see eq. 1.13), a decrease of $|A_{UU}^{\cos\phi_h}|$ with Q^2 was expected. In contrast, a growth of the amplitude with Q^2 was observed, already in the asymmetries obtained from a reduced data sample without RC [44]. Interestingly, the effect is still present in the measured results after the radiative correction, as visible in figure 4.24.

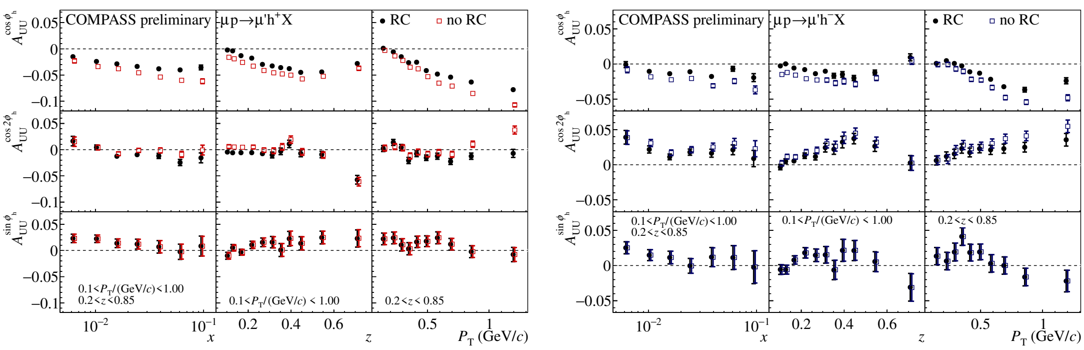

Figure 4.17: The comparison of the azimuthal asymmetries before and after applying RC for (left) h^{+} and (right) h^{-}.

The effect of RC on the P_{T}^{2}-distributions without identification

The effect of the RC on the P_{T}^{2}-distributions is small, so we do not directly compare the results before and after RC. To better visualise the size of the effect, the η distributions are presented in the figure 4.25. The values of η represent the size of the correction for the individual P_{T}^{2} bins. Since they show a linear dependence, they are fitted with a linear function in the following form:

$$f(P_{\mathrm{T}}^{2}) = p_0(1 + p_1 P_{\mathrm{T}}^{2}) \ . \tag{4.19}$$

The results of the fit are the parameters p_0 and p_1. The results for the linear slopes are plotted in figure 4.26. Although correction with such slopes does not result in a visual difference of the values in P_{T}^{2}-distributions and their double exponential fits, the correction leads to a difference of the final slope of the fit $\langle P_{\mathrm{T}}^{2}\rangle$ up to an order of its statistical error. Due to this observation, the RC for the P_{T}^{2}-distributions cannot be neglected.

The effect of RC on UAs of identified hadrons

Due to the azimuthal asymmetries of K being so large the effect of RC is presented in the figure 4.27 in terms of $A_{\mathrm{RC}}^{f(\phi_{\mathrm{h}})}$ amplitudes of azimuthal modulations obtained by fitting the cross-section 1.9 on the η distributions. The theory does not predict any differences between $\mathrm{h}^{\pm}$. There seems to be no dependence on the size of the effect before correction, otherwise the effect would be larger for K than for π. The effect size is in line with observations in the analysis without identification – the order of precent for $A_{\mathrm{UU}}^{\cos\phi_{\mathrm{h}}}$ and $A_{\mathrm{UU}}^{\cos 2\phi_{\mathrm{h}}}$, compatibility of the effect with zero for $A_{\mathrm{LU}}^{\sin\phi_{\mathrm{h}}}$.

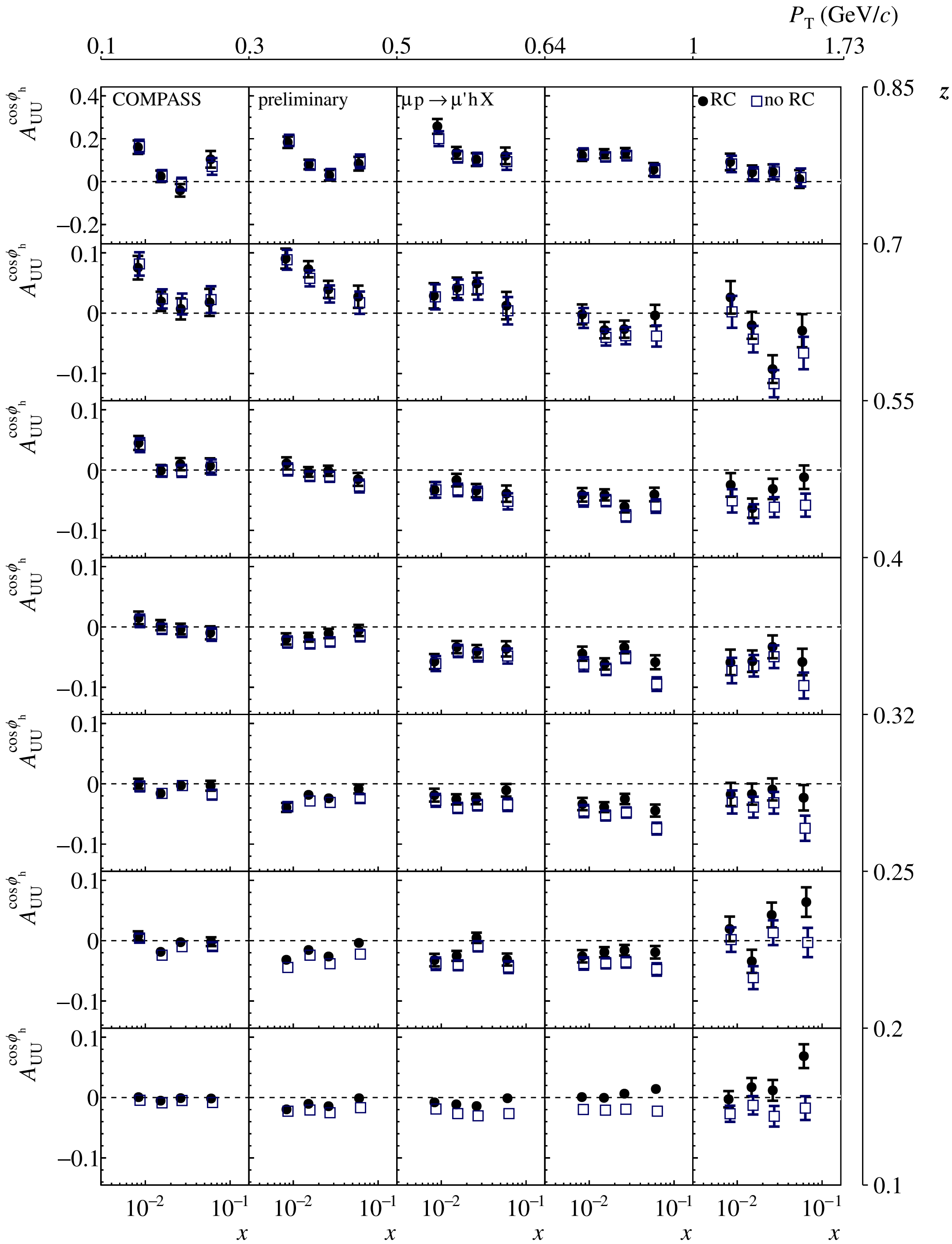

Figure 4.18: The comparison of $A_{UU}^{\cos\phi_h}$ before and after applying RC for h^-.

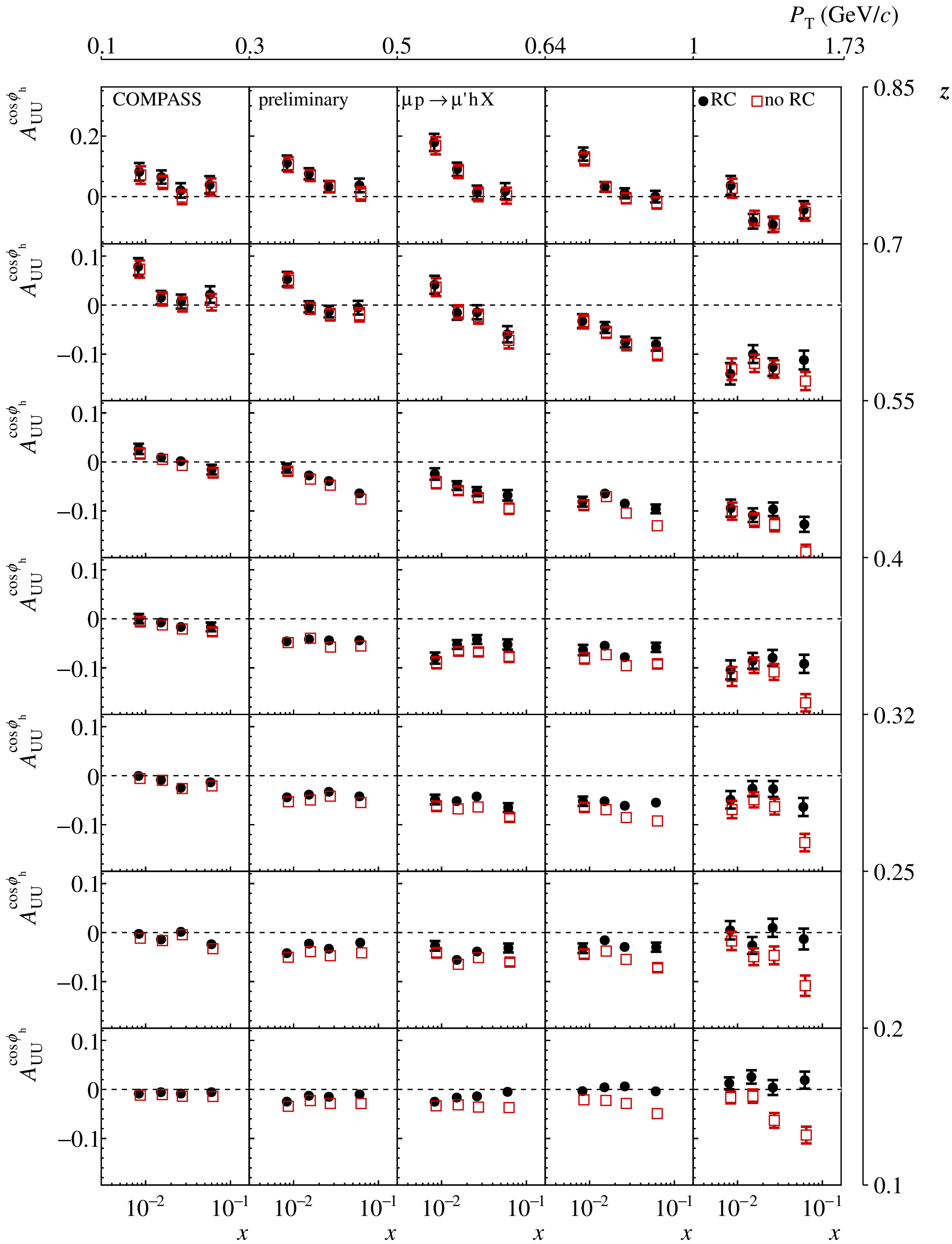

Figure 4.19: The comparison of $A_{\mathrm{UU}}^{\cos\phi_{\mathrm{h}}}$ before and after applying RC for h^{+}.

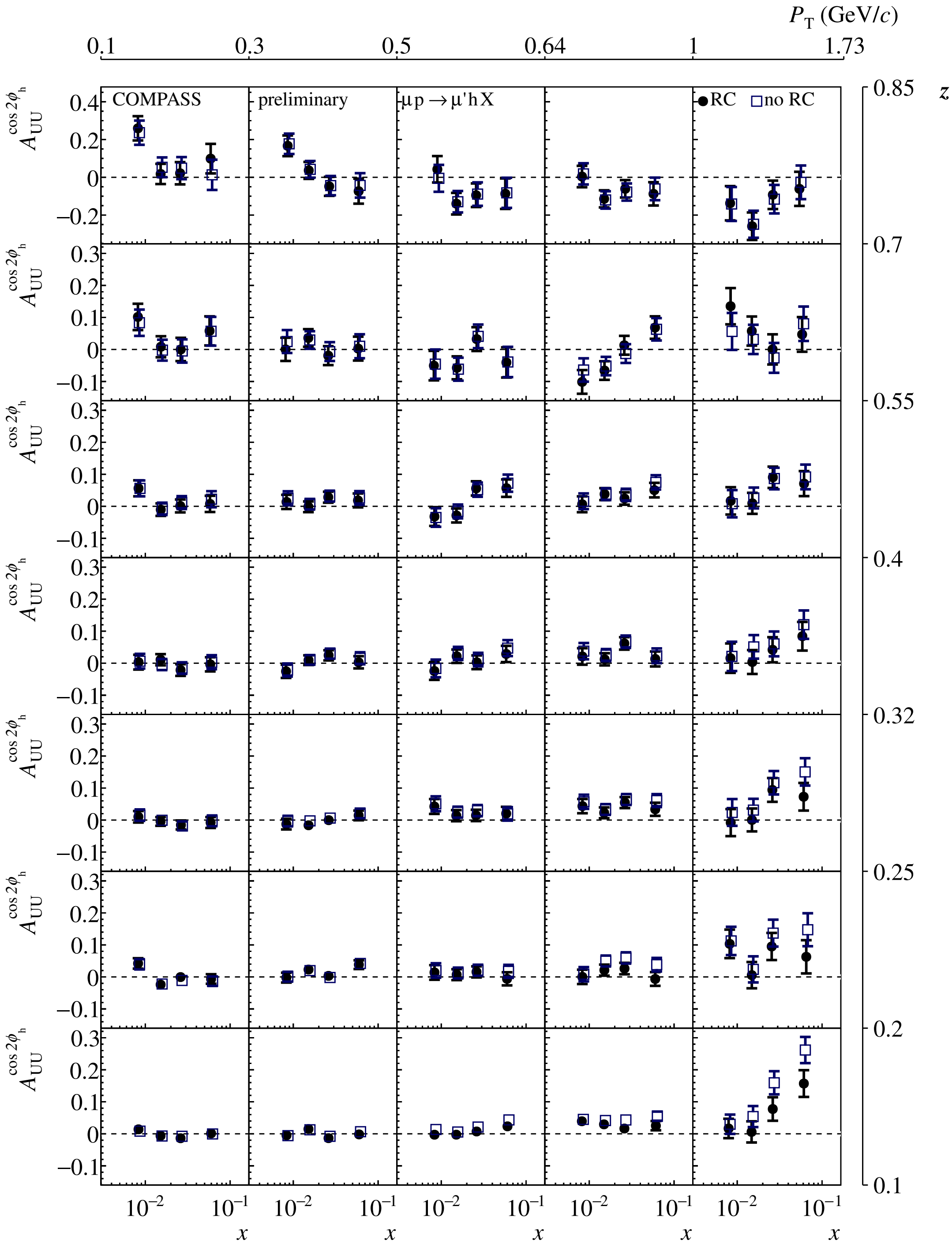

Figure 4.20: The comparison of $A_{\mathrm{UU}}^{\cos 2\phi_{\mathrm{h}}}$ before and after applying RC for h^{-}.

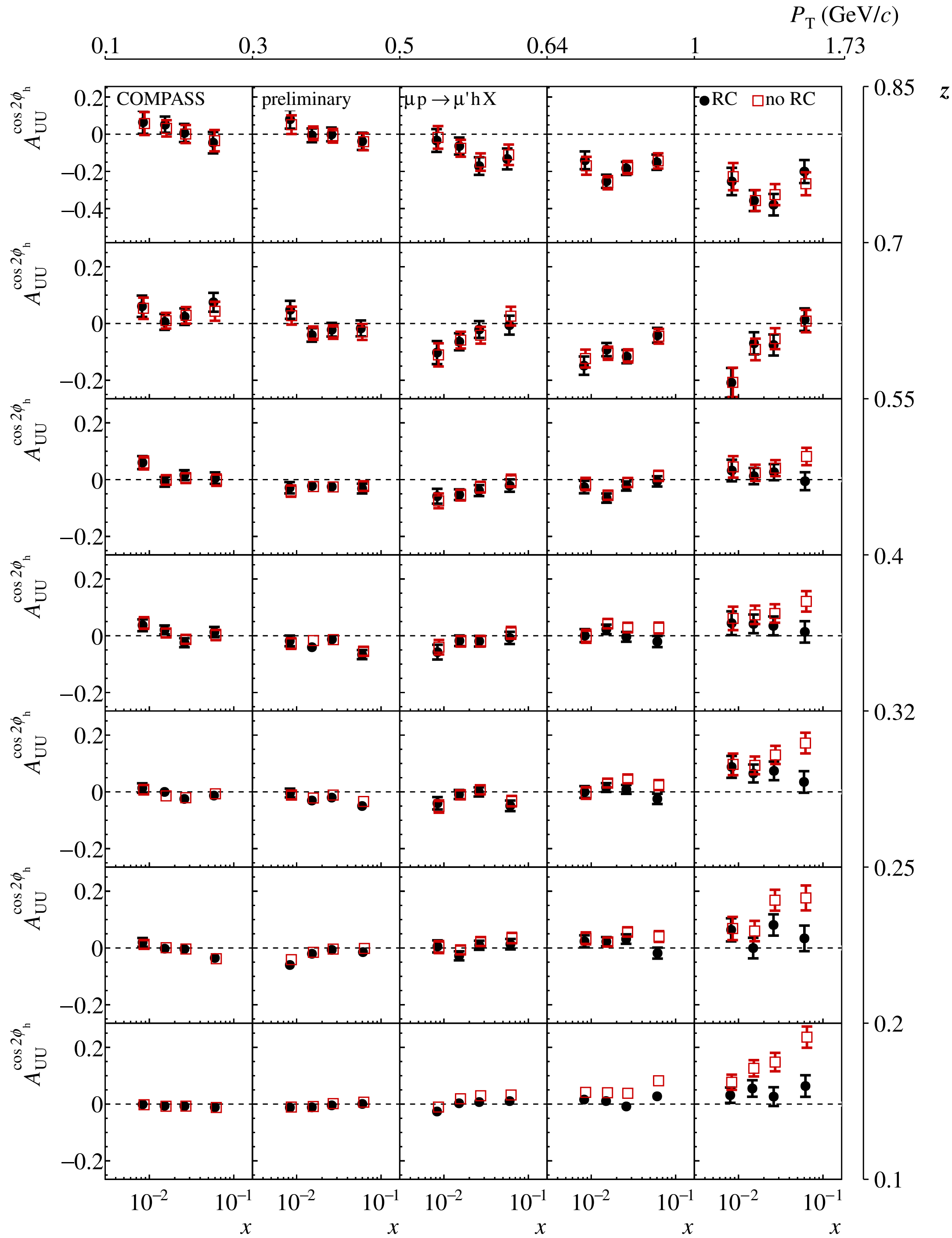

Figure 4.21: The comparison of $A_{\rm UU}^{\cos 2\phi_{\rm h}}$ before and after applying RC for $\rm h^{+}$.

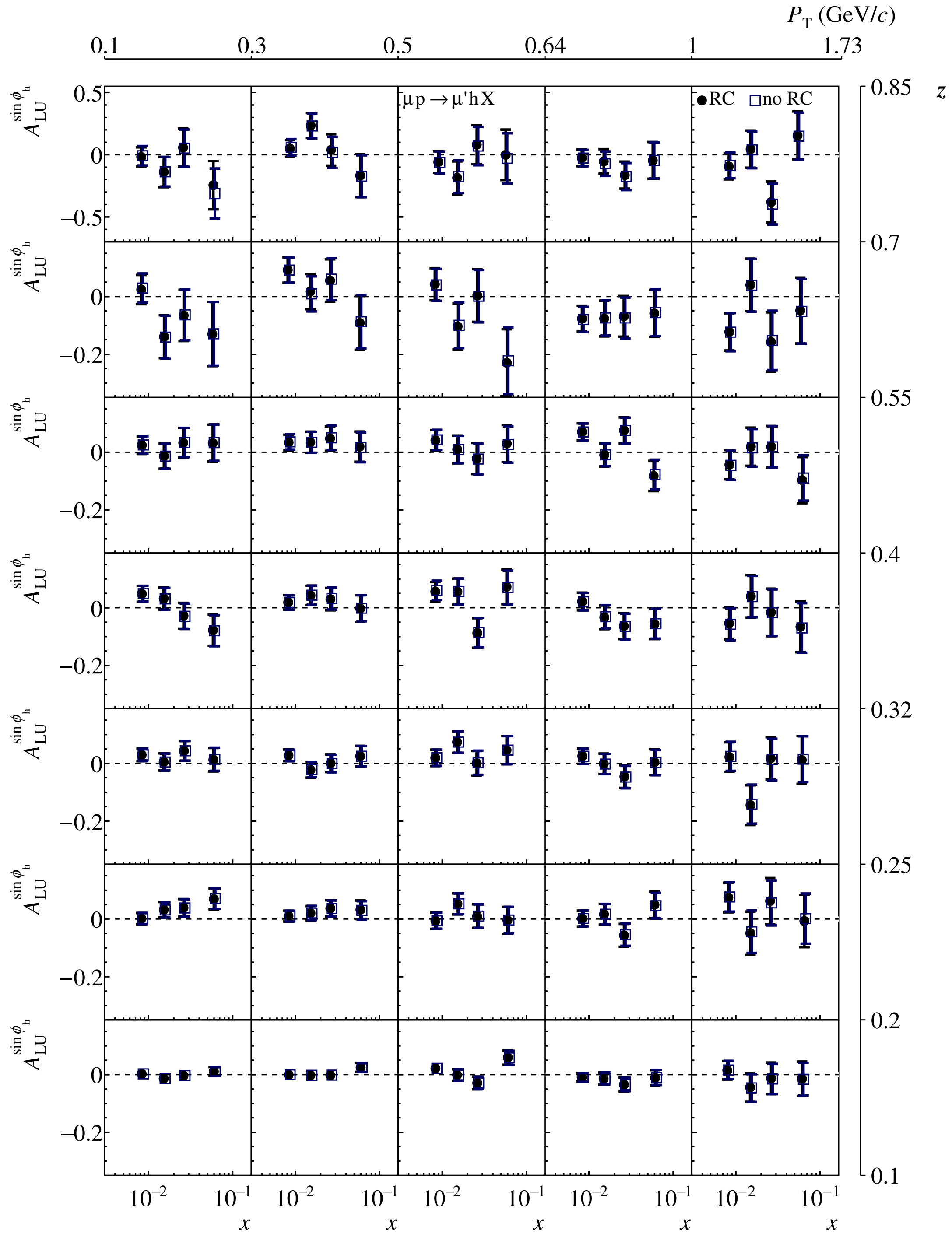

Figure 4.22: The comparison of $A_{\mathrm{LU}}^{\sin\phi_{\mathrm{h}}}$ before and after applying RC for h^{-}.

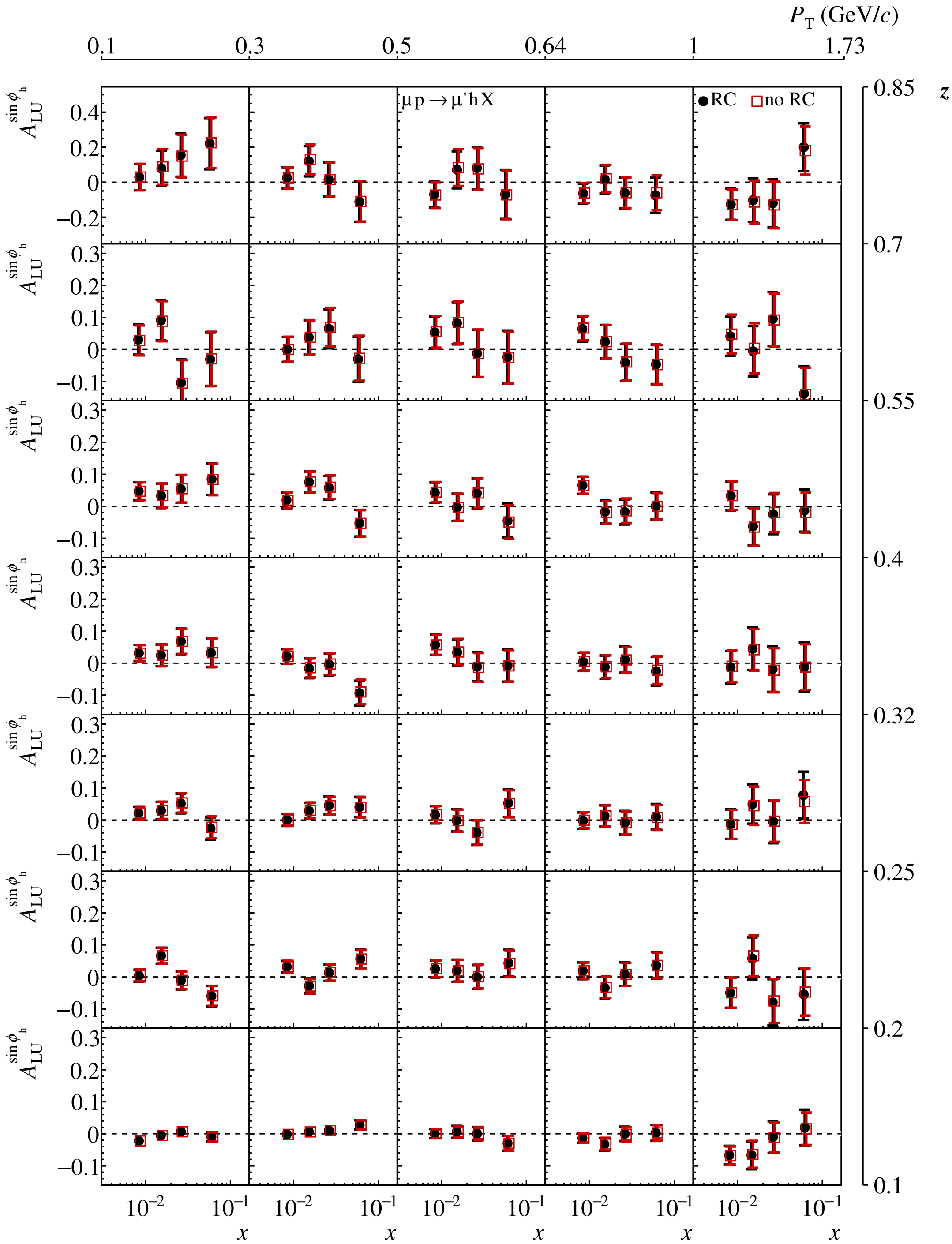

Figure 4.23: The comparison of $A_{\mathrm{LU}}^{\sin\phi_{\mathrm{h}}}$ before and after applying RC for h^{+}.

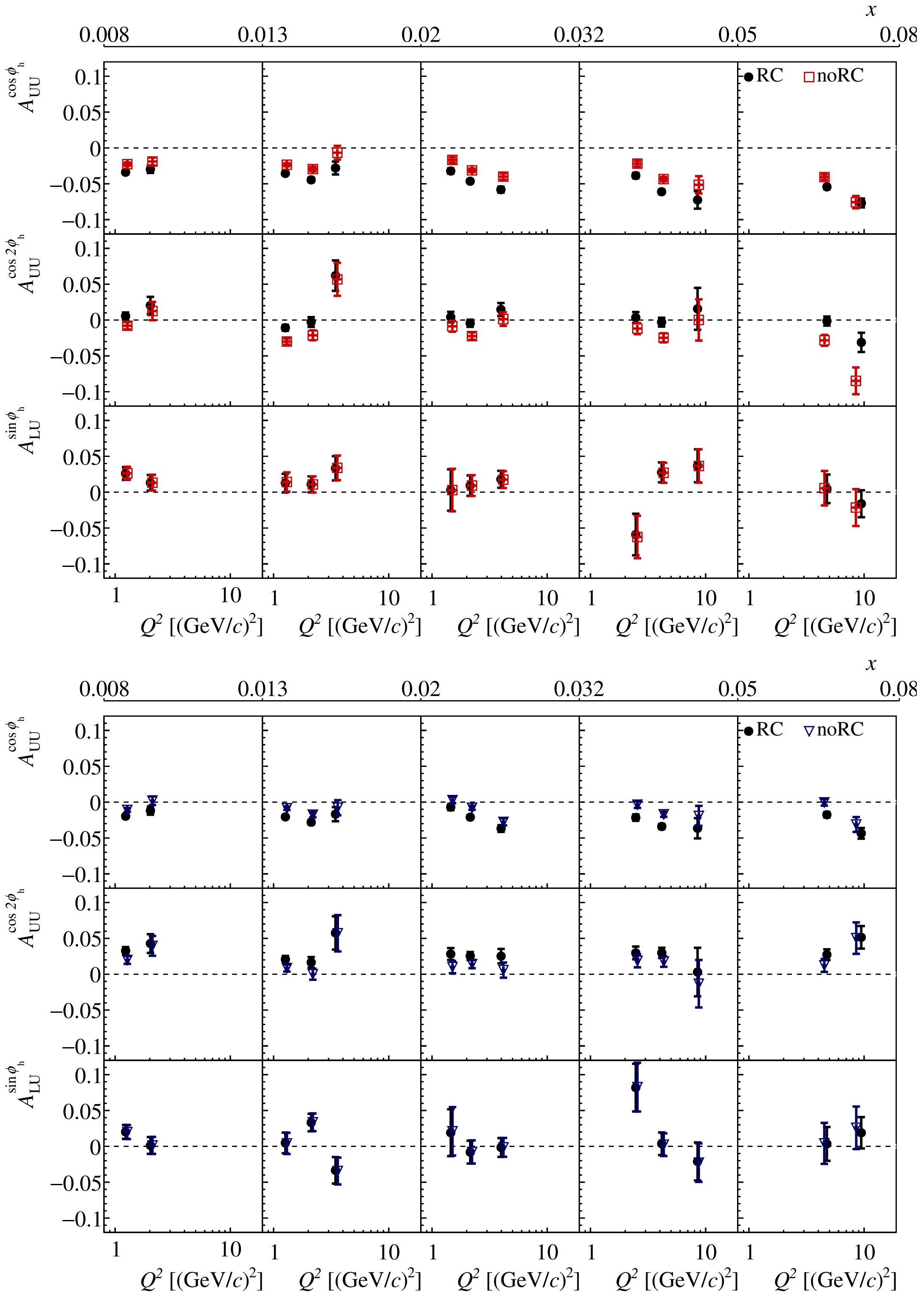

Figure 4.24: The comparison of the azimuthal asymmetries before and after applying RC in 2D $x : Q^2$ binning for (top) h$^+$ and (bottom) h$^-$.

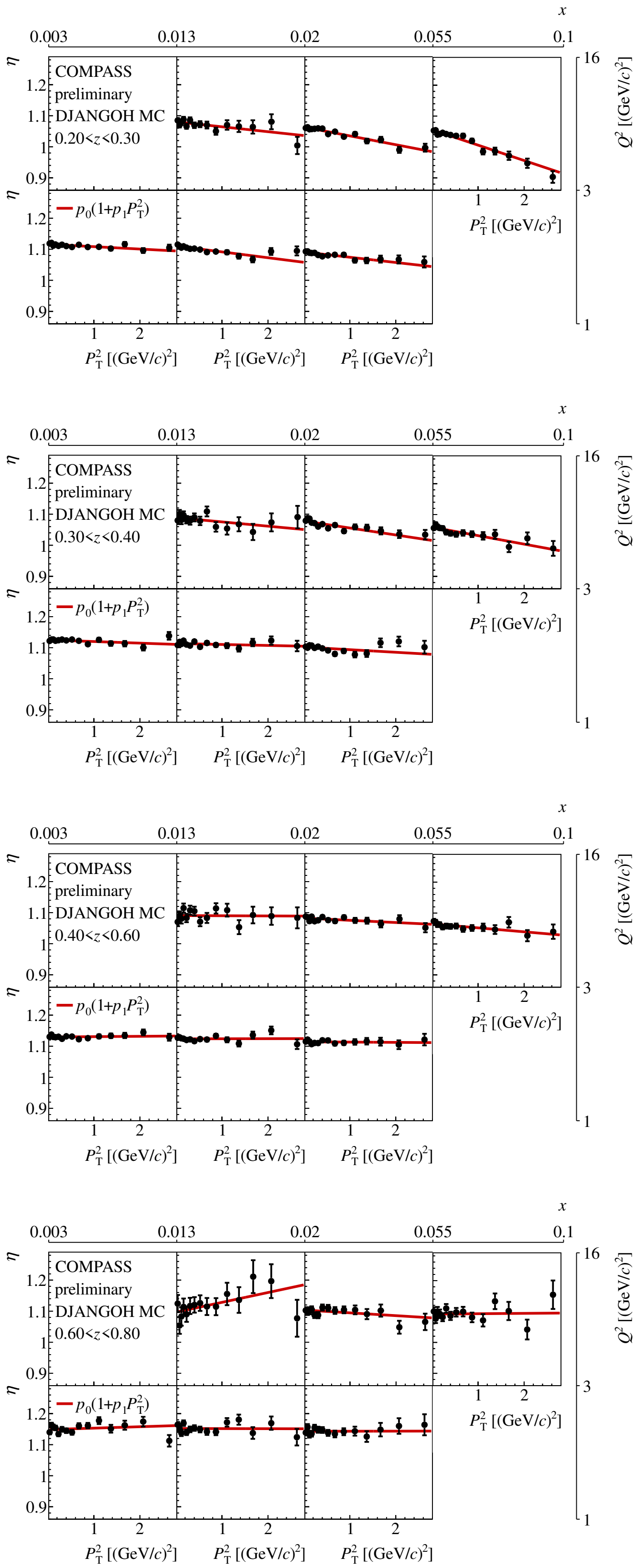

Figure 4.25: The final results for the η distributions in 4D $P_T^2 : x : Q^2 : z$ binning for both h$^+$ and h$^-$ together. The plots go from the lowest z bin (top) to the last z bin (bottom) with the x and Q^2 dependence represented with the top and right axes. Plots contain curves that represent linear fits.

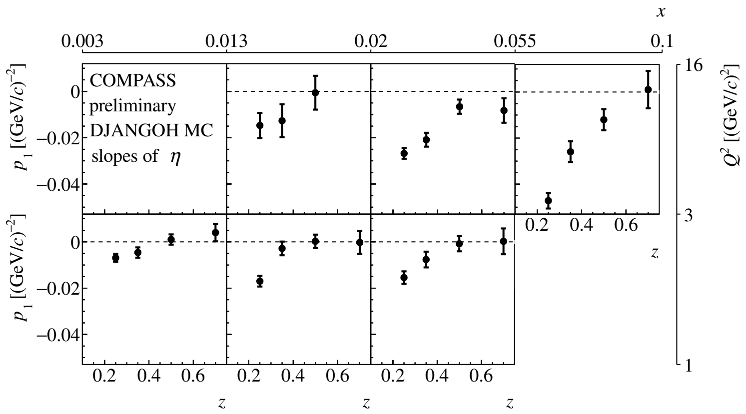

Figure 4.26: The final results of the linear fit of the radiative corrections for the P_{T}^{2}-distributions performed in figure 4.25.

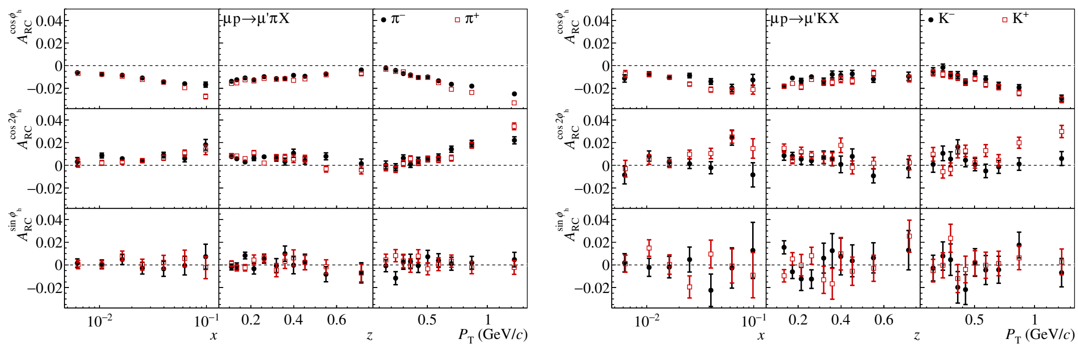

Figure 4.27: The comparison of the amplitudes of azimuthal modulations in η distributions for π (left) and K (right).

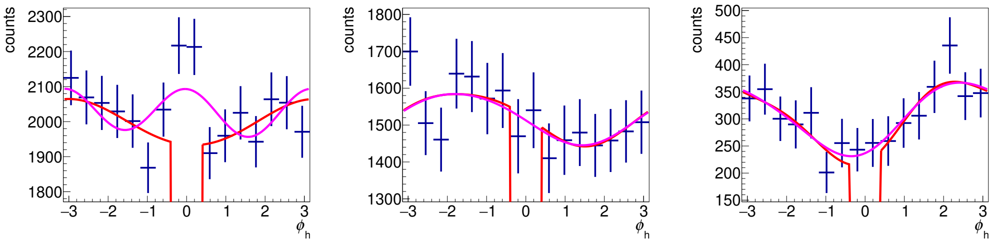

Figure 4.28: Distributions of ϕ_h for P08 μ^+, first x bin, h^+, corrected only on acceptance as in analysis of unidentified hadrons (left), for pions only (middle) and for kaons (right). In the plots, fits of the full region (magenta) and fits with the central region excluded (red) are being visually compared.

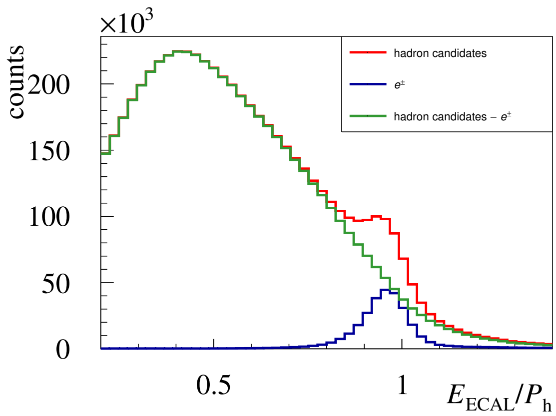

Figure 4.29: Distributions of $\frac{E_\mathrm{ecal}}{P_\mathrm{h}}$ for all hadron candidates in reconstructed DJANGOH MC (red), misidentified $\mathrm{e}^\pm$ (blue) and their difference (green).

4.7 Electron contamination from ISR and FSR

Hadron sample selected in the process of selection in the section 4.1 can still contain e^+ and e^- converted from initial- and final-state radiation (ISR and FSR) photons. Since the photon is emitted in the leptonic plane of GNS, the products of its conversion should have $\phi_\mathrm{h} \approx 0$. The contamination is visible as a narrow peak around 0, as shown in the figure 4.28. The standard way to treat this contamination is to exclude the central region of the ϕ_h histograms from the fit.

The 2016 data sample has had problems with Z_vertex dependence of the azimuthal asymmetries [30]. One of the many proposed explanations was that this dependence originates from the misidentified electrons since their amplitudes of azimuthal modulation could be Z_vertex dependent due to the different material lengths travelled by the radiating particle in the target. By observing the distributions of $\frac{E_\mathrm{ecal}}{P_\mathrm{h}}$, which is plotted in figure 4.29, we tried to use calorimeter information to exclude the $\mathrm{e}^\pm$ peak from the analysis by the following cut:

$$\frac{E_\mathrm{ecal}}{P_\mathrm{h}} < 0.7 \tag{4.20}$$

We tested the hypothesis of improvement in the Z_vertex dependence by calculating the azimuthal asymmetries with and without the E_ecal cut applied and for the region of $e^{\pm}$ in 4 Z_{vertex} bins, as was also done to evaluate this systematic effect in [30]. The test did not effectively eliminate the Z_{vertex} dependence of the azimuthal asymmetries, as evident in figure 4.30. The sample defined by $\frac{E_{\mathrm{ecal}}}{P_{\mathrm{h}}} > 0.7$ which contains a large fraction of electrons, does exhibit the Z_{vertex} trend of concern strongly enhanced, supporting the hypothesis that the electrons can be to blame. However, its removal does not have a significant effect on the final results and therefore is not used in the final analysis.

Intuition would suggest using RICH detector to eliminate ISR and FSR-originated electrons from the hadron data sample. However, COMPASS RICH detector was tuned for π–K–p separation, therefore we cannot fully trust likelihood values for the $e^{\pm}$ hypothesis. In the analysis of identified hadrons, we employ the following $e^{\pm}$ veto cut:

$$\frac{\mathscr{L}_{\mathrm{e}}}{\mathscr{L}_{\pi}} > 1.8 \;, \tag{4.21}$$

where $\mathscr{L}_{\mathrm{e}}$ and $\mathscr{L}_{\pi}$ are likelihood values for $e^{\pm}$ and $\pi^{\pm}$ hypotheses respectively, which are provided as an output of RICH detector. It is visible in figure 4.28 that the presence of the central region is not as significant for the ϕ_{h} distributions for identified π and K. However, as we explored in the chapter 3, the efficiency in the $[-\frac{\pi}{8}, \frac{\pi}{8}]$ region is significantly worse, thus this region is excluded from the cross-section fit also in the case of identified hadrons.

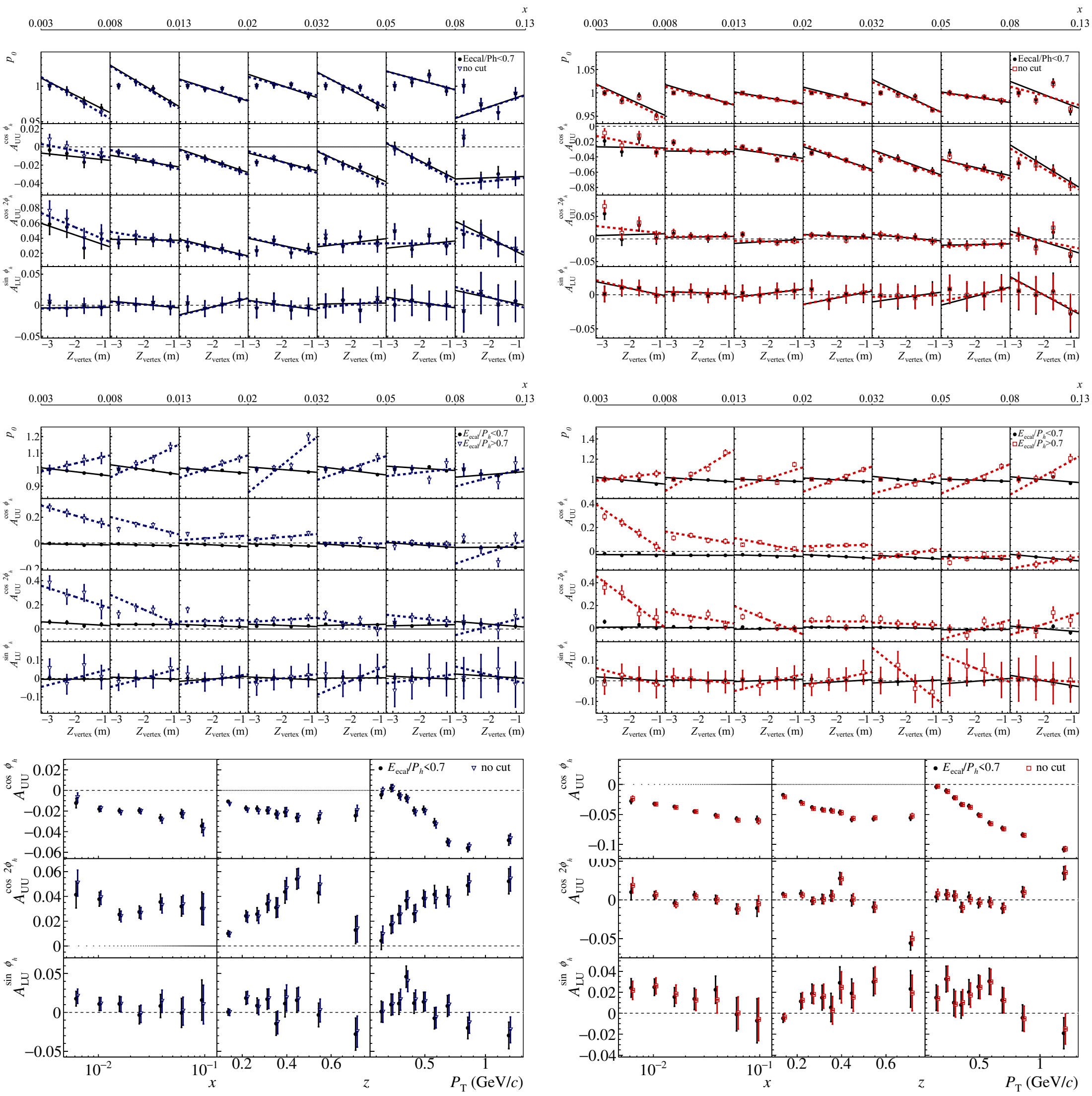

Figure 4.30: Azimuthal asymmetries and $p_0 \equiv \sigma_0$ in the $Z_{\text{vertex}} : x$ dependence with and without the E_{ecal} cut (top), with cut and for the region of e$^{\pm}$ (middle) and 1D binning without the E_{ecal} cut (bottom). Results for positive hadrons are compared on the right, negative hadrons on the left. Corrected on acceptance, invisible hadrons from DVM decays not removed.

5. Results

The results are presented in Section 5.1 for the UAs and in Section 5.4 for the P_T^2-distributions. A comparison with previous COMPASS results on the deuteron target was performed to investigate potential flavour dependence. Additionally, results were cross-checked against measurements from the kinematically similar HERMES experiment to provide an independent validation of the findings presented in this thesis. The results for P_T^2-distributions with hadron identification applied were not finalised at the time of thesis submission and are therefore not included in this chapter.

5.1 Results of the measurement of UAs

The final results for azimuthal asymmetries are in figures 5.1–5.4. The plots include both statistical and systematic uncertainty. Contributions to the systematic uncertainty from period compatibility and Z_{vertex} dependence were evaluated already in [30]. In 5.1–5.4 the systematic error evaluation was extended for contributions from RC, acceptance correction, and background treatment. In all cases, the contribution is proportional to the size of the correction, with an optional constant term. The scaling factor is determined according to the agreement of the measured data and the MC sample used for the correction (kinematical distributions are usually compared, in the case of HEPGEN, azimuthal modulations of visible pairs).

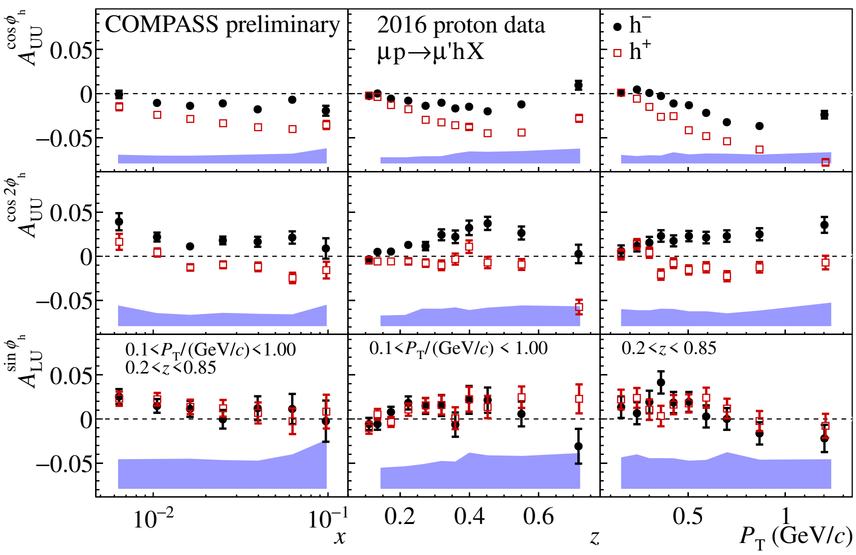

Figure 5.1: The final results for azimuthal asymmetries in the 1D binnings. The blue band represents systematic uncertainty and is common for h^+ and h^-.

The final results for azimuthal asymmetries for π and K separately are in figure 5.5. For better comparison, the results are grouped differently in figure 5.6. The systematic error for these results has not yet been estimated.

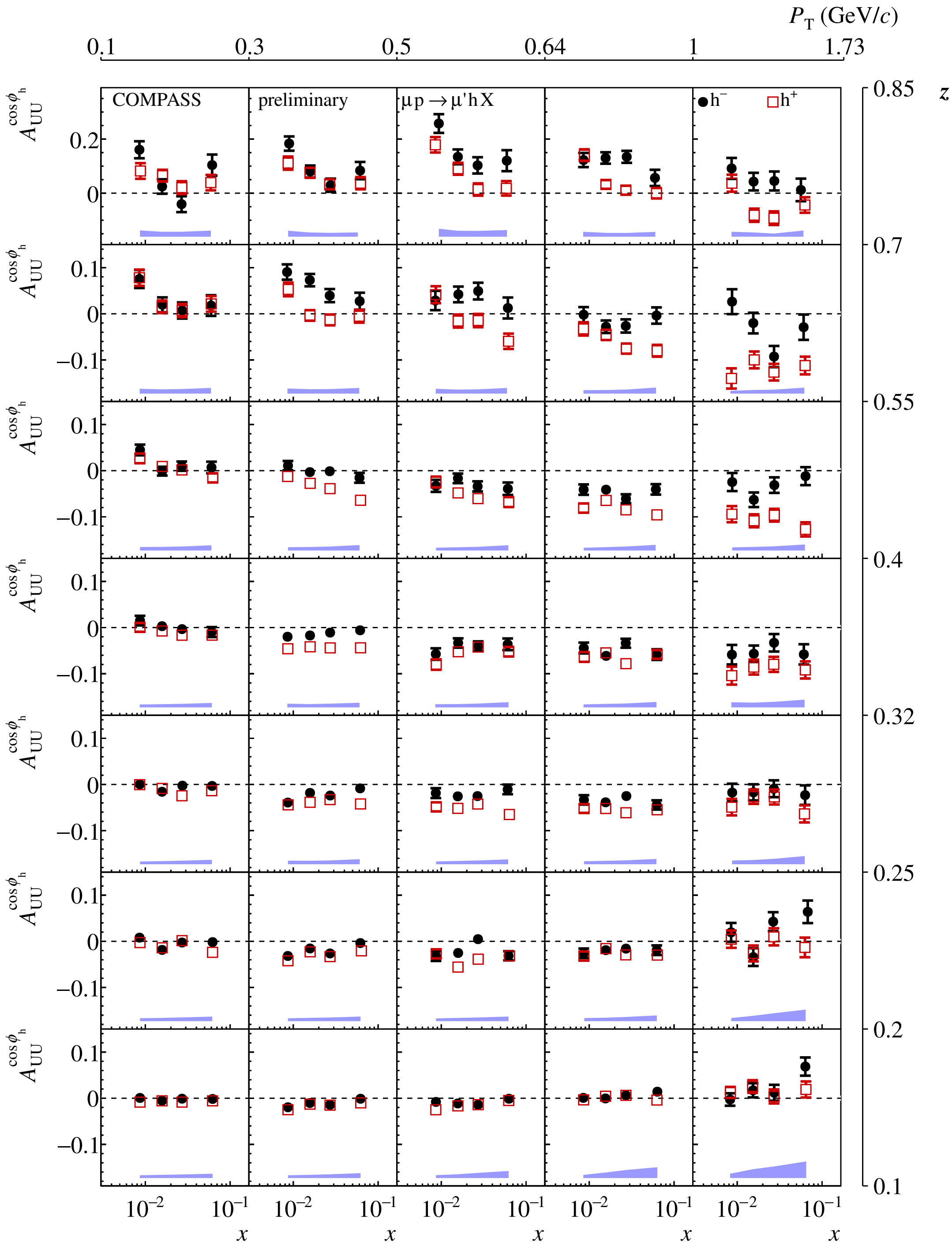

Figure 5.2: The final results for $A_{UU}^{\cos\phi_h}$ in the 3D binning. The blue band represents systematic uncertainty and is common for h^+ and h^-.

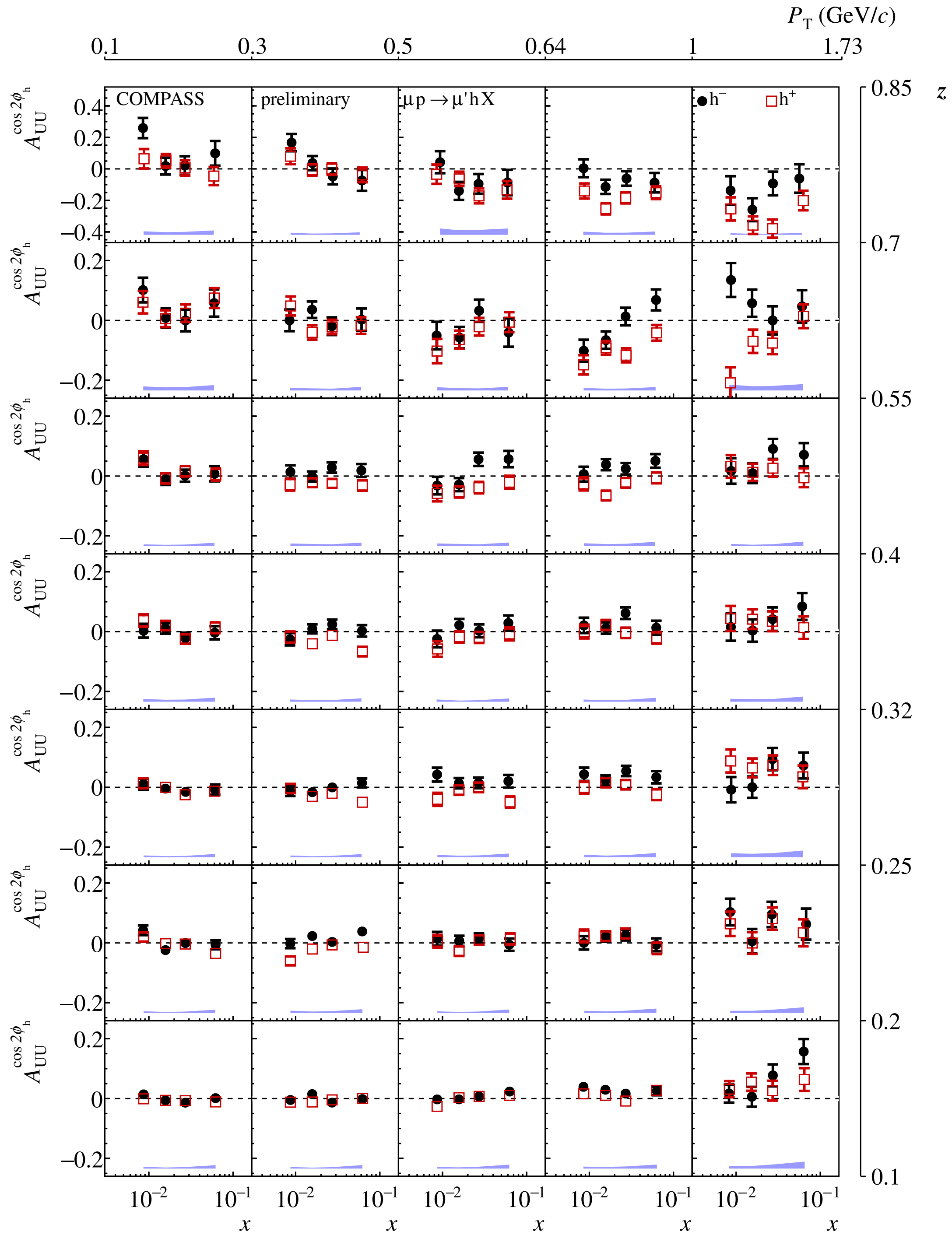

Figure 5.3: The final results for $A_{\mathrm{UU}}^{\cos 2\phi_{\mathrm{h}}}$ in the 3D binning. The blue band represents systematic uncertainty and is common for h^+ and h^-.

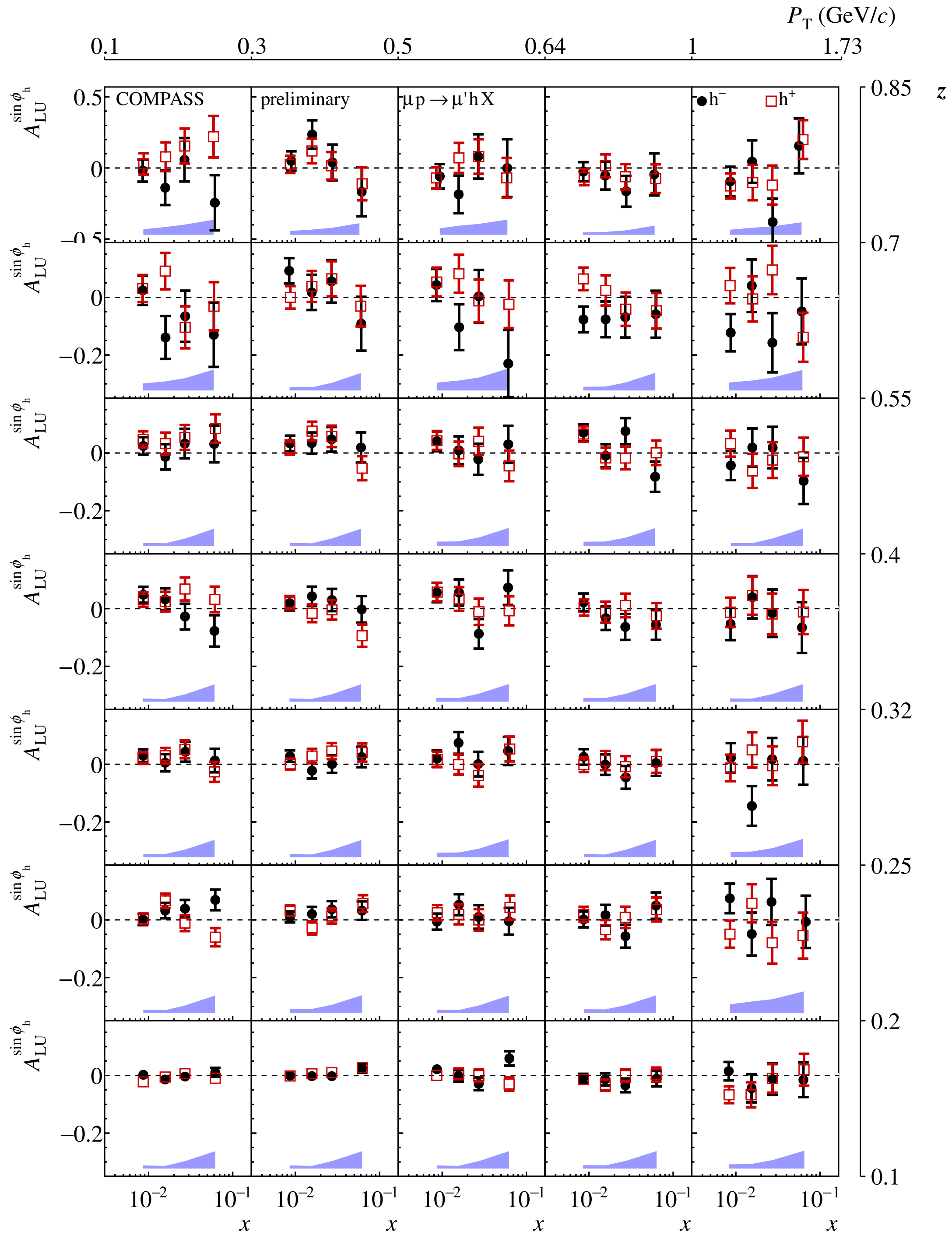

Figure 5.4: The final results for $A_{\mathrm{LU}}^{\sin\phi_{\mathrm{h}}}$ in the 3D binnings. The blue band represents systematic uncertainty and is common for h^+ and h^-.

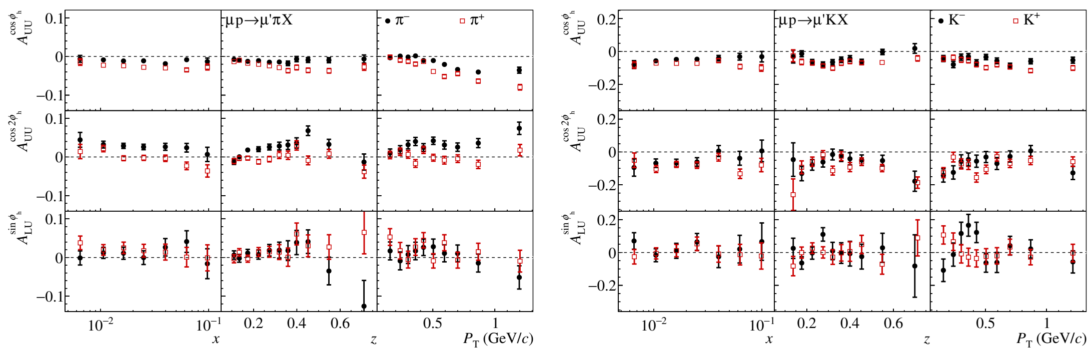

Figure 5.5: The final results for azimuthal asymmetries for π (left) and K (right).

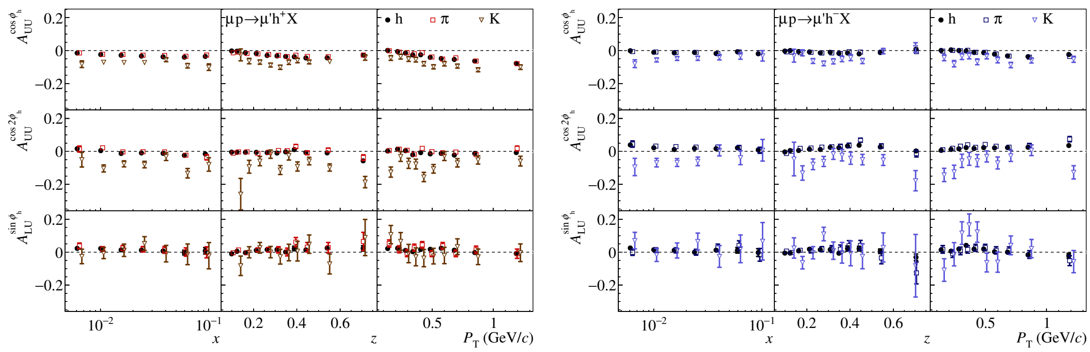

Figure 5.6: Direct comparison of azimuthal asymmetries from the analysis without identification, π and K. Positive hadrons (left) and negative hadrons (right).

5.1.1 Comparison with COMPASS results on deuteron

The COMPASS experiment measured unpolarised asymmetries on an isoscalar (deuteron) target in 2004 and published the first results in 2014 [6]. Later, the effect of the background from diffractive vector mesons (DVMs) was shown to be significant and the subtracted asymmetries in 3D binning were published [34]. To explore flavour dependence of the azimuthal asymmetries, we compare the up quark dominated results on proton from this work (not corrected on RC, contribution form RC not included in systematical error) with the results on isoscalar target in the figures 5.7. In theory, RE should not be target dependent; thus it is possible to make conclusions even when the results miss the RC.

The results for $A_{\mathrm{UU}}^{\cos\phi_{\mathrm{h}}}$ are systematically higher for proton with respect to deuteron and oppositely for $A_{\mathrm{UU}}^{\cos 2\phi_{\mathrm{h}}}$. However, the mean values are mostly within the error bars, apart from the high z region, where a difference over 2σ is visible. Differences in z dependence between proton and deuteron point to the flavour dependence of TMD-FFs of up and down quarks. Compatibility in the x dependence points to the same TMD-PDFs for valence quarks up and down.

5.2 Comparison with HERMES results

Cross-checking the results between independent experiments helps confirm that the findings are not specific to a particular setup, analysis method, or detector system. Published results for $\varepsilon_1 A_{\mathrm{UU}}^{\cos\phi_{\mathrm{h}}} \equiv 2\langle\cos\phi\rangle$ and $\varepsilon_2 A_{\mathrm{UU}}^{\cos 2\phi_{\mathrm{h}}} \equiv 2\langle\cos 2\phi\rangle$ from

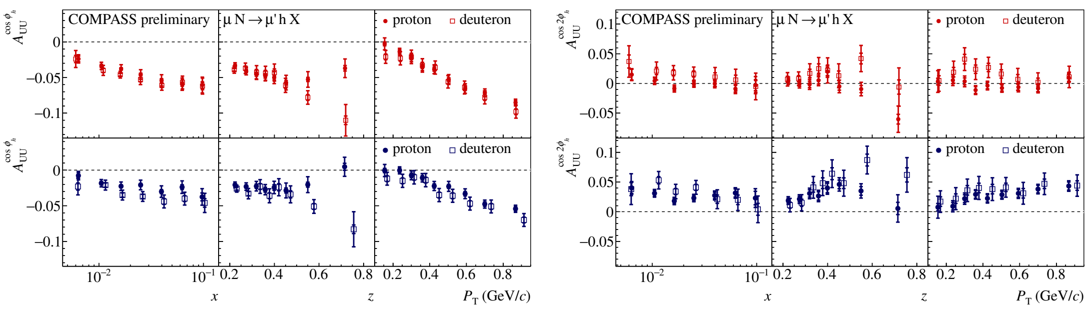

Figure 5.7: The comparison of the COMPASS results for azimuthal asymmetries measured on proton (full dot) and deuteron (empty squares). Results for $A_{\mathrm{UU}}^{\cos\phi_{\mathrm{h}}}$ (left), for $A_{\mathrm{UU}}^{\cos 2\phi_{\mathrm{h}}}$ (right), positive hadrons (red), negative hadrons (blue).

the HERMES collaboration, which are shown in figure 5.8, are ideal for comparison due to the similarity of the kinematical coverage of the two experiments [45]. Although their results are not corrected for the background from DVMs nor kinematical factors ε, we can make some basic conclusions from the qualitative properties of the results. Observation of a larger effect for K and a negative value of $2\langle\cos 2\phi\rangle$ for K is in agreement with our analysis. Additionally, the compatibility is also in the results for π that are similar to the results for the analysis without identification, $2\langle\cos 2\phi\rangle$ for π^+ slightly positive, for π^- around zero. However, for $2\langle\cos\phi\rangle$ there is a bigger difference between positive and negative π in our results.

Similar to COMPASS, the amplitudes of the azimuthal modulations on a deuteron target were also measured by the HERMES experiment [45]. Their comparison of the $A_{\mathrm{XU}}^{f(\phi_{\mathrm{h}})}$ amplitudes on proton and deuteron targets does not exhibit the difference at large z that is observed in our analysis (see Figure 5.7). This discrepancy could be attributed to the significant contribution of background from DVM decays, which are not accounted for in the HERMES analysis and which are expected to contribute in the same way for both targets.

5.3 Comparison with JLab results

Although the measured $A_{\mathrm{LU}}^{\sin\phi_{\mathrm{h}}}$ at COMPASS is close to zero, the CLAS and its successor CLAS12 experiments at JLab (e p → e h X), which operate at higher values of x and benefit from significantly higher statistics, observe a positive asymmetry. The comparison of results for $A_{\mathrm{LU}}^{\sin\phi_{\mathrm{h}}}$ of positive hadrons from CLAS and CLAS12 experiments at JLab with HERMES and COMPASS results on deuteron can be done using published results [46, 6, 47]. No other azimuthal asymmetries have been published by JLab to date.

5.4 Results for P_{T}^2-distributions without identification

The final results for P_{T}^2-distributions are shown in figure 5.9, while the results of the double exponential fit in terms of $\langle P_{\mathrm{T}}^2\rangle$ are presented in figure 5.10. The

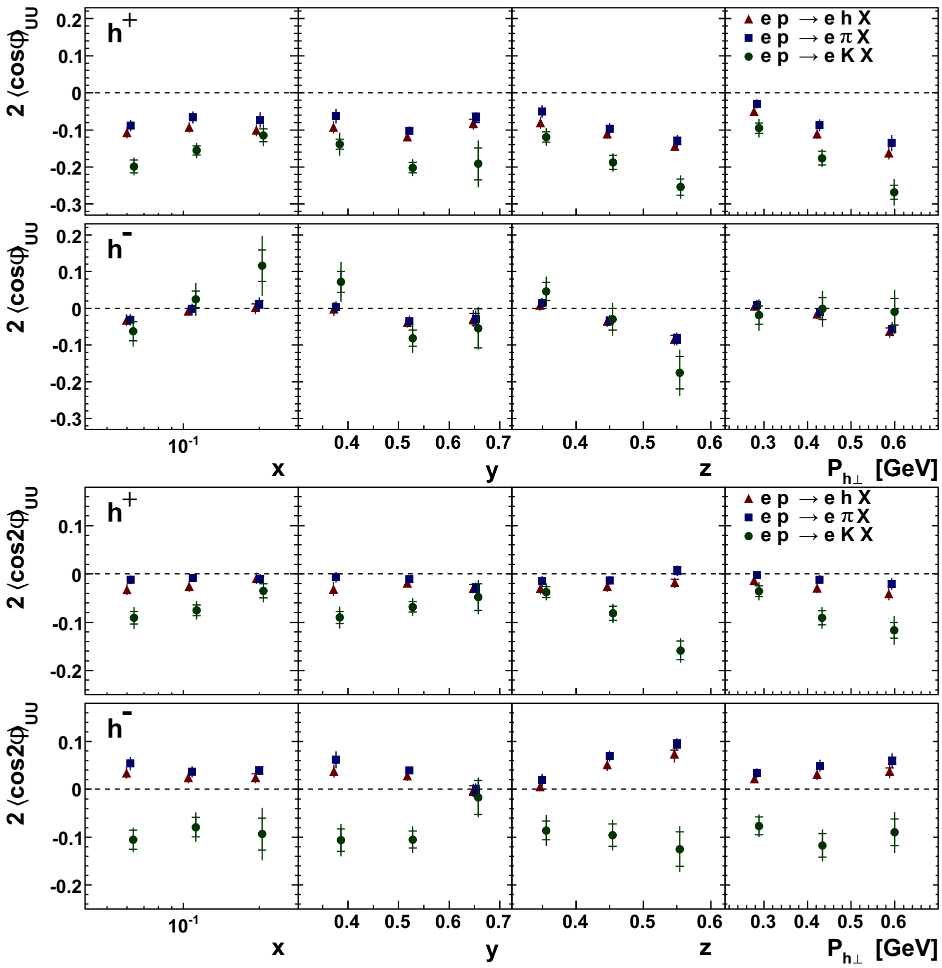

Figure 5.8: The results for $\varepsilon_1 A_{\mathrm{UU}}^{\cos\phi_{\mathrm{h}}} \equiv 2\langle\cos\phi\rangle$ and $\varepsilon_2 A_{\mathrm{UU}}^{\cos 2\phi_{\mathrm{h}}} \equiv 2\langle\cos 2\phi\rangle$ from HERMES [45].

shape of the P_{T}^2-distributions is visually well described by the double exponential model. The mean transverse momentum squared is approximately 0.4 $(\mathrm{GeV}/c)^2$ and exhibits a rising trend with increasing z and Q^2. Since the analysis of the P_{T}^2-distributions is still in an early phase, the results will be subject to further refinement. Subsequently, the equation 1.18 can be used for the separation of the intrinsic quark transverse momentum $\langle k_{\mathrm{T}}^2 \rangle$ and $\langle P_{\perp}^2 \rangle$ from fragmentation [48].

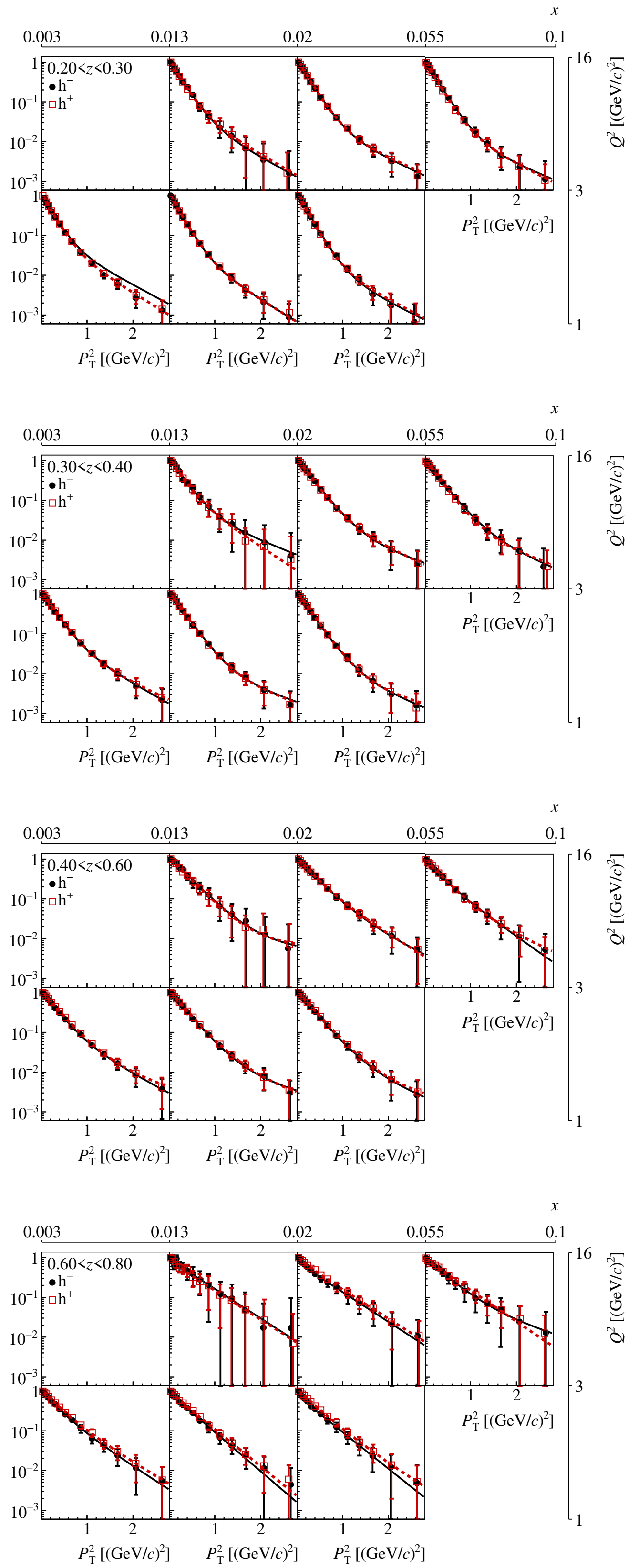

Figure 5.9: The final results for the P_{T}^2-distributions in 4D $P_{\mathrm{T}}^2 : x : Q^2 : z$ binning for h^+ and h^-. The plots go from the lowest z bin (top) to the last z bin (bottom) with the x and Q^2 dependence represented with the top and right axes. Plots contain curves that represent double exponential fits.

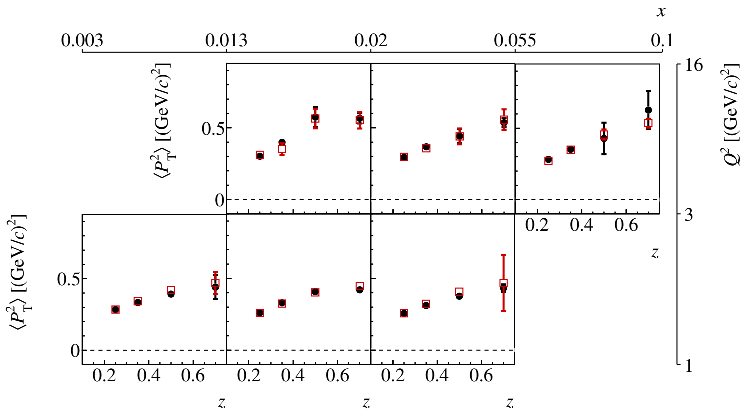

Figure 5.10: The final results for $\langle P_{\mathrm{T}}^2 \rangle$ of h^+ (red) and h^- (black).

Conclusion

We presented a brief overview of the kinematics relevant to DIS and SIDIS, including the commonly used observables and conventions for describing these processes. An introduction to the theoretical framework of TMD-PDFs was provided, with specific examples of functions contributing to SIDIS off an unpolarised target. We also outlined the methodology for extracting these functions from experimental measurements of azimuthal asymmetries and P_{T}^2-distributions. In particular, the *Boer–Mulders* function $h_1^{\perp}$ contributes dominantly to the $\cos 2\phi_h$ modulation and can thus be accessed through measurements of $A_{\mathrm{UU}}^{\cos 2\phi_{\mathrm{h}}}$. In addition, we discussed the *Cahn* effect, which gives rise to a negative $\cos\phi_{\mathrm{h}}$ modulation. The theoretical framework and Gaussian model for TMDs predict an exponential shape of P_{T}^2-distributions.

The COMPASS experiment was designed to study the structure of nucleons by investigating data collected by a 60 m long two-stage spectrometer. Its 2016–2017 setup equipped with an unpolarised liquid hydrogen target combined with a muon or anti-muon beam was dedicated to HEMP, DVCS, and SIDIS measurements. We explored parts of COMPASS 2016–2017 spectrometer relevant for hadron identification.

We present results for unpolarised azimuthal asymmetries of charged (not-identified) hadrons, expanding upon the work initiated in the bachelor's thesis of the author [30]. The analysis was extended to include corrections for contributions from the decay of diffractively produced vector mesons and corrections on radiative effects. The implementation of radiative corrections using the DJANGOH MC generator for unpolarised asymmetries, as presented in this work, represents a recent development within the COMPASS collaboration. After all the corrections, the results are different for h^+ and h^-, which points to a flavour dependence of TMDs. The results for $A_{\mathrm{UU}}^{\cos\phi_{\mathrm{h}}}$ are mostly negative, which was predicted due to the Cahn effect with a negative weight dominating within the convolution describing the relevant structure function. Asymmetry $A_{\mathrm{UU}}^{\cos 2\phi_{\mathrm{h}}}$ exhibit an interesting mirror symmetry between h^+ and h^- at high x, consistent with theoretical predictions [16]. The measured effect for $A_{\mathrm{LU}}^{\sin\phi_{\mathrm{h}}}$ is close to being compatible with zero. The results are currently being prepared for publication.

To explore the flavour dependence, we compared results from this thesis (SIDIS off proton target) to the COMPASS results off deuteron target. The observed differences in the z-dependence between the proton and deuteron results indicate a flavour dependence of the up and down quark TMD-FFs. In contrast, the compatibility of the x-dependence suggests that the valence up and down quark TMD-PDFs are similar.

Another comparison was made between the results of this thesis and those from the kinematically similar HERMES and JLab experiment. The results are consistent in the sign of $A_{\mathrm{UU}}^{\cos 2\phi_{\mathrm{h}}}$ for kaons and in the observation of larger asymmetries for kaons compared to pions. However, at HERMES, the differences between h^+ and h^-, as well as between proton and deuteron targets, appear much less significant. While the results for $A_{\mathrm{LU}}^{\sin\phi_{\mathrm{h}}}$ at COMPASS are close to zero, measurements from JLab indicate a clear positive asymmetry for positive hadrons.

For the first time at COMPASS, we attempted to use RICH detector to extract azimuthal asymmetries and P_{T}^2-distributions of identified hadrons. Because acceptance correction does not account for the RICH detector, estimation of the ϕ_{h} dependence of RICH detector efficiencies was essential for accomplishing this task due to the correlation of the two observables. Results for ϕ_{h} dependent RICH performance are also presented in this thesis. Momentum and polar angle dependence of the efficiencies is in agreement with previous analyses of RICH performance.

The results for the azimuthal asymmetries of the identified π closely resemble the results of not identified hadrons, which is expected due to the dominance of pions within the hadron sample. Around 78% of hadron candidates were identified as pions. All corrections were in line with the expectations from studies of MC samples and results of the analysis without identification. The azimuthal asymmetries for K are larger than the asymmetries for π. This observation hints at a larger strange quark contribution to the convolutions of TMD-PDFs and TMD-FFs than for valence up and down quarks.

Preliminary results for the P_{T}^2-distributions and the extracted $\langle P_{\mathrm{T}}^2 \rangle$ values, obtained as the slopes of double-exponential fits, were also presented in this thesis. The values of $\langle P_{\mathrm{T}}^2 \rangle$ are of the order of 0.4 GeV^2/c^2 and show rising dependence on z, which should be connected to a bigger contribution of the transverse momentum from fragmentation in the same region. The newly implemented radiative corrections were applied to these observables as well. In this case, the impact of the correction was significantly smaller than for the azimuthal asymmetries, where the correction was comparable to the size of the measured effect. Nonetheless, radiative corrections cannot be neglected in the analysis of P_{T}^2-distributions, as their magnitude is comparable to the statistical uncertainty. The results of the analysis of P_{T}^2-distributions for identified hadrons are missing from this thesis due to time constraints.

Bibliography

[1] E. Rutherford, “The scattering of alpha and beta particles by matter and the structure of the atom,” *Phil. Mag. Ser. 6* **21** (1911) 669–688.

[2] R. P. Feynman, “Very high-energy collisions of hadrons,” *Phys. Rev. Lett.* **23** (1969) 1415–1417.

[3] M. Gell-Mann, “A Schematic Model of Baryons and Mesons,” *Phys. Lett.* **8** (1964) 214–215.

[4] G. D. Alexeev *et al.* (COMPASS), “High-statistics measurement of Collins and Sivers asymmetries for transversely polarized deuterons,” *Phys. Rev. Lett.* **133** no. 10, (2024) 101903, `arXiv:2401.00309 [hep-ex]`.

[5] G. D. Alexeev *et al.* (COMPASS), “Probing transversity by measuring Λ polarisation in SIDIS,” *Physics Letters B* **824** (Jan., 2022) 136834. `http://dx.doi.org/10.1016/j.physletb.2021.136834`.

[6] C. Adolph *et al.* (COMPASS), “Measurement of azimuthal hadron asymmetries in semi-inclusive deep inelastic scattering off unpolarised nucleons,” *Nuclear Physics B* **886** (Sept., 2014) 1046–1077. `http://dx.doi.org/10.1016/j.nuclphysb.2014.07.019`.

[7] R. Akhunzyanov *et al.* (COMPASS), “Transverse extension of partons in the proton probed in the sea-quark range by measuring the DVCS cross section,” *Physics Letters B* **793** (June, 2019) 188–194. `http://dx.doi.org/10.1016/j.physletb.2019.04.038`.

[8] G. D. Alexeev *et al.* (COMPASS), “Measurement of the hard exclusive π^0 muoproduction cross section at COMPASS,” 12, 2024. `https://arxiv.org/abs/2412.19923`.

[9] G. D. Alexeev *et al.*, “Multiplicities of positive and negative pions, kaons and unidentified hadrons from deep-inelastic scattering of muons off a liquid hydrogen target,” `arXiv:2410.12005 [hep-ex]`.

[10] G. Aad *et al.* (ATLAS), “A precise determination of the strong-coupling constant from the recoil of Z bosons with the ATLAS experiment at $\sqrt{s} = 8$ TeV,” 2023. `https://arxiv.org/abs/2309.12986`.

[11] A. Bacchetta, G. Bozzi, M. Radici, M. Ritzmann, and A. Signori, “Effect of flavor-dependent partonic transverse momentum on the determination of the W boson mass in hadronic collisions,” *Physics Letters B* **788** (Jan., 2019) 542–545. `http://dx.doi.org/10.1016/j.physletb.2018.11.002`.

[12] A. Bacchetta *et al.*, “Semi-inclusive deep inelastic scattering at small transverse momentum,” *JHEP* **02** (2007) 093, `arXiv:hep-ph/0611265`.

[13] J. C. Collins, D. E. Soper, and G. F. Sterman, “Factorization of Hard Processes in QCD,” *Adv. Ser. Direct. High Energy Phys.* **5** (1989) 1–91, `arXiv:hep-ph/0409313`.

[14] R. Boussarie *et al.*, "TMD Handbook," arXiv:2304.03302 [hep-ph].

[15] S. Bhattacharya, K. Cichy, M. Constantinou, A. Metz, A. Scapellato, and F. Steffens, "Twist-3 partonic distributions from lattice QCD," *SciPost Phys. Proc.* **8** (2022) 057, arXiv:2107.12818 [hep-lat].

[16] S. Bastami *et al.*, "Semi-inclusive deep-inelastic scattering in Wandzura-Wilczek-type approximation," *Journal of High Energy Physics* **2019** no. 6, (June, 2019) . http://dx.doi.org/10.1007/JHEP06(2019)007.

[17] R. N. Cahn, "Azimuthal Dependence in Leptoproduction: A Simple Parton Model Calculation," *Phys. Lett. B* **78** (1978) 269–273.

[18] P. Schweitzer, T. Teckentrup, and A. Metz, "Intrinsic transverse parton momenta in deeply inelastic reactions," *Physical Review D* **81** no. 9, (May, 2010) . http://dx.doi.org/10.1103/PhysRevD.81.094019.

[19] V. Barone, M. Boglione, J. O. Gonzalez Hernandez, and S. Melis, "Phenomenological analysis of azimuthal asymmetries in unpolarized semi-inclusive deep inelastic scattering," *Phys. Rev. D* **91** no. 7, (2015) 074019, arXiv:1502.04214 [hep-ph].

[20] S. Melis, "Phenomenology of TMDs," *EPJ Web Conf.* **85** (2015) 01001, arXiv:1412.1719 [hep-ph].

[21] C. Adolph *et al.* (COMPASS), "Measurement of azimuthal hadron asymmetries in semi-inclusive deep inelastic scattering off unpolarised nucleons," *Nucl. Phys. B* **886** (2014) 1046–1077, arXiv:1401.6284 [hep-ex].

[22] M. Aghasyan *et al.* (COMPASS), "Transverse-momentum-dependent Multiplicities of Charged Hadrons in Muon-Deuteron Deep Inelastic Scattering," *Phys. Rev. D* **97** no. 3, (2018) 032006, arXiv:1709.07374 [hep-ex].

[23] A. Bacchetta *et al.* (MAP collaboration), "Unpolarized transverse momentum distributions from a global fit of Drell-Yan and semi-inclusive deep-inelastic scattering data," *JHEP* **10** (2022) 127, arXiv:2206.07598 [hep-ph].

[24] J. Kónya and N. M. Nagy, "Chapter 5 - interaction of radiation with matter," in *Nuclear and Radiochemistry (Second Edition)*, J. Kónya and N. M. Nagy, eds., pp. 85–131. Elsevier, second edition ed., 2018. https://www.sciencedirect.com/science/article/pii/B9780128136430000056.

[25] P. Abbon *et al.* (COMPASS), "The COMPASS experiment at CERN," *Nuclear Instruments and Methods in Physics Research Section A: Accelerators, Spectrometers, Detectors and Associated Equipment* **577** no. 3, (2007) 455–518. https://www.sciencedirect.com/science/article/pii/S0168900207005001.

[26] B. Adams *et al.* (AMBER), "COMPASS++/AMBER: Proposal for measurements at the M2 beam line of the CERN SPS Phase-1: 2022-2024," 2019. https://cds.cern.ch/record/2676885?ln=en.

[27] G. Baum *et al.* (COMPASS), "COMPASS: A Proposal for a Common Muon and Proton Apparatus for Structure and Spectroscopy," Tech. Rep. CERN-SPSLC-96-14, SPSLC-P-297, CERN, Geneva, Switzerland, 1996. http://cds.cern.ch/record/298433.

[28] S. Navas *et al.* (Particle Data Group), "Review of particle physics," *Phys. Rev. D* **110** no. 3, (2024) 030001.

[29] C. Chatterjee, *Performance study of the RICH at COMPASS experiment for hadron identification in SIDIS physics.* PhD thesis, Universita' Di Trieste, Italy, 2020.

[30] V. Benesova, "Hadron production in deep inelastic scattering of muons off protons at COMPASS experiment," 2023. https://wwwcompass.cern.ch/compass/publications/theses/2023_bac_benesova.pdf. Bachlor's thesis, Charles University, Prague.

[31] S. Gerassimov, "PHAST: PHysics Analysis Software Tools." https://ges.web.cern.ch/ges/phast/index.html.

[32] T. Klasek, "Semi-inclusive DIS studies at COMPASS experiment," 2023. https://wwwcompass.cern.ch/compass/publications/theses/2023_bac_klasek.pdf. Bachlor's thesis, Charles University, Prague.

[33] NumPy development team, "NumPy v2.2 Manual – numpy.linalg." https://numpy.org/doc/stable/reference/routines.linalg.html.

[34] J. Agarwala *et al.* (COMPASS), "Contribution of exclusive diffractive processes to the measured azimuthal asymmetries in SIDIS," *Nuclear Physics B* **956** (July, 2020) 115039.

[35] G. D. Alexeev *et al.*, "Spin density matrix elements in exclusive ρ^0 meson muoproduction," 2023. https://arxiv.org/abs/2210.16932.

[36] A. Moretti, *Study of the Transverse-Momentum-Dependent structure of the nucleon in Semi-Inclusive DIS.* PhD thesis, 2021-08-16, Trieste U., 2021. arXiv:2109.08426 [hep-ex].

[37] A. E. G. Ingelman and J. Rathsman, "LEPTO 6.5 — a Monte Carlo generator for deep inelastic lepton-nucleon scattering," *Computer Physics Communications* **101** no. 1-2, (04, 1997) 108–134. https://doi.org/10.1016%2Fs0010-4655%2896%2900157-9.

[38] T. C. Szameitat, *New Geant4-based Monte Carlo software for the COMPASS-II experiment at CERN.* PhD thesis, Freiburg U., Germany, 2017.

[39] I. Akushevich and A. Ilyichev, "Lowest order QED radiative effects in polarized SIDIS," *Phys. Rev. D* **100** no. 3, (2019) 033005, arXiv:1905.09232 [hep-ph].

[40] A. A. Akhundov, D. Y. Bardin, L. Kalinovskaya, and T. Riemann, "Model independent QED corrections to the process e p $\rightarrow$ e X," *Fortsch. Phys.* **44** (1996) 373–482, arXiv:hep-ph/9407266.

[41] C. Adolph *et al.* (COMPASS), "Multiplicities of charged kaons from deep-inelastic muon scattering off an isoscalar target," *Physics Letters B* **767** (Apr., 2017) 133–141. http://dx.doi.org/10.1016/j.physletb.2017.01.053.

[42] C. Adolph *et al.* (COMPASS), "Multiplicities of charged pions and charged hadrons from deep-inelastic scattering of muons off an isoscalar target," *Physics Letters B* **764** (Jan., 2017) 1–10. http://dx.doi.org/10.1016/j.physletb.2016.09.042.

[43] K. Charchula, G. Schuler, and H. Spiesberger, "Combined QED and QCD radiative effects in deep inelastic lepton–proton scattering: The Monte Carlo generator DJANGO6," *Comput. Phys. Commun.* **81** (1994) 381–402.

[44] J. Matousek (COMPASS), "Azimuthal Asymmetries in Unpolarised Semi-Inclusive DIS at COMPASS," *JPS Conf. Proc.* **37** (2022) 020104, arXiv:2201.05205 [hep-ex].

[45] A. Airapetian *et al.* (HERMES), "Azimuthal distributions of charged hadrons, pions, and kaons produced in deep-inelastic scattering off unpolarized protons and deuterons," *Phys. Rev. D* **87** no. 1, (2013) 012010, arXiv:1204.4161 [hep-ex].

[46] S. Diehl *et al.* (CLAS), "Multidimensional, High Precision Measurements of Beam Single Spin Asymmetries in Semi-inclusive π^+ Electroproduction off Protons in the Valence Region," *Phys. Rev. Lett.* **128** no. 6, (2022) 062005, arXiv:2101.03544 [hep-ex].

[47] A. Airapetian *et al.*, "Beam-helicity asymmetries for single-hadron production in semi-inclusive deep-inelastic scattering from unpolarized hydrogen and deuterium targets," *Physics Letters B* **797** (Oct., 2019) 134886. http://dx.doi.org/10.1016/j.physletb.2019.134886.

[48] M. Anselmino, M. Boglione, J. O. Gonzalez H., S. Melis, and A. Prokudin, "Unpolarised transverse momentum dependent distribution and fragmentation functions from sidis multiplicities," *Journal of High Energy Physics* **2014** no. 4, (Apr., 2014) . http://dx.doi.org/10.1007/JHEP04(2014)005.

List of Figures

List of Tables

List of Abbreviations